creative commons

COMMONS DEED

저작자표시-비영리-동일조건변경허락 2.0 대한민국

이용자는 아래의 조건을 따르는 경우에 한하여 자유롭게

- 이 저작물을 복제, 배포, 전송, 전시, 공연 및 방송할 수 있습니다.
- 이차적 저작물을 작성할 수 있습니다.

다음과 같은 조건을 따라야 합니다:

저작자표시. 귀하는 원저작자를 표시하여야 합니다.

비영리. 귀하는 이 저작물을 영리 목적으로 이용할 수 없습니다.

동일조건변경허락. 귀하가 이 저작물을 개작, 변형 또는 가공했을 경우에는, 이 저작물과 동일한 이용허락조건하에서만 배포할 수 있습니다.

- 귀하는, 이 저작물의 재이용이나 배포의 경우, 이 저작물에 적용된 이용허락조건을 명확하게 나타내어야 합니다.
- 저작권자로부터 별도의 허가를 받으면 이러한 조건들은 적용되지 않습니다.

저작권법에 따른 이용자의 권리는 위의 내용에 의하여 영향을 받지 않습니다.

이것은 이용허락규약(Legal Code)을 이해하기 쉽게 요약한 것입니다.

Disclaimer

dCollection

이학박사학위논문

Theoretical Studies on Electronic and Magnetic Properties of Graphene Nanoribbons

2014 년 2 월

서울대학교 대학원
화학부 물리화학 전공
박희수

Theoretical Studies on Electronic and Magnetic Properties of Graphene Nanoribbons

지도교수 신 석 민

이 논문을 이학박사 학위논문으로 제출함
2013년 12월
서울대학교 대학원
화학부 물리화학 전공
박 희 수

박희수의 이학박사 학위논문을 인준함
2013년 12월

위 원 장 석 차 옥 (인)
부위원장 신 석 민 (인)
위 원 정 연 준 (인)
위 원 이 진 용 (인) lee
위 원 김 우 연 (인)

Abstract

Theoretical Studies on Electronic and Magnetic Properties of Graphene Nanoribbons

Heesoo Park

Physical Chemistry, Department of Chemistry

The Graduate School

Seoul National University

In this thesis, we have performed theoretical and computational studies on the properties of graphene nanoribbons (GNRs). The electronic structure of a graphene nanoribbon is different from that of graphene. As the bonds of graphene are broken in order to form edge structures, the two-dimensional structure turns into a one-dimensional-like structure. The zero band gap of the pristine graphene becomes open by the broken symmetry for graphene nanoribbons. In addition, either α- or β-spin state is localized at an edge with the spatial separation between different spin states. We have studied the model systems of chemically modified graphene nanoribbons by first-principle calculations on the band structure and the chemical reactions. We investigated the effects of the adsorption of small molecules and the application of external electric fields on the electronic properties of graphene nanoribbons.

In Chapter 1, features of the band structures for graphene and graphene nanoribbons are introduced. In order to understand the change of the band structure near the Fermi energy in periodic boundary conditions, it is necessary to explain how the atomic arrangement in real space is related with the band structure in reciprocal space, as discussed in terms of the wave vector for the orbital phases. We also introduced some of the experimental studies for the synthesis and the characterization of graphene and grapheme derivatives. These studies illustrated that controlled synthesis of graphene derivatives with particular properties could be very challenging. In Chapter 2, as a main computational method, general features of density functional theory (DFT) were described as compared with Hartree-Fock method. For the calculations of extended systems, DFT calculations with planewave wavefunctions as well as k-points sampling are explained.

In Chapter 3, our calculations with the DFT-PBE (Perdew-Burke-Ernzerhof) method on pristine graphene nanoribbons were compared with other reported DFT calculations. The electronic structures of pristine graphene nanoribbons are analyzed as a reference to show the differences from chemically modified graphene nanoribbons.

Graphene nanoribbons with zigzag edge structures are attracting attentions in the field of material research, because they are anticipated to be promising for future devices such as spintronics and transistors due to the unique electronic and magnetic properties. The properties of zigzag graphene nanoribbons (ZGNRs) can be tuned by the interactions with small molecules or under the effect of external field. In Chapter 4, the influence of pyridine adsorption and the applied electric field on the band structure and metallicity of ZGNRs was investigated by using DFT calculations. The semiconducting ZGNRs became half-metallic or remained semiconducting depending on the configuration of covalent bonds between pyridine and the ZGNRs. In addition, the band gap of the different spin states of the ZGNRs could be tuned by non-covalent bonds. This effect was enhanced when BF_3 was introduced simultaneously at the opposite edge. The applied external electric field can also modulate the band structures of the ZGNRs, making them half-metallic or semiconducting to some extent. These features suggest that the well-arranged adsorption of small molecules could be used to tune the band structures of nano-scale electronic devices based on graphene.

Removal of an epoxide group from oxidized ZGNR without damaging honeycomb structure of graphene is a challenging problem. In Chapter 5, we have studied the reaction mechanism of the epoxide group on the middle of narrow ZGNR. It was found that barriers for competing processes of migration and reduction depend on the widths of ZGNRs. It was also shown that the transition state energies were lowered by the application of perpendicular electric field with respect to the surface of ZGNR. Our studies illustrated that the electronic properties of graphene derivatives can be controlled by the modification of local structures of graphene chemically or electrically. Implications of such results, with the perspective of designing noble functional molecular systems, are discussed in Chapter 6.

Keywords: graphene, nanoribbon, zigzag edge, band structure, density functional theory, electric field
Student number: 2004-20455
Thesis Supervisor: Seokmin Shin
Title: Professor

To PM, KJ and HJ for their love, patience

Theoretical Studies on Electronic and Magnetic Properties of Graphene Nanoribbons

by

Heesoo Park

Submitted to the Department of Chemistry
in partial fulfillment of the requirements for the degree of

Doctor of Philosophy

at the

SEOUL NATIONAL UNIVERSITY

February 2014

Supervisor . . . . Seokmin Shin
Professor

Contents

Abstract i

Contents vii

List of Figures x

List of Tables xx

1 Introduction 1

1.1 Graphene and its derivatives synthesis 2

1.1.1 Graphene 3

1.1.2 Graphene oxide 4

1.1.3 Reduced graphene oxide 5

1.1.4 Graphene Nanoribbon 6

1.2 Band structure of GNR 7

1.2.1 C−C bonds and allotropes 7

1.2.2 Chemical bonding in solids: orbitals in a repeated potential . 8

1.2.3 Graphene 17

1.2.4 Graphene nanoribbon 22

1.2.5 Localized state in periodic boundary conditions and external electric field 24

2 Theory and Methodology **31**

2.1 Introduction 32

2.2 The Born-Oppenheimer approximation 32

2.3 Hartree-Fock and Kohn-Sham equations 33

2.3.1 Hartree-Fock (HF) 34

2.3.2 Density Functional Theory (DFT) 37

2.4 Reciprocal space and k-points 43

2.4.1 Reciprocal space 43

2.4.2 Brillouin zone sampling 47

3 Computational Studies on the Properties of Pristine GNRs **51**

3.1 Computational details: preliminary calculations 53

3.1.1 Lattice constants 53

3.1.2 Planewave cutoff 54

3.1.3 k-points sampling 57

3.2 Electronic and magnetic structure 59

3.2.1 Supercell and band structure 59

3.2.2 Band gaps related with the width of ZGNR 63

3.2.3 Magnetism of pristine GNR 64

3.3 DFT-PBE calculations of GNRs 67

4 Tuning of the Band Structures of GNRs by an Electric Field and adsorption of molecules **71**

4.1 Introduction 72

4.2 Computational Details 73

4.3 Results and discussion 77

4.3.1 Covalent and noncovalent interactions 77

4.3.2 External electric field 89

4.4 Conclusions 93

5 Migration and Removal of an Epoxide in Graphene Nanoribbons by the Width and an Electric Field 97

5.1 Introduction 98

5.2 Computational Methods 101

5.3 Results and discussion 103

5.3.1 Epoxide migration 104

5.3.2 Reduction of an epoxide 108

5.4 Conclusions 113

6 Concluding Remarks 117

A Band structures under an external electric field 125

B Band structures of 8-ZGNR with an epoxide group 129

Bibliography 132

국문초록 (Abstract in Korean) 157

감사의 말 (Acknowledgements) 161

List of Figures

1-1 The π orbitals of (a) ethylene and (b) allyl assembled from two and three CH_2 units, respectively. The π orbitals of allyl are put together ethylene moiety (ethylene minus a hydrogen atom) and CH_2 group. . 10

1-2 Polyenes with π orbitals are depicted as focused on valence electrons. (a) A polyene consists of N atoms with π orbitals. (b) The coefficient and phase of orbitals are adopted by size and color (white and dark gray), respectively. 13

1-3 The open-chain with infinite length is taken account as large cyclic system. We assume that at no π orbital does feel any curvature at all. 14

1-4 The phase variation between neighboring π orbitals is dependent on the k. 15

1-5 (a) The energy depending on wave vector k disperses as formed band in one-dimensional periodic orbitals. (b) The number of state (n) is described with respect to the energy level. Occupied states are in the dark-gray area. 17

1-6 (a) Real lattices of graphene are $\mathbf{a}_1$ and $\mathbf{a}_2$, and corresponding reciprocal lattice vectors are $\mathbf{b}_1$ and $\mathbf{b}_2$. A unit cell of graphene is composed of A and B sublattices. (b) The neighbor C atoms are at $1/3\mathbf{a}_1 - 2/3\mathbf{a}_2$, $1/3\mathbf{a}_1 + 1/3\mathbf{a}_2$, and $-2/3\mathbf{a}_1 + 1/3\mathbf{a}_2$. (c) The first Brillouin zone is filled with gray. The zone center, which is denoted as Γ, indicates $\mathbf{k} = 0$ 19

1-7 The band energy with respect to k for graphene. For the Fermi level, $E_\mathrm{f} = \alpha$. 20

1-8 The phases of orbitals are represented in real space according to the wave vectors of the reciprocal lattices. Crest is depicted as bright and trough is described as dark for the wave at M and K points in the Brillouin zone of graphene. 21

1-9 At Γ point, π and π^* unit cells are periodic with the invariant phase along the translation. When the reciprocal vector is on K point ($\mathbf{k} = \frac{2}{3}\mathbf{b}_1 + \frac{1}{3}\mathbf{b}_2$), the overall phases are same so that the state is degenerate. 21

1-10 The direction of armchair edge is parallel to $\Gamma \rightarrow$ M and that of zigzag edge is related with $\Gamma \rightarrow$ K. 23

1-11 The structure of edge can break the symmetry of graphene's sublattice. (a) The edge atoms are A sublattices of graphene in zigzag structure, meanwhile (b) both A and B sublattices are the edge atoms and they are paired in armchair structure. 24

1-12 The energy dispersion is plotted for graphene and GNR. The gap is zero for graphene between valence and conduction band near the K points, meanwhile the gap is open for GNR along the k space with the longitudinal axis. 25

1-13 The state of localized electrons, in repeating of molecules along the GNR, interacts with the state of delocalized electrons in GNR. . . . 26

1-14 Tuning the band for a spin state. (a) The edge state is localized at an edge with zigzag structure. (b) The edge state is degenerate due to the spatial symmetry for the spin states. (c) A system is polarized by an electric field. 27

2-1 H atoms cap the ZGNR. The same pattered circles indicate identical C atoms in the periodic boundary condition with the primitive lattice vector $\mathbf{a}_2$. The other primitive lattices are omitted due to the length of arrows, including vacuum in the unit cell. The translation primitive vector $\mathbf{a}_1$ goes from the left to the right, and the $\mathbf{a}_3$ comes out of the paper in the right angle to the other axes. 45

2-2 Schematic illustration of Bloch states of repeated p_z orbitals in one dimension is depicted depending on the $\mathbf{k}_2$ vectors. The each orbital is on an identical C atom in periodic boundary conditions; the same pattern depict them. The envelope is the smooth function that multiplies a periodic array of p_z orbital functions of C atoms, and the coefficients attribute to the size of the orbitals. 46

2-3 A band energy varies with respect to wave vector k in the first BZ. By the Monkhorst-Pack method, the sampled k-points are marked by empty circles. When $N_2 =$ (a) 2, (b) 3, and (c) 4 are given, the efficient points are chosen at uniform grids in reciprocal space. At the k-points the Bloch wavefunctions are integrated. 47

3-1 The calculation was performed with PBE functional and 400 eV cutoff energy, and $13 \times 13 \times 1$ k-points are sampled by Monkhorst-Pack grids. The bond length was subject to the lattice constant, as the locations of C atoms were determined with the proportion of lattice constants. The lengths are written in Å. (a) The 32 C atoms were arranged with perfectly hexagonal network in a supercell. (b) The energy of supercell is dependent on the C−C bond length. 54

3-2 The primitive cell was prepared from the result of lattice parameters of graphene. (a) The 8-ZGNR composed of 16 C atoms and two H atoms in a unit cell with lattice constant of 2.462 Å in the y-axis. The dashed line represents the unit cell. (b) In order to verify the cutoff energy, the calculation was performed with the cutoff energy from 200 to 700 eV. 56

3-3 The 8-ZGNR with lattice constant of 2.462 Å in the y-axis was calculated with the 400 eV cutoff energy. By the Monkhorst-Pack method, from 1 to 30 k-points were used to integrate the Bloch states. 57

3-4 The geometry of a row of 8-ZGNR was optimized in the periodic boundary condition. The lattice constant was 2.462 Å along the y-axis, and the distances are written in Å. 58

3-5 Supercells consisted of multiple primitive rows. The supercell is the area enclosed by solid lines. The gray circles are C atoms and the empty circles are H atoms. The 8-ZGNR composed of (a) 16 C + 2H, (b) 32 C + 4 H, (c) 48 C + 6 H, and (d) 64 C + 8 H in a supercell. Depending on the number of C atom in a supercell, the lattice constant was 2.462, 4.924, 7.836, 9.848 Å, respectively, along the y-axis. . . . 60

3-6 The plots are the band energy with respect to k in the first Brillouin zone (left) and the DOS (right) corresponding to the supercells of 8-ZGNR, where $E_{\mathbf{f}}$ denotes the Fermi energy. The supercells comprised (a) only the primitive cell, (b) two primitive cells, (c) three primitive cells, and (d) four primitive cells. The band in the α-spin state (solid line) was degenerated with the band in the β-spin state (dashed line). 61

3-7 The energy is different depending on the number of grids to be sampled in k-space. The reference energy is the total energy calculated by 30 Monkhorst-Pack grids for corresponding supercells. The supercells consisted of multiple primitive rows. As the supercell is larger in real space, the energies is converged with less grids. The circle, cross mark, square, triangle, diamond are for the 8-ZGNR-1P, 8-ZGNR-2P, 8-ZGNR-3P, 8-ZGNR-4P, and 8-ZGNR-5P supercell, respectively. . 62

3-8 (a) For 64-ZGNR, the band structure and DOS are plotted with respect to k space. During the calculation, spin-polarized wavefunctions were used. (b) The band gap is dependent on the width. The N-ZGNR have the width N. 63

3-9 For 6-ZGNR, the charge density difference is depicted for the α-spin electrons (red) and the β-spin electrons (blue). The zigzag edges have ferromagnetic structure along an edge. There are two states: (a) the same spin states are localized in both edges as ferromagnetic and (b) the different spin states are localized in each edge as antiferromagnetic. 65

3-10 (a) The band structures of 8-ZGNR in FM. The solid line is the band for the α-spin state and the dot-dash line is the band for the β-spin state. (b) The relative energy ($E_{\mathrm{FM}} - E_{\mathrm{AF}}$) is for an edge atom. N is the width of N-ZGNRs. 66

4-1 8-ZGNR is periodic along the x-axis. C1 to C8 (C1' to C8') denote the C atoms from the left (right) edge to the middle. 74

4-2 Optimized geometries of different bindings of pyridine with the ZGNRs fabricated in this work. Atom colors: carbon (brown); hydrogen (white); nitrogen (light blue). 75

4-3 Distances and adsorption energies were obtained with or without accounting for dispersion effects. (a) The distance between pyridine and graphene is defined as a distance between N atom of pyridine and the graphene surface. (b) Adsorption energies with and without the consideration of dispersive interactions are green-cross points and blue-empty-circle points, respectively. 78

4-4 Density of state (DOS) with a (red) and b (blue) state: (a) pristine ZGNR (b) **A**, (c) **S**, (d)-(l) for from $\mathbf{N}_0$ to $\mathbf{N}_8$ 79

4-5 Band structures and spin densities of (a) **A**, (b) **S**, and (c) $\mathbf{N}_0$ and (d) band gaps of the α- and β-spin states. The spin densities correspond to the partial charge ranging from $E - E_{\mathrm{f}}$ values of -0.30 (-0.25) to 0 eV in the upper figures and from -0.60 (-0.5) to -0.30 (-0.25) eV in the lower figures for **A** and **S** ($\mathbf{N}_0$). The band gaps of α-spin (solid line) and β-spin (dotted line) was obtained by calculations using PBE (blue) and PBE-D2 (green). 80

4-6 Band gaps of the α- and β-spin states for N-ZGNRs ($N = 4, 6, 8, \cdots, 64$). 82

4-7 Spin density of the highest valence bands: (a) the highest-1 bands of **A**, (b) the highest band of **A** (c) the highest bands of **S**. 83

4-8 Band gaps of the α- and β-spin states for 8-ZGNRs depending on the distance between the neighboring pyridine molecules. For $l = 2$, the lattice constant is 4.92 Å along the periodic axis. 84

4-9 Band structures with α (red) and β (blue) state: (a)-(i) for from $\mathbf{N}_0$ to $\mathbf{N}_8$. 85

4-10 Density of states (DOS) of (a) **A**, (b) **S**, (c) $\mathbf{N}_0$, and (d) $\mathbf{N}_8$ for the α-spin (red) and β-spin (blue) states. 87

4-11 The charge transfer of the outmost atoms, which is corresponding to C1 (blue cross and dot line) and C1' (green empty circle and dot-dash line), is plotted in a comparison with pristine ZGNR from $\mathbf{N}_0$ to $\mathbf{N}_8$. And that of pyridine (red filled square and solid line) is plotted in a comparison with the isolated pyridine. 88

4-12 Band gaps of each α (red filled squares)- and β (blue empty circles)-states: (a) pristine graphene, (b) **A**, (c) **S**, (d) $\mathbf{N}_0$, (e) $\mathbf{N}_2$, and (f) $\mathbf{N}_8$. 89

4-13 (a) Optimized geometries in which pyridine locates on C2 and BF_3 stays on C2', (b) DOS, and (c) band structure. 92

4-14 The localized edge states and the band energy by electron donor and electron acceptor. 94

5-1 The scheme for the reaction: (a) the reactant state, and (b) the product state. 101

5-2 (a) An epoxide group is at the middle site of the plane of 4-ZGNR. (b) **E** and **M** are discerned by the different location at which a CO molecule absorbs. (c) The positive (negative) F_{app} means that the external electric field is applied in the same (opposite) direction of the z-axis. 103

5-3 The figure depicts the bond and the geometry in the migration reaction, from (a) the reactant state, (b) the transition state, and (c) to the product state. 105

5-4 The plot depicts (a) the differences of the total energies between the reactant state and the product state (dotted line), $\mathit{\Delta} E^0$, and (b) the migration barriers (solid line), $\Delta E^{\ddagger}$ with respect to the electric field strength F_{app}. The green, blue, and red lines are for 4 (filled square)-, 6 (cross mark)-, and 8 (filled circle)-ZGNR, respectively. (c) The charge density difference is described, as the α- (β)-state charge is red (blue) at the transition state for 4-ZGNR. 106

5-5 For ZGNRs with an epoxide, the relative total energies are referenced to the energy of the corresponding N-ZGNR in which an epoxide is at C1$-$C2 site. 107

5-6 The adsorption energies (E_{ads}) are dependent on the conformation and F_{app}. (a) CO and CO_2 physisorb on the ZGNRs in **E**. The E_{ads} of (b) 4, (c) 6, and (d) 8-ZGNR increase as the F_{app} varies from -0.50 to 0.50 V/Å in the z-axis . The solid with cross and dotted lines with empty circle are for the conformation **E** and **M** respectively. The black line is for CO and the blue line is for CO_2. 110

5-7 (a) F_{app} reduces the difference of total energies between the reactant and product state. (b) The plot depicts that the barrier heights was lowered by applying a vertical electric field. The solid with filled mark (dotted line with empty mark) denote **E** (**M**) reaction paths, and the green, blue, and red lines are for 4, 6, and 8-ZGNR, respectively. . . 111

5-8 In the transition state, the charge density difference of (a) **E** and (b) **M** path is described by red and blue iso-surface, for the α- and β-state, respectively. 111

5-9 The site-projected DOS is plotted for the O of epoxide in the transition state for (a) p_x, (b) p_y, and (c) p_z states. In each plot, the upper and lower site-projected DOS is for α- and β-spin state, respectively. . . 114

A-1 Band structure of **A**. The valence and conduction band is shifted under the external electric field. 126

A-2 Band structure of $\mathbf{N}_0$. The valence and conduction band is shifted under the external electric field. 127

B-1 The band structures of 8-ZGNRs with an epoxide group. The location of an epoxide group is at between (a) C1 and C2, (b) C2 and C3, (c) C3 and C4, (d) C4 and C5, (e) C5 and C6, (f) C6 and C7, (g) C7 and C8, and, (h) C8 and C9. 130

B-2 The band gaps for the α- and β-spin states with respect to the location of epoxide. 131

List of Tables

3.1 The magnetic moments with H terminations for N-ZGNRs with various widths for AF and FM configurations. 65

4.1 Band Gaps (eV) of ZGNRs by Pyridine or BF_3 Adsorption on C2 . 93

4.2 Band Gap (eV) Variation of $\mathbf{N}_0$ by BF_3 Adsorption at C0′, C1′, or C2′ 93

5.1 In the transition state, the l_{TS}(C-O) (in Å) is varied depending on F_{app}. 108

5.2 The l_{TS}(C-O) (in Å) is varied depending on F_{app}, in the reactant state (RS) and the transition state (TS). 113

Chapter 1

Introduction

An atom is made of the nucleus and the electrons. And the atom relates to neighbor atoms by redistribution of the electrons. By theoretical methods in which we describe the state of the electrons, we obtain the properties of a matter at the atomic and molecular level; the strength of chemical bonds varies considerably as the result of the electronic degrees of freedom in the system of matter and the adsorption or emission of a photon happens with the frequency which is a consequence of difference between the energy levels of the electrons in the system. There are our major issues for graphene nanoribbons (GNRs) of which electronic structures were derived by chemical decorations, and we compared them with pristine GNRs.

In Chapter 1, we introduce the repeated atomic orbitals in a periodic potential. Graphene is composed of only C atoms. And each carbon atom is connected to four other carbons in sp^2 hybridization. The sp^2 hybridization of C$-$C leads graphene to be unique material. The energy dispersion of band may be explained by analogous band of polyenes by which we tackle a problem from ethylene to infinitely long polyenes. For graphene, furthermore, it is extended to two-dimensional structure. As a result of the hexagonal carbon network, the energy-momentum relation (dispersion relation) is conical at near the K points due to the structure of graphene.

Meanwhile, GNRs turn in quasi-one-dimensional structure with finite width. And the electronic structure of GNRs is different from that of graphene, because it is no longer two-dimensional structure. The band gap is open from the zero gap to a finite gap, depending on the edge structure and the width. In other words, we can control the band gap by the adequate edge structure and width. Since a spin state is localized along an edge with zigzag structure particularly, we may manipulate the edge state in order to tune a band of GNRs for either α- or β-spin state.

The chemical properties and the reactions are important to understand to tune the band structure of GNRs. Moreover, it is essential to exploit the reaction mechanism to obtain the desired structure by synthesis. As we applied an electric field also on the system, we analyzed and compared the chemical modification in GNRs.

1.1 Graphene and its derivatives synthesis

Wallace predicted the electronic structure of graphene with the results of his theoretical study in 1947[1]. According to the tight-binding model, graphene is semimetallic of which band gap is zero. And other theoretical work followed giving the peculiar properties of graphene.[2–6] However, it took several decades to measure a single layer (graphene) exfoliated from graphite. Since graphene is one of the thinnest materials and it attracts other flakes by dispersion forces, it had been challenging to extract. In this section, we would discuss mainly the recent experimental results of graphene. The chemical and physical properties will be briefly introduced from the synthesis to the prospective applications. And we put theoretical works aside for following chapters.

1.1.1 Graphene

Carbon materials based on carbon nanotubes have attracted great interest because of the flexibility of their electronic properties and applications for devices and sensors.[7–9] The metallic or semiconducting nature of carbon nanotubes is essentially dependent on their morphology, diameter, and chirality. Due to the inhomogeneity of the experimentally obtained diameter, it is quite a challenging task to fabricate an electronic or spintronic device.

Graphite is also one of allotropes of carbon. Even before a single layer of graphite was successfully extracted from multiple layers, the properties of graphite had been well-known and it is easy to figure out what looks like the structure of the mono-layer graphite is. It is the structure where hexagonal structure—as analogous of benzene—is repeated in two dimensions, and the multiple flakes compose of graphite. The C$-$C bonds are combined in sp^2 hybridization in basal plane, and the outmost C atoms are capped with H atoms. However, before Geim and Novoselov experimented with complete graphene flake of which structure have rarely defects, no one had observed the properties of the single layer. By using scotch-tape, it was possible to separate a graphene flake from graphite. Through the successful extractions of a monolayer from a bunch of graphene layers, Geim, Novoselov, and Kim observed the properties successfully such as massless Dirac fermion and quantum Hall effect.[10–12] And graphene has been gathering much attention in condensed matter research.

The discovery of the unique two-dimensional crystal leads attentions to the control of synthesis two-dimensional structure to be designed. As the simple method of mechanically peeling was introduced, the desirable material came to be realized and it is now considered as promising material for various applications because of unique properties than carbon nanotubes (CNTs).[13,14] Many researchers got started to pay the derivatives of graphene as well: graphene nanoribbon, graphene with functional molecules or with metal atoms, and including other two-dimensional carbon complexes.[15] In particular, when a single-walled carbon nanotube (SWCNT) is unrolled, a two-dimensional monolayer of graphite, graphene, is formed.

The drawback of mechanical peeling is that the yield is limited to the number of exfoliation procedure, in addition, there is no more control over the graphene's spatial structure because there are few chemical methods to synthesis the optimal structure. The chemical vapor deposition (CVD) method deposits mono- or a few layer graphene films atop transition metal catalysts, such as Ni, Cu, and Ru.[16–19] It uses gaseous carbon source as precursor of graphene, such as CH_4 and C_2H_2. The spatial product can be controlled by the arrangement of catalysts and precursor.

Since the first high-quality graphene prepared by Novoselov and Geim,[10] experimental and theoretical studies of graphene and its derivatives have been performed extensively and intensively over the past years.[20–25] In experimental studies of graphene, contrary to CNTs, diameter and chirality control are not required. Nevertheless, graphene is reported to have excellent electrical, optical, and mechanical properties. Because of the band gap and the transparency feature, it is potential material for various applications such as solar cells and flexible displays.[14,25–36]

1.1.2 Graphene oxide

There have been researches on the chemical modification of graphite as solution-based processes. Chemical modification in solution would be one of the most efficient methods in which we can produce desirable derivatives from graphene. It is feasible to obtain mass yield. Once graphite is oxidized, a stable aqueous dispersion of graphene is obtained in the form of individual graphene oxide (GO) sheet, because the hydrophilic functional groups of GO facilitate exfoliation and dispersion in aqueous solutions. Graphene oxide is soluble, and this is easily separated by ultrasonic dispersion with less van der Waals forces. The advantage is that there is not to limit to the quantity but the amount of the substance.

The oxidation in the basal plane of graphene, however, makes defects form sp^3 orbitals. Hydroxyl and epoxy groups are in the basal plane of GOs and carbonyl and carboxyl groups are on the edge sites.[37,38] As a result of oxidation, GO is insulator. Regarding the functionalization of graphene, most studies have been related to GO because the graphene edges often exist as oxides in most experimental preparations.[39–41] So, in order to prepare GO, it is determining procedure for the properties of GO to manipulate the molecular function.

1.1.3 Reduced graphene oxide

Reduced graphene oxide (RGO) is a resultant graphene oxide to be reduced again. Even though there are abundant functional groups, it can be chemically reduced by reducing agents such as hydrazine.[42] Most of the epoxy groups can be removed and form a $C{=}C$ structure, though $-OH$ groups bonded to the surface of GO can not be reduced by hydrazine even at relative high temperature.[43] The harsh oxidization process, however, break the conjugate $C-C$ bonds of the pristine graphene.[44–46] That is still lack behind that of pristine graphene by a factor of 10-100.[42,47] The defects are not completely recovered to the pristine graphene.

By controlling the oxidation and reduction reactions, in addition to feasibility of exfoliation, the conductivity of GOs can be controlled in spite of metallic character of pristine graphene. The conductivity of GOs is increased by up to 4 orders of magnitude by reducing oxygen functional groups, while the oxidized areas are restored to sp^2-bonded carbon networks. A number of atomically structural defects and oxygen functional groups with insulating properties are present, which however lack the perfect crystallinity of intact graphene.[48] Moreover, the band gap of RGO is possibly modulated by tuning the femtosecond lase power.[49] Reduction process as well as oxidation process can be manipulated to tune the band structure.

1.1.4 Graphene Nanoribbon

Graphene exhibits semimetallic behavior with zero band gap. Meanwhile, due to the quantum confinement and edge effects, narrow graphene nanoribbons (GNRs) are semiconductors.[50,51] Thus, GNRs are attracting for its the possibility of electronic applications. Depending upon the width and orientation of the edges, there are reports for GNRs to offer a possibility of achieving tunable electronic properties[20–23,26]. Showing intriguing theoretical and experimental results, GNR is the promising candidate to be applied beyond the conventional electric devices.[14,26–33,50–52]

It is necessary that graphene should be fabricated as nanoribbon to apply microdevices. The electrochemically synthesis was introduced that large-area and patterned graphene oxide was reduced by the potentiostatic method.[53] Opening the prospect of patterning oxidized regions on RGO with nanometric resolution, RGO sheets were controllably reoxdized on a local scale by means of STM lithography.[54] And modification of graphene was patterned under light illumination,[55] creating reactive intermediate species.

Among the oxygen functional groups,epoxy groups are able to unzip graphene basal. GO unzipping is initiated by the strain generated by the cooperative alignment of epoxy group on a carbon lattice of graphene.[56–58] GNR can be synthesized even inside of carbon nanotubes where chemical reactions occur differently from the bulk three-dimensional conditions.[59] And 13-AGNR is fabricated from molecular precursors and observed the band gap.[60] Recently, precise fabrication of GNRs with the edges passivated by H atoms was realized using surface-assisted coupling of molecular precursors.[7] Accordingly, by utilizing the proper precursors, chemically modified GNRs may be achieved. As a result of much effort to circumvent such physical difficulties, diverse techniques have been reported to acquire desirable fragments, such as nanoribbon and large size flakes with good quality at low cost.[20,37,61]

Although some GNRs were successfully synthesized in a few experiments, the fabrication of GNRs with uniformly functionalized edges is very challenging yet. It has been baffling to observe the properties of all the derivatives by experiments. And it needs much effort to design a GNR of which chemical and physical properties are refined for a purpose and to synthesis the designed GNR. In order to understand the chemical and physical character of various derivative GNRs, it is necessary to study theoretical models for GNRs.

1.2 Band structure of GNR

1.2.1 C−C bonds and allotropes

A carbon atom has two core electrons (two-1s orbital) and four valence electrons (two-2s and two-2p orbital). The number of valence electron makes carbon be capable to form many allotropes. There are matters that consist of only carbon atoms such as diamond and graphite. Although both are composed of only carbon atoms, the chemical and physical properties are different according to the forms of C−C bonds.

The network of carbon atoms is arranged in a tetrahedral lattice or in sheets of a hexagonal lattice.

Diamond is one well known as an allotrope of carbon. Carbon atoms are in a covalent network lattice that crystallizes into the diamond crystal lattice that is a variation of the face centered cubic structure. Due to the hybridization sp^3, diamond is the hardest mineral in nature on earth. And it is an electrical insulator. Graphite is different from diamond. The carbon atoms are arranged in a honeycomb lattice as a sheet. And a bunch of these layers consist of graphite. Because the C−C bonds of the flakes are in sp^2 hybridization, it is an electrical conductor or semimetal.

The properties are subtle in a nanometer scale. The discovery of fullerene molecules [62] and carbon nanotubes [63] have triggered the intensive research on various nanometer-sized carbon materials. And Geim and Novoslelov found an effective and simple way to exfoliate an atomic layer from graphite. [10] Using scotch tape, they peeled off the flakes of graphite repeatedly. After they measured successfully the mobility of electrons and holes, many researchers have paid their attention to the electronic and magnetic properties of graphene and nanographites.

In these systems, the geometry of sp^2 carbon networks crucially affects their electronic states near the Fermi level. [64,65] To understand the Fermi level and band structure of graphene, we are necessary to grasp the electronic structure of an individual carbon atom and the periodicity of the carbon atoms in honeycomb lattice.

1.2.2 Chemical bonding in solids: orbitals in a repeated potential

Though GNRs are strips of graphene, a number of carbon atoms consist of GNRs still. An astronomically large numbers of computing resources are necessary for us to deal with the whole degrees of freedom of the electrons in a system, if we were to do the computational research of GNRs by considering all correlated electrons on every atom. However, a problem of electronic wavefunction of GNR is reduced by translation symmetry. Due to the geometry of crystal, we may assume a system to be a collection of repeating units. Then we can solve a problem of an infinitely long GNR by contemplating a unit cell and the relation between unit cells.

Polyene

The discussion of chemical bonds in solids might start by looking at the electronic structure of molecules.[66–69] It gives us a useful basis from which we can move to solid state and its band structure. The conjugated open-chain molecules are π systems as a graphene consists of carbon atoms in sp^2 hybridization. Among these molecules, an ethylene comprises two carbon atoms.

We may write the wavefunction of valence electrons of ethylene as the molecular orbitals (MOs) of H_2 is expressed,

$$\psi = a\phi_1 + b\phi_2 \tag{1.1}$$

While the basis orbitals ($\phi_{1,2}$) are $1s$ orbitals for H_2, the basis orbitals are p_z orbitals of carbon for ethylene. Since the probability of the state (ψ) in the whole of space is

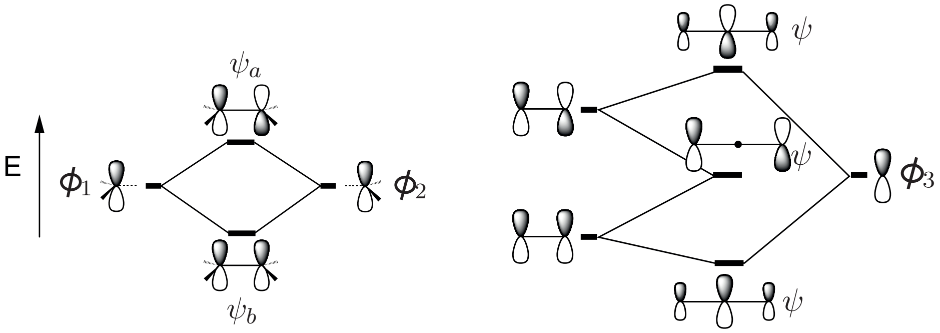

(a) The π orbitals of ethylene (b) The π orbitals allyl

Figure 1-1: The π orbitals of (a) ethylene and (b) allyl assembled from two and three CH_2 units, respectively. The π orbitals of allyl are put together ethylene moiety (ethylene minus a hydrogen atom) and CH_2 group.

1,

$$\begin{aligned}\langle\psi|\psi\rangle &= \langle a\phi_1 + b\phi_2|a\phi_1 + b\phi_2\rangle \\ &= a^2\langle\phi_1|\phi_1\rangle + b^2\langle\phi_2|\phi_2\rangle + 2ab\langle\phi_1|\phi_2\rangle \\ &= a^2 + b^2 + 2abS \\ &= 1\end{aligned} \tag{1.2}$$

where S is a overlap integral, it is defined as $S = \langle\phi_1|\phi_2\rangle$. By symmetry the electron density must be equal on both carbon atoms, leading to $a = \pm b$. As a result from the normalization, we can obtain two wavefunctions,

$$\left.\begin{aligned}\psi_a &= \pm\frac{1}{\sqrt{2(1-S)}}(\phi_1 - \phi_2) \\ \psi_b &= \pm\frac{1}{\sqrt{2(1+S)}}(\phi_1 + \phi_2)\end{aligned}\right\} \tag{1.3}$$

We may derive the energy levels using Hückel theory, ignoring S.* If the Coulomb integral is defined as $\alpha = \langle\phi_1|\mathscr{H}^{\mathrm{eff}}|\phi_1\rangle = \langle\phi_2|\mathscr{H}^{\mathrm{eff}}|\phi_2\rangle$ and the interaction integral $\beta = \langle\phi_1|\mathscr{H}^{\mathrm{eff}}|\phi_2\rangle$, where $\mathscr{H}^{\mathrm{eff}}$ is effective Hamiltonian for the problem, then we can generate the bonding energies from the Hückel determinant $|H_{ij} - E| = 0$.[†]

---

*Extended Hückel method;[70,71] a nonorthogonal overlap matrix S is calculated. The S along with separately fitted onsite Hamiltonian matrix elements yields correspondingly off-diagonal hopping elements of the Hamiltonian.

For the energy levels of conjugated open-chain molecules, the secular determinant is directly applicable. Solving this simple determinant

$$\begin{vmatrix} \alpha - E & \beta \\ \beta & \alpha - E \end{vmatrix} = 0 \tag{1.4}$$

we immediately obtain the result

$$\left.\begin{aligned} E_a &= \alpha - \beta \\ E_b &= \alpha + \beta \end{aligned}\right\} \tag{1.5}$$

This result is shown in Figure 1-1(a). ψ_b is the ground electronic configuration, in which a bonding orbital is depicted as ϕ_1 and ϕ_2 are combined in-phase. The energy is lower with E_b than E_a. In the meantime, ψ_a is in the higher lying level. The MOs are out-of-phase between ϕ_1 and ϕ_2. It describes anti-bonding.

In principle we can generate energy levels and orbital coefficients straightforwardly, adding CH_2. The π energy levels of allyl are given analogously,

$$\begin{vmatrix} \alpha - E & \beta & 0 \\ \beta & \alpha - E & \beta \\ 0 & \beta & \alpha - E \end{vmatrix} = 0 \tag{1.6}$$

No entry appears in the 1,3 position since orbital interactions are included only between atoms in covalent bonds. The roots are

---

[†] $H_{ij} = \langle\phi_i|\mathscr{H}^{\mathrm{eff}}|\phi_j\rangle$

$$\left.\begin{aligned} E_1 &= \alpha - \beta \\ E_2 &= \alpha \\ E_3 &= \alpha + \beta \end{aligned}\right\} \tag{1.7}$$

and the orbital wavefunctions are

$$\left.\begin{aligned} \psi_1 &= 0.5\phi_1 - 0.71\phi_2 + 0.5\phi_3 \\ \psi_2 &= 0.71\phi_1 - 0.71\phi_3 \\ \psi_3 &= 0.5\phi + 0.71\phi_2 + 0.5\phi_3 \end{aligned}\right\} \tag{1.8}$$

Figure 1-1(b) shows the orbitals and coefficients for ally. The orbital wavefunction ψ_3 is at the lowest level. And the higher-energy orbital has more nodes in terms of phase variation. It also is noted that ψ_3 describes anti-bonding as ϕ_1, ϕ_2, and ϕ_3 are combined out-of-phase between the neighbors.

Simple functions describe both the energy levels and orbital coefficients for ethylene and allyl. It can be extended to longer conjugated chain as well. For open-chain conjugated hydrocarbons, which are unbranched and linear polyenes ($\mathrm{C_nH_{n+2}}$) as shown in Figure 1-2(a), we can obtain the energy levels. As shown by Coulson [72–74], the energy of the pth MO for a system with N π orbitals (p_z) is given as,

$$E_p = \alpha + 2\beta\cos\left(\frac{p\pi}{N+1}\right) \tag{1.9}$$

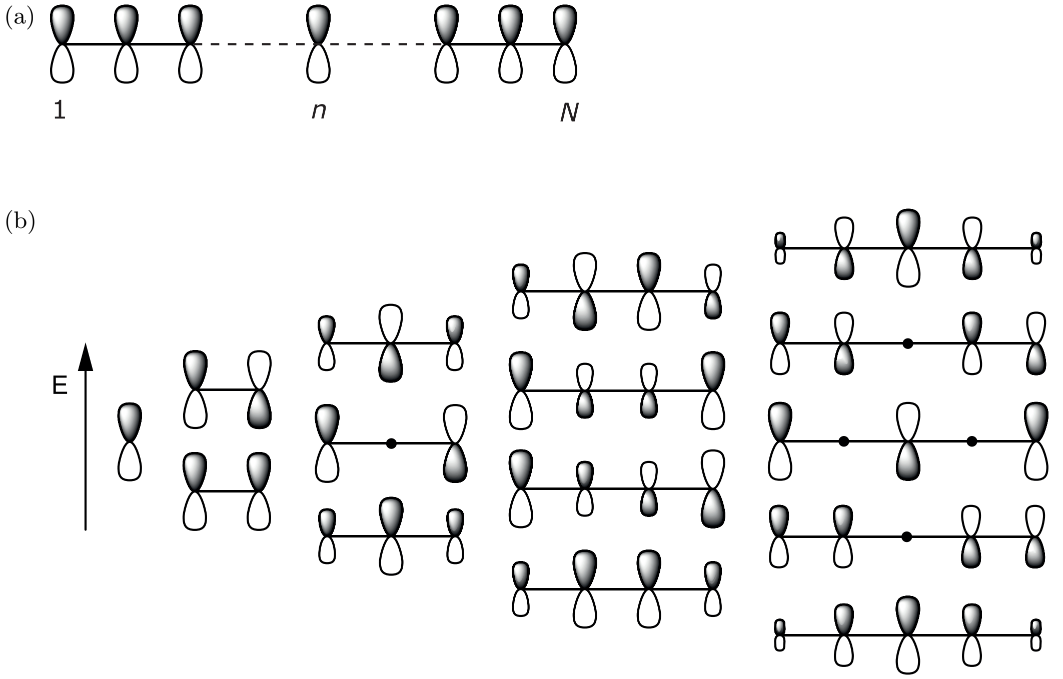

Figure 1-2: Polyenes with π orbitals are depicted as focused on valence electrons. (a) A polyene consists of N atoms with π orbitals. (b) The coefficient and phase of orbitals are adopted by size and color (white and dark gray), respectively.

and the orbital coefficient c_{pn} of ϕ_n in the ψ_p MO is given by

$$c_{pn} = \sqrt{\frac{2}{N+1}} \sin\left(\frac{pn\pi}{N+1}\right) \tag{1.10}$$

The results of E_p and c_{pn} are given pictorially in Figure 1-2. The figure depicts the evolution of the π-orbital for conjugated linear polyenes. The number of nodes in the wavefunction increases by one as the energy increases.

Cyclic system

As noted in Eq. 1.9, the extension for the open-chain molecule leads to an infinite collection of orbitals bounded by the energies of $\alpha \pm 2\beta$. However, the polyenes with

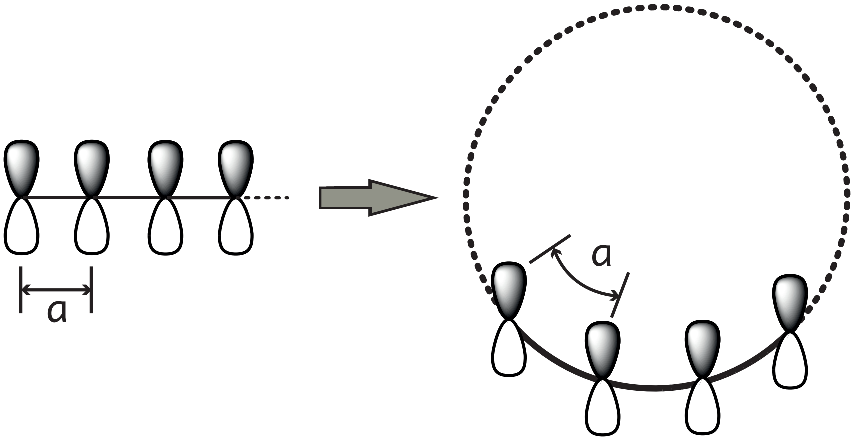

Figure 1-3: The open-chain with infinite length is taken account as large cyclic system. We assume that at no π orbital does feel any curvature at all.

infinite number of atoms are cumbersome to deal with. It is more useful to take account it as a cyclic system.[75,76] We may approach the system as the two ends of a chain are connected, as shown in Figure 1-3. The energies are given by

$$E_j = \alpha + 2\beta \cos ka \tag{1.11}$$

where $k = 2p\pi/Na$ and a is the unit cell length. This k is called wave vector, taking values from 0 to $\pm\pi/a$ continuously in the first Brillouin zone. The variation of the energy with k is the dispersion of the band.

At $k = 0$, the phase factor linking an orbital with its neighbor is equal for all π orbitals and so the wavefunctions look like Figure 1-4(a). There is not a node for π orbitals. And the energy is bottom, $E = \alpha + 2\beta$. The top of the band occurs at $k = \pi/a$ and the energy is $\alpha - 2\beta$. Since the wave vector of π/a indicates that the phase is opposite by translation of a, the each orbital shown in Figure 1-4(b) is asymmetric with neighbor orbitals at both sides. As k increases from 0, the state energy is lager and the MOs have more nodes.

When N is infinitely large as ring sizes increase, the wavefunctions in periodic potential are given as

$$\psi(k) = \frac{1}{\sqrt{N}} \sum_{n=1}^{N} e^{ik\mathbf{R}_n} \phi(\mathbf{r} - \mathbf{R}_n) \tag{1.12}$$

where $\phi(\mathbf{r}-\mathbf{R}_n)$ is the atomic orbital wavefunction (p_z) of nth carbon atom. And this periodic wavefunction is called Bloch function. Furthermore, the energy dispersion with respect to k may be rewritten as a general expression of energy, describing electronic structures for an extended system,

$$\begin{aligned}
E(k) &= \langle \psi(k) \left| \mathscr{H}^{\text{eff}} \right| \psi(k) \rangle \\
&= \left\langle \frac{1}{\sqrt{N}} \left(\cdots \phi + \phi(r-a)e^{ika} + \phi(r-2a)e^{2ika} + \cdots \right) \right| \\
&\times \mathscr{H}^{\text{eff}} \left| \frac{1}{\sqrt{N}} \left(\cdots \phi + \phi(r-a)e^{ika} + \phi(r-2a)e^{2ika} + \cdots \right) \right\rangle \\
&= \frac{1}{N} \cdot N \left\{ \alpha + \left(e^{ika} + e^{-ika} \right) \beta \right\} \\
&= \alpha + 2\beta \cos ka
\end{aligned} \tag{1.13}$$

The energy that we obtained here is same as the energy of cyclic polyenes in Eq. 1.11. Moreover, this can be rewritten by Hückl theory. The energy per unit may be

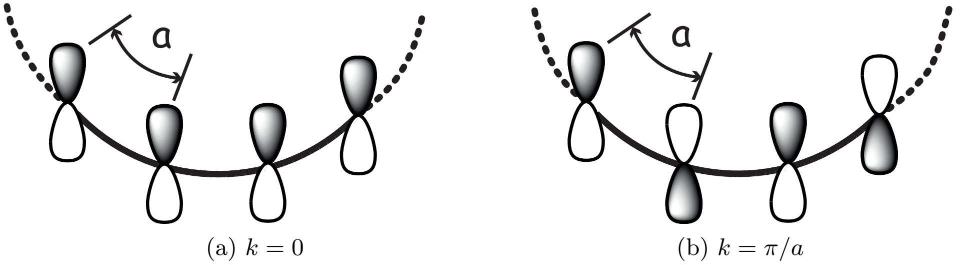

(a) $k = 0$ (b) $k = \pi/a$

Figure 1-4: The phase variation between neighboring π orbitals is dependent on the k.

expressed as

$$\begin{vmatrix} \alpha - E & \beta(e^{ika} + e^{-ika}) \\ \beta(e^{-ika} + e^{ika}) & \alpha - E \end{vmatrix} = 0 \tag{1.14}$$

The resonance integrals, H_{12} or $H_{21}(= H_{12}{}^*)$, are β multiplied by the summation of the phase difference of periodic wavefunctions with neighbors. In other words, the neighbors are the reference unit itself but the phase is changed according to the periodic wavefunction.

In this case, we have

$$E = \alpha \pm 2\beta \mathrm{cos} ka \tag{1.15}$$

When the orbital phase is invariant along the cyclic line with $k = 0$, $E = \alpha + 2\beta \mathrm{cos} ka$. Meanwhile, when the phase of orbitals is opposite with neighbors with $k = \pi/a$, $E = \alpha - 2\beta \mathrm{cos} ka$.

As we take $k = 0$, we can consider the system to be come out of two different states, π or π^*, if there are two sublattice in a unit cell. This will be discussed in the following subsection for the band of graphene.

Fermi level

Electron is fermion, which is characterized by Fermi-Dirac statistics due to half-integer spin. Two electrons cannot occupy the same state. There are not two electrons that the quantum number is same at a location, at the same time. For the reason, there are only two electrons at a certain energy level. One electron is in the α-spin sate and another electron is in the β-spin state. Given the number of electron, the energies are filled doubly from the lowest level upto some level. The highest occupied level is called the Fermi level. The Fermi level is indicated in Figure 1-5 as E_{f} and the corresponding wave vector is denoted as k_{f}. The electrons are filled in the range from $\alpha + 2\beta$ to E_{f}.

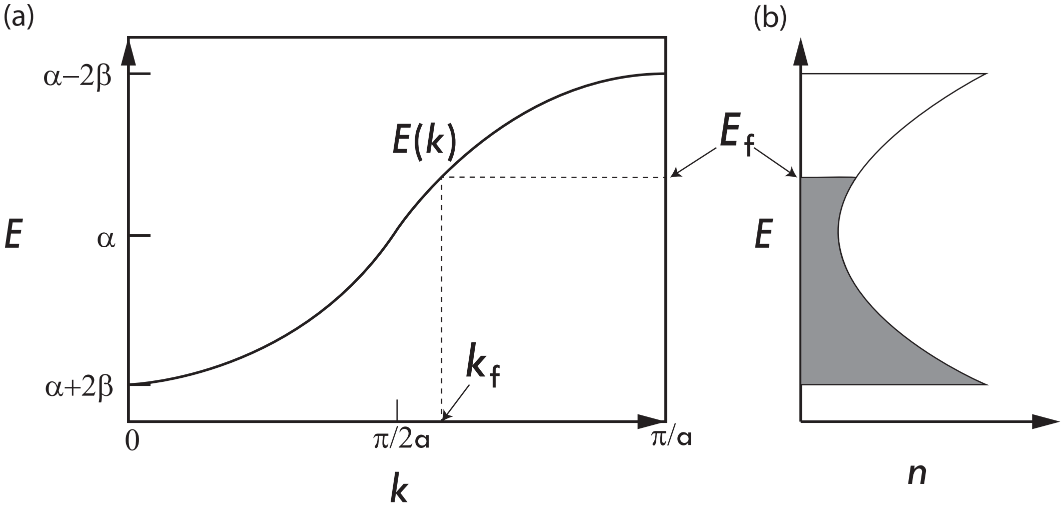

Figure 1-5: (a) The energy depending on wave vector k disperses as formed band in one-dimensional periodic orbitals. (b) The number of state (n) is described with respect to the energy level. Occupied states are in the dark-gray area.

1.2.3 Graphene

MOs were expressed by the linear combination of π orbitals. Two MOs of ethylene were the first conjugated bonds with two energy levels and the N MOs of polyenes came from linear combinations of π orbitals with corresponding energy levels by Eq. 1.9. And the description for solid state has been extended to the periodic wavefunctions, which are formulated in Bloch functions. Graphene consists of carbon atoms that are connected in sp^2 hybridization. We may take account π orbitals of graphene as two-dimensional π network in honeycomb lattice.

Graphene is two-dimensional crystal in which carbon atoms are arranged in a honeycomb lattice. Each carbon atom has three covalent bonds in the plane. Among four valence electrons of carbon are three electrons in sp^2 bonds, and another electron is in the p_z orbital. Although the energy level of the valence band in graphene is originated from the π orbitals as that of MO in polyene is, there are differences as a result of the two-dimensional structure of graphene. It is bipartite lattice. As shown in Figure 1-6, the unit cell is made of two inequivalent sublattices indicated as “A” and “B”. And the unit cell is with primitive lattice vectors, which are $\mathbf{a}_1$ and $\mathbf{a}_2$. A sublattice and the equivalent are located at every $l\mathbf{a}_1 + m\mathbf{a}_2$, where l and m are integers, in real space. [‡]

As the band of polyenes is generated by Hückel theory, the valence band of graphene may be provided by Hückel approximation.[69,75] While one orbital was chosen for a repeated unit in Figure 1-3, two orbitals compose of a unit for graphene due to bipartite lattices as shown in Figure 1-6(a).

As we take $S_{11}(\mathbf{k}) = S_{22}(\mathbf{k})$ and $S_{12}(\mathbf{k}) = S_{21}(\mathbf{k}) = 0$, according to Hückel theory the secular determinant becomes

$$\begin{vmatrix} \alpha - E(k) & \beta B \\ \beta B^* & \alpha - E(k) \end{vmatrix} = 0 \tag{1.16}$$

As the resonance integrals of Eq. 1.14 for polyenes is expressed by the phase differences, H_{12} is written as β is multiplied by the summation of phase differences with

---

[‡] In three dimension, reciprocal lattices are related with real lattices as

$$\mathbf{b}_1 = 2\pi\frac{\mathbf{a}_2 \times \mathbf{a}_3}{|\mathbf{a}_1 \cdot (\mathbf{a}_2 \times \mathbf{a}_3)|}, \quad \mathbf{b}_2 = 2\pi\frac{\mathbf{a}_3 \times \mathbf{a}_1}{|\mathbf{a}_2 \cdot (\mathbf{a}_3 \times \mathbf{a}_1)|}, \quad \mathbf{b}_3 = 2\pi\frac{\mathbf{a}_1 \times \mathbf{a}_2}{|\mathbf{a}_3 \cdot (\mathbf{a}_1 \times \mathbf{a}_2)|}$$

So,

$$e^{i(k_1\mathbf{b}_1 \cdot l_1\mathbf{a}_1)}e^{i(k_2\mathbf{b}_2 \cdot l_2\mathbf{a}_2)}e^{i(k_3\mathbf{b}_3 \cdot l_3\mathbf{a}_3)} = e^{i(\mathbf{k}\cdot\mathbf{r})}$$

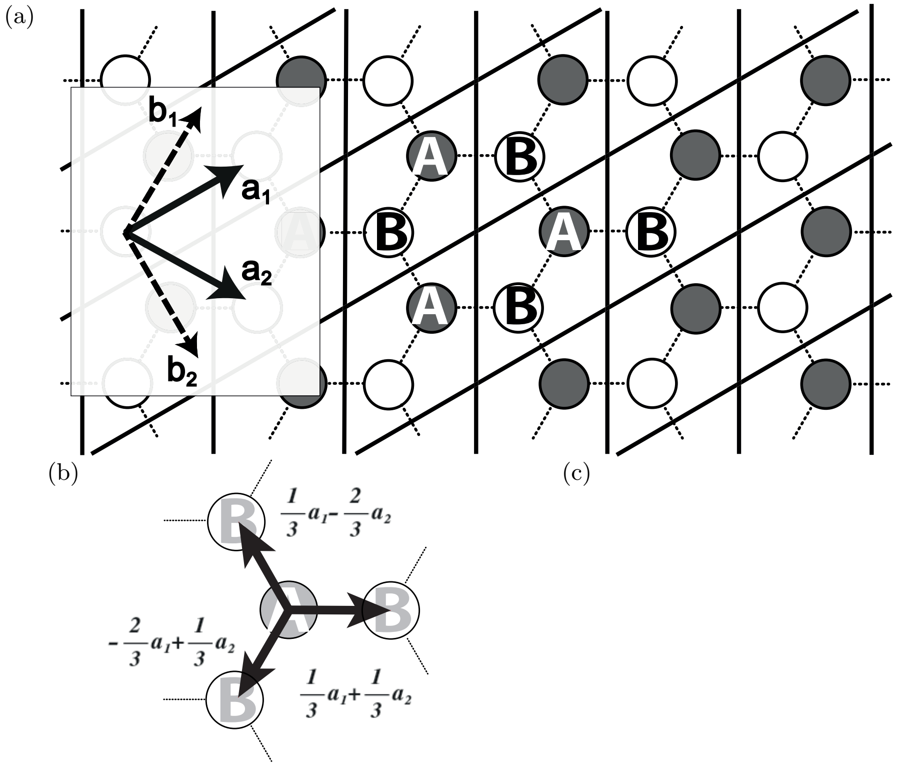
(a)
$\mathbf{b}_1$
$\mathbf{a}_1$
$\mathbf{a}_2$
$\mathbf{b}_2$
A
B
(b)
(c)
$\frac{1}{3}a_1-\frac{2}{3}a_2$
$-\frac{2}{3}a_1+\frac{1}{3}a_2$
$\frac{1}{3}a_1+\frac{1}{3}a_2$

Figure 1-6: (a) Real lattices of graphene are $\mathbf{a}_1$ and $\mathbf{a}_2$, and corresponding reciprocal lattice vectors are $\mathbf{b}_1$ and $\mathbf{b}_2$. A unit cell of graphene is composed of A and B sublattices. (b) The neighbor C atoms are at $1/3\mathbf{a}_1 - 2/3\mathbf{a}_2$, $1/3\mathbf{a}_1 + 1/3\mathbf{a}_2$, and $-2/3\mathbf{a}_1 + 1/3\mathbf{a}_2$. (c) The first Brillouin zone is filled with gray. The zone center, which is denoted as Γ, indicates $\mathbf{k} = 0$

three neighbors. So,

$$B = e^{-i\mathbf{k}\left(\frac{1}{3}\boldsymbol{a}_1+\frac{1}{3}\boldsymbol{a}_2\right)} + e^{-i\mathbf{k}\left(-\frac{1}{3}\boldsymbol{a}_1+\frac{2}{3}\boldsymbol{a}_2\right)} + e^{-i\mathbf{k}\left(\frac{2}{3}\boldsymbol{a}_1-\frac{1}{3}\boldsymbol{a}_2\right)} \tag{1.17}$$

where the positions of the neighbors are represented by the lattices in real space as shown in Figure 1-6(b).

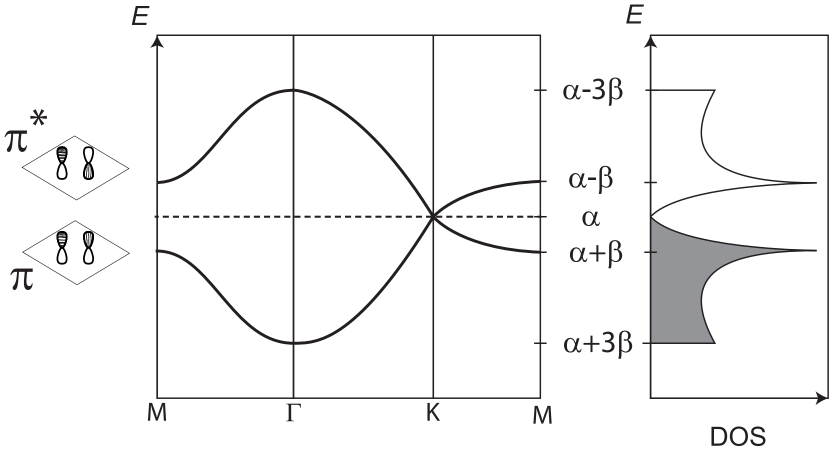

Figure 1-7: The band energy with respect to k for graphene. For the Fermi level, $E_{\mathrm{f}} = \alpha$.

In order to obtain $E(k)$ we solve the secular determinant, since

$$\begin{aligned} B^*B &= \left(e^{-i\mathbf{k}\left(\frac{1}{3}\boldsymbol{a}_1+\frac{1}{3}\boldsymbol{a}_2\right)} + e^{-i\mathbf{k}\left(-\frac{1}{3}\boldsymbol{a}_1+\frac{2}{3}\boldsymbol{a}_2\right)} + e^{-i\mathbf{k}\left(\frac{2}{3}\boldsymbol{a}_1-\frac{1}{3}\boldsymbol{a}_2\right)}\right) \\ &\times \left(e^{i\mathbf{k}\left(\frac{1}{3}\boldsymbol{a}_1+\frac{1}{3}\boldsymbol{a}_2\right)} + e^{i\mathbf{k}\left(-\frac{1}{3}\boldsymbol{a}_1+\frac{2}{3}\boldsymbol{a}_2\right)} + e^{i\mathbf{k}\left(\frac{2}{3}\boldsymbol{a}_1-\frac{1}{3}\boldsymbol{a}_2\right)}\right) \qquad (1.18) \\ &= 3 + 2\cos(\mathbf{k}\cdot\mathbf{a}_1) + 2\cos(\mathbf{k}\cdot\mathbf{a}_2) + 2\cos(\mathbf{k}\cdot(\mathbf{a}_1-\mathbf{a}_2)) \end{aligned}$$

the energy with $\mathbf{k}$ is

$$E(\mathbf{k}) = \alpha \pm \beta\sqrt{3 + 2\cos(\mathbf{k}\cdot\mathbf{a}_1) + 2\cos(\mathbf{k}\cdot\mathbf{a}_2) + 2\cos(\mathbf{k}\cdot(\mathbf{a}_1-\mathbf{a}_2))} \qquad (1.19)$$

When $\mathbf{k} = 0$, at which the symmetry point is Γ, the energy is the lowest and highest with $\alpha + 3\beta$ and $\alpha - 3\beta$, respectively. The lowest energy is a result from bonding orbitals (π) between two sublattices in a unit, while the highest energy is product of anti-bonding orbitals (π^*) as depicted the MOs in Figure 1-7.

The energy dispersion at near K points leads graphene to be intriguing matter. The π and π^* states are degenerate where the MOs from π and π^* are exactly same

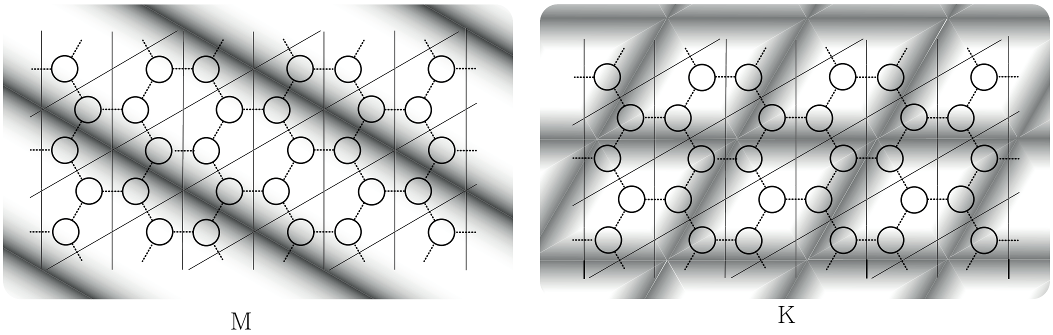

Figure 1-8: The phases of orbitals are represented in real space according to the wave vectors of the reciprocal lattices. Crest is depicted as bright and trough is described as dark for the wave at M and K points in the Brillouin zone of graphene.

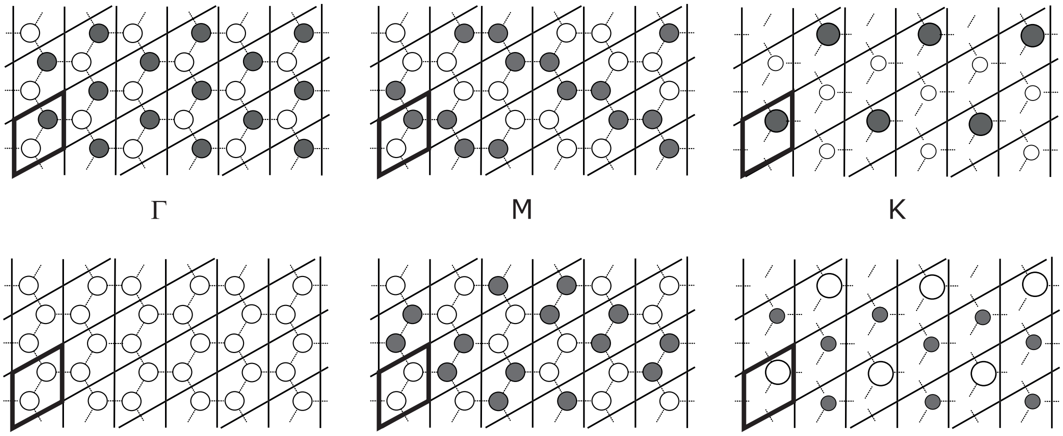

Figure 1-9: At Γ point, π and π^* unit cells are periodic with the invariant phase along the translation. When the reciprocal vector is on K point ($\mathbf{k} = \frac{2}{3}\mathbf{b}_1 + \frac{1}{3}\mathbf{b}_2$), the overall phases are same so that the state is degenerate.

after adopted by symmetry with K points. In addition, the energy level of graphene at K ($\mathbf{k} = \frac{2}{3}\mathbf{b}_1 + \frac{1}{3}\mathbf{b}_2$) matches the Fermi level as shown in Figure 1-7. Since the gap between valence and conduction band is zero, graphene is semimetallic. And the energy of electron is in proportion to $\sqrt{{k_1}^2 + {k_2}^2}$. For the reason, an electron transport is governed by Dirac's (relativistic) equation at K.[11] These K points are often called *Dirac point* and an electron is known for a massless Dirac fermion at the state.[§]

1.2.4 Graphene nanoribbon

Graphene nanoribbon is strip of graphene with a narrow width. The electronic states are determined by the edge structure where the symmetry of graphene is broken. Hydrogen atoms often cap the edges. The electrons of hydrogen atoms are in only 1s atomic orbitals. There is no p_z orbital to become π MOs. It is the reason for which the energy level of electronic state is different from the states on the carbon atoms that compose almost GNR.

Two types of nanoribbon are provided from graphene. The special edge structures are determined by the direction of cut as shown in Figure 1-10. Armchair graphene nanoribbon (AGNR) is cut out of graphene with edge where the structure seems like “armchair”. And zigzag graphene nanoribbon (ZGNR) is a strip of graphene in which the edge structures are “zigzag”.

After bonds are broken as the edge fragment are formed in the shape of zigzag or armchair, one of lattice vectors of graphene in real space vanishes by the breaking of translational symmetry and it turns into one-dimensional structure. The lattice vector should be along with $\mathbf{a}_1$ for ZGNRs, and the lattice vector should be along

---

[§] Starting with the relativistic equation due to Einstein

$$\mathscr{H} = (c^2p^2 + m^2c^4)^{1/2}$$

where c is the speed of light and m is the rest mass of the electron, and Dirac equation [77] is

$$i\hbar\frac{\partial\Psi}{\partial t} = (\alpha_1\, c\hat{p}_x + \alpha_2\, c\hat{p}_y + \alpha_3\, c\hat{p}_z)\,\Psi + \beta mc^2\Psi$$

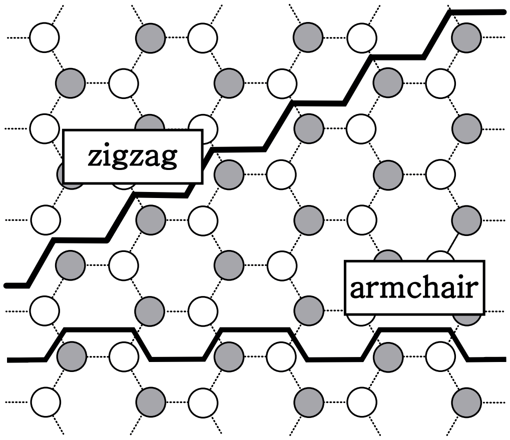

Figure 1-10: The direction of armchair edge is parallel to Γ → M and that of zigzag edge is related with Γ → K.

with $\mathbf{a}_1 + \mathbf{a}_2$ for AGNRs. Thus, the reciprocal lattice $\mathbf{b}'_1$ of GNRs is

$$\mathbf{b}'_1 = \begin{cases} 2\pi \dfrac{\mathbf{a}_1}{|\mathbf{a}_1|^2} & \text{for ZGNRs} \\ 2\pi \dfrac{\mathbf{a}_1 + \mathbf{a}_2}{|\mathbf{a}_1 + \mathbf{a}_2|^2} & \text{for AGNRs} \end{cases} \tag{1.20}$$

, however, there are not reciprocal lattices for $\mathbf{b}'_2$ or $\mathbf{b}'_3$, because GNRs are one-dimensional.

Moreover, as shown in Figure 1-11, an edge is differently consisting of sublattices by the structure. There are A and B sublattices in the primitive cell of graphene. The edge atoms are from A sublattices of graphene, in zigzag structure with breaking symmetry. Meanwhile, both A and B sublattices from graphene are the edge atoms and they are paired in armchair structure. Due to the zigzag structure, in particular, there are localized states at the edge of ZGNRs.

As a result of fragmentation, AGNRs are metallic or semiconducting, depending on the width. The longitudinal axis of AGNRs is related with M points in the

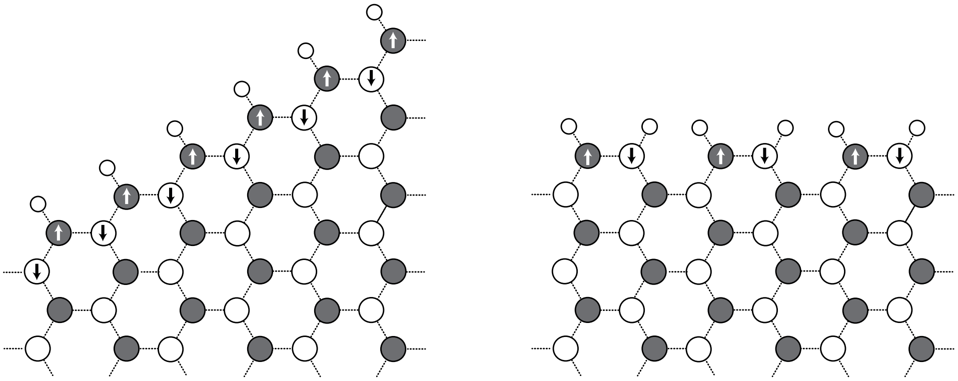
(a) Zigzag edge (b) Armchair edge

Figure 1-11: The structure of edge can break the symmetry of graphene's sublattice. (a) The edge atoms are A sublattices of graphene in zigzag structure, meanwhile (b) both A and B sublattices are the edge atoms and they are paired in armchair structure.

Brillouin zone of graphene as shown in Figure 1-10. Although the band of graphene have a gap as k varies from Γ to M, the Fermi level of ANGRs is above the band of π with a certain width. Meanwhile, the zigzag edge structure is related with K points in the Brillouin zone of graphene, the direction of Γ to K matches the longitudinal ribbon. The localized state at edge is near the Fermi level than states in the middle. And the energy of valence band is below the Fermi level in the ground state all the time. The gap between valence and conduction band is no longer zero.

1.2.5 Localized state in periodic boundary conditions and external electric field

GNRs are gathering attentions due to the unique properties to which GNRs are led by the edge structure and the functional groups. Our major issues are to tune GNRs by understanding the relations between the band structures through whole GNRs and the chemical interactions which occur locally in GNRs. Since the valence band

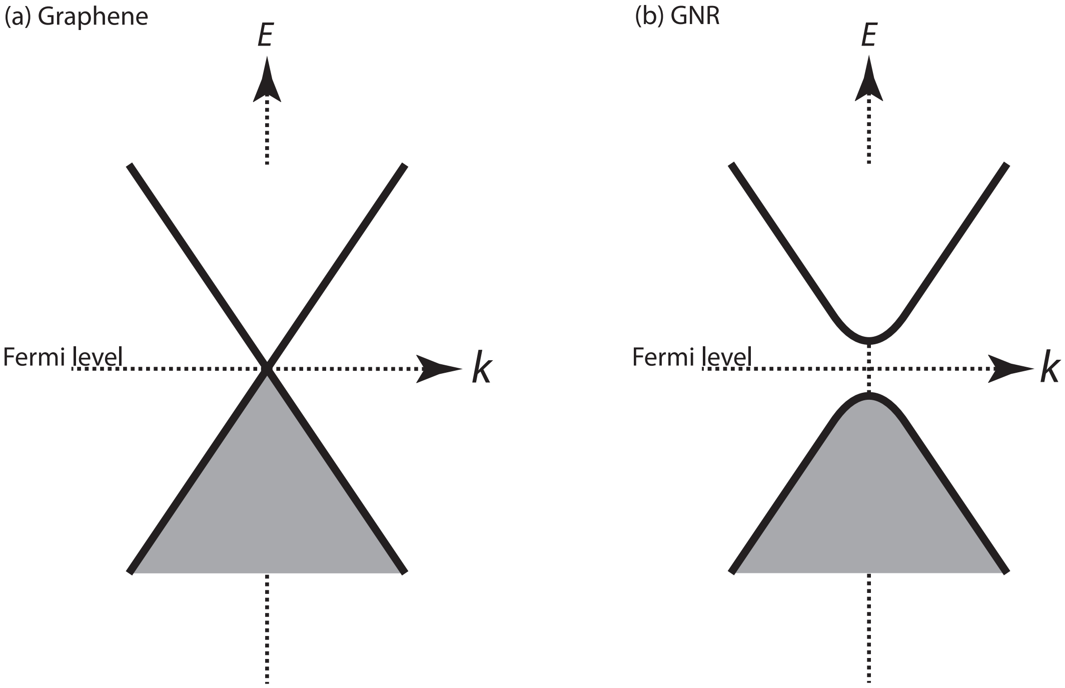

Figure 1-12: The energy dispersion is plotted for graphene and GNR. The gap is zero for graphene between valence and conduction band near the K points, meanwhile the gap is open for GNR along the k space with the longitudinal axis.

is related with the p_z orbitals of C atoms, in order to tune the electronic property of GNR, we studied not only the orbital energy but also chemical feature of p_z orbitals during the chemical reactions. By chemical reactions with covalent/non-covalent bonds, we may adjust the orbital energies, as a result of chemical reactions on GNR the band gap can be tuned. When the periodic electronic state of GNR is interacting with the localized states such as the orbitals of small molecules and functional groups, the band gap would be tuned as the bands are perturbed by introducing the electrons and the holes from the molecules and the functional groups, as in the scheme depicted in Figure 1-13.

In particular, the edge state is separated spatially in GNR with zigzag edge

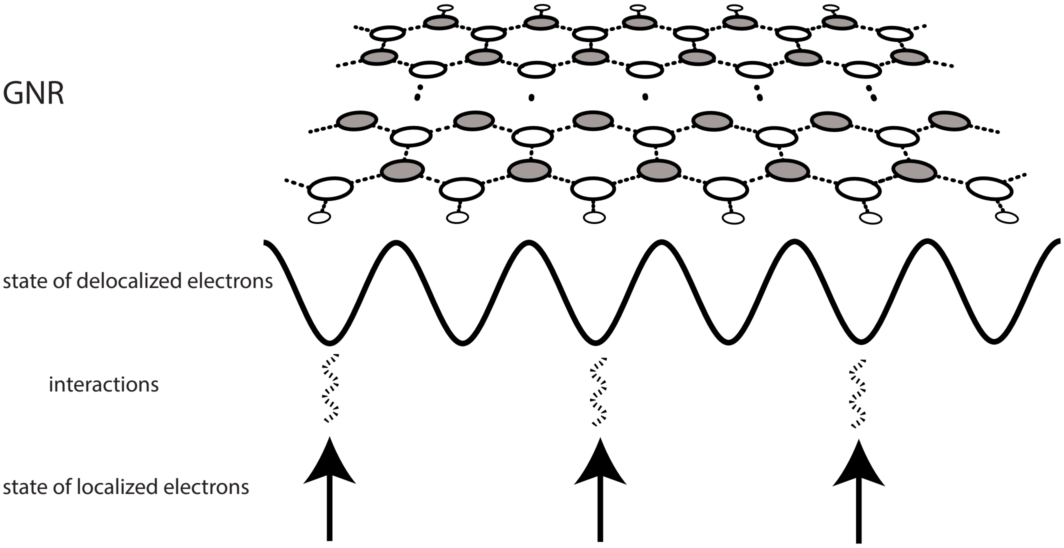

Figure 1-13: The state of localized electrons, in repeating of molecules along the GNR, interacts with the state of delocalized electrons in GNR.

structure (Figure 1-14(a)). If a different spin state is localized at each edge, the degeneration between α- and β-spin states would be broken, by the unbalanced population of the small molecule that is either electron donor or electron acceptor. It is represented schematically in Figure 1-14(b) that the electron and hole transfer to the band of GNR depending on the relative energy level of HOMO (E_{HOMO}) and LUMO (E_{LUMO}) of a molecule, against the energy level of valence band (E_{VB}) and conduction band (E_{CB}). If E_{HOMO} is higher than the lowest E_{CB}, subsequently $E_{\mathrm{HOMO}} > E_{\mathrm{f}}$, an electron may transfer from the HOMO into an empty band state. And if E_{LUMO} is lower than the highest E_{VB}, so $E_{\mathrm{LUMO}} < E_{\mathrm{f}}$, charge injection may proceed from the Fermi sea to the LUMO level. In other words, the holes may transfer from the LUMO into the band occupied by electrons. Furthermore, we applied a homogeneous electric field of which orientation is perpendicular to the periodic axis (Figure 1-14(c)). The electrons redistribute under an external electric field if the size of a system is finite along the direction of an electric field. For example, an isolated gas molecule is polarized in an electric field and the charge density at the surface in a slab are changed by a vertical electric field, because there can not exist a state to be occupied by electrons in vacuum. In the variation of external electric

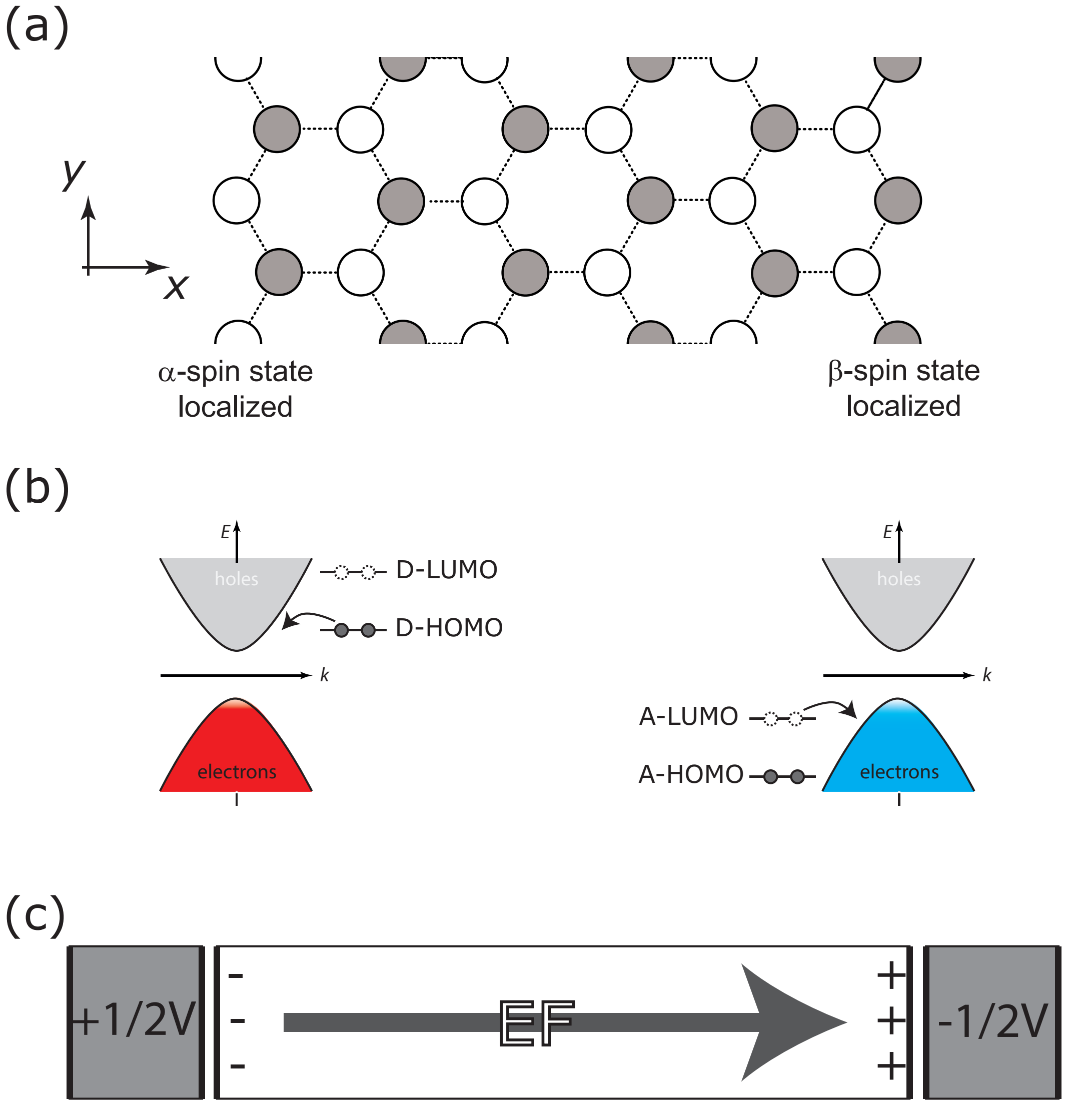
(a)
y
x
α-spin state localized
β-spin state localized
(b)
E
holes
D-LUMO
D-HOMO
k
electrons
E
holes
k
A-LUMO
A-HOMO
electrons
(c)
+1/2V
- - -
EF
+ + +
-1/2V

Figure 1-14: Tuning the band for a spin state. (a) The edge state is localized at an edge with zigzag structure. (b) The edge state is degenerate due to the spatial symmetry for the spin states. (c) A system is polarized by an electric field.

fields, the band structures were investigated with the energy shift by local interaction with molecular orbitals of electron donor and acceptor. The electronic structure and the total energy of a system would be discussed to unravel the role of localized orbitals and homogeneous electric field in terms of electric conductivity and chemical reactions by means of first principles.

Chapter 2

Theoretical Framework: Kohn-Sham equations and Bloch theorem

2.1 Introduction

In this chapter, we shall discuss details on the theoretical and computational methods to be used for the investigation of GNRs. Because our interests are the electronic structures and the properties of some state in the complex of GNRs, which are pristine GNR, chemically decorated GNR, or GNR absorbed by molecules, the systems should be dealt with at the level of quantum mechanics. It requires huge efforts and computing resources to solve Schrödinger equation with the exact wavefunctions of nuclei and electron, which are correlated each other in a system. However, we can approximate it to problems of uncoupled wavefunction depending on the time scale and the spatial scale. And we can use the equation of motion for individual electrons; this is single particle theory. Thus, we don't have to solve any equations simultaneously. Nonetheless, the description method can not help giving us some limits to which we can rely on and interpret the results. For this reason we are to review briefly what we based on, the theories and the methods.

2.2 The Born-Oppenheimer approximation

The states of a quantum mechanical system are vectors in a Hilbert space. This leads to the exponential growth of the dimensions with increasing number of particles. To describe a system which is made of nuclei and electrons is required necessarily that the dimension of many-body problem be reduced to the smaller subspace. Then, the properties are obtained by a simpler way within an acceptable accuracy.

Being interested in a system in the electronic ground state, we can separate the nuclei and electrons in mathematical problems. It is the *Born-Oppenheimer* (BO) approximation. Due to the much mass of a nucleus than that of an electron, the state of a nucleus can be considered being fixed. The electrons, in other words, relax instantaneously as the nuclei move even slower than electrons. Accordingly, the energy to be computed is the *adiabatic potential energy surface* of the atoms, for which we studied the properties and the reactions.

If we have M nuclei at positions $\mathbf{R}_1, \cdots, \mathbf{R}_M$, then we can define the electronic state for the position, X. And the electronic state depends parametrically on the nuclear position as a function is written by $X(\mathbf{R}_1, \cdots, \mathbf{R}_M)$. Moreover, we can express the ground state energy, E, as a function of positions of these nuclei, $E(\mathbf{R}_1, \cdots, \mathbf{R}_M)$ The electronic states are presumed to be uncoupled with the nuclear states. It is disregarded that the vibrationally nonadiabatic effects can contribute the electronic state by coupling between various states. From the approximation, we were able to study the features of the GNR complexes in which the adiabatic electronic states are determinant in the reaction.

2.3 Hartree-Fock and Kohn-Sham equations

The Hartree-Fock and density functional theory (DFT) methods provide the solution of the wavefunction for a many-body system. In the ground state the wavefunction of an individual electron is approximated to be uncorrelated with other electrons. The interaction is for the mean-field out of other electrons. Due to the computing efficiency for a system in periodic boundary conditions, we used DFT to calculate the state of the system.

2.3.1 Hartree-Fock (HF)

The atomic structures are described by solutions of the Schrödinger equation—precisely, it describes the adiabatic and non-relativistic state for a system. The time-independent Schrödinger equation is written as,

$$\hat{H}\Psi = E\Psi \tag{2.1}$$

where $\hat{H}$ is the Hamiltonian operator,

$$\hat{H} = \hat{T}_{nuc} + \hat{V}_{nn} + \hat{T}_{el} + \hat{V}_{ne} + \hat{V}_{ee} \tag{2.2}$$

in which

$$\hat{T}_{nuc} = \sum_{\alpha=1}^{M} \left(-\frac{\hbar^2}{2M_\alpha} \nabla_\alpha^2 \right) \tag{2.3}$$

is the kinetic energy operator for nuclei with the mass M_α of the nucleus α,

$$\hat{V}_{nn} = \sum_{\alpha=1}^{M} \sum_{\alpha<\beta} \frac{Z_\alpha Z_\beta}{R_{\alpha\beta}} \tag{2.4}$$

is the nucleus-nucleus repulsion energy,

$$\hat{T}_{el} = \sum_{i=1}^{N} \left(-\frac{\hbar^2}{2m} \nabla_i^2 \right) \tag{2.5}$$

is the kinetic energy operator for electrons with the mass m of a electron,

$$\hat{V}_{ne} = -\sum_{\alpha} \frac{Z_\alpha}{r_{i\alpha}} \tag{2.6}$$

is the external potential acting on electron i due to nuclei of charges Z_α, and

$$\hat{V}_{ee} = \sum_{i=1}^{N} \sum_{i<j} \frac{1}{r_{ij}} \tag{2.7}$$

is the electron-electron repulsive potential.

Since the wavefunction is expressed in terms of a wavefunction of the nuclei χ and of the electrons Φ, according to the BO approximation,

$$\Psi(\mathbf{r}, \mathbf{R}) = \chi(\mathbf{R})\Phi(\mathbf{r}; \mathbf{R}) \tag{2.8}$$

When we are interested in the situation where N electrons are interacting with multiple nuclei, by employing the BO approximation the more complete description of the Schrödinger equation for the electronic state is

$$\left[-\frac{\hbar^2}{2m} \sum_{i=1}^{N} \nabla_i^2 + \sum_{i=1}^{N} V(\mathbf{r}_i) + \sum_{i=1}^{N} \sum_{i<j} U(\mathbf{r}_i, \mathbf{r}_j) \right] \Phi(\mathbf{r}; \mathbf{R}) = E\Phi(\mathbf{r}; \mathbf{R}) \tag{2.9}$$

In this equation, $\mathbf{r}_i$ indicates the all (space and spin) coordinates of the ith electron. And we obtain the expectation energy for the electronic state as,

$$E_{\mathrm{el}} = \langle \Phi | \hat{H}_{\mathrm{el}} | \Phi \rangle \tag{2.10}$$

For the Hamiltonian, so far, Φ is the electronic wavefunction that is a function of the state of the whole electrons of the system, written as

$$\Phi = \Phi(\mathbf{r}_1, \cdots, \mathbf{r}_N) \tag{2.11}$$

In order to solve the energy and the state of the electrons, the Hartree-Fock method is a central starting point to approximate the quantum many-body system. The method is based on the simple approximation to the many-body system.

The electron was considered as a spinless particle in Eq. 2.7. But an electron is a fermion with half-integer spin. Two identical electrons cannot be simultaneously in the same state. As the many-fermion wavefunction has to be antisymmetric upon particle exchange, the wavefunction is expressed by a Slater determinant of N spin-orbitals. If the spin-orbitals depict the state of each electron: $\phi_1, \phi_2, \cdots, \phi_N$, then Φ^{HF} can be written as,

$$\Phi^{\mathrm{HF}} = \frac{1}{\sqrt{N!}} \begin{vmatrix} \phi_1(\mathbf{x}_1) & \phi_1(\mathbf{x}_2) & \cdots & \phi_1(\mathbf{x}_N) \\ \phi_2(\mathbf{x}_1) & \phi_2(\mathbf{x}_2) & \cdots & \phi_2(\mathbf{x}_N) \\ \vdots & \vdots & & \\ \phi_N(\mathbf{x}_1) & \phi_N(\mathbf{x}_2) & \cdots & \phi_N(\mathbf{x}_N) \end{vmatrix} \tag{2.12}$$

where the $\mathbf{x}$ variables include the coordinates of space and spin. The wavefunction Φ is approximated as a product of an individual electron. This wavefunction may be inserted Eq. 2.10 reducing the many-body problem to a set of one- and two-electron equations.

Employing the *variational theorem*, if we minimize the E_{el} by seeking the wavefunction in a self-consistent field method, we can solve the energy in the ground state that is the minimum E_{el} in Eq. 2.10. Thus, the Hartree-Fock energy is

$$E_{\mathrm{el}}^{\mathrm{HF}} = \underset{\Phi}{min} \left\langle \Phi^{\mathrm{HF}} | \hat{T} + \hat{V}_{ee} + \hat{V}_{\mathrm{ext}} | \Phi^{\mathrm{HF}} \right\rangle \tag{2.13}$$

where the first contribution is the non-interacting kinetic energy of the many orbitals, and the second is two-electron contribution as $\hat{V}_{ee} = \hat{J} - \hat{K}$. It is defined in terms of their action on the spin orbitals by the Coulomb($\hat{J}$) and exchange($\hat{K}$) operator:[78]

$$\hat{J}_j \phi_i(\mathbf{x}_2) = \left(\int \phi_j^*(1) \frac{1}{\mathbf{r}_{12}} \phi_j(1) d\mathbf{x}_1 \right) \phi_i(\mathbf{x}_2) \tag{2.14}$$

$$\hat{K}_j \phi_i(\mathbf{x}_2) = \left(\int \phi_j^*(1) \frac{1}{\mathbf{r}_{12}} \phi_i(1) d\mathbf{x}_1 \right) \phi_j(\mathbf{x}_2) \tag{2.15}$$

and the last $\hat{V}_{ext}$ in the Eq. 2.13 is external potential energy.[78,79]

However, as a system involves more atoms, we have to confront a number of two-electron integrals such as Coulomb and exchange energy. In addition to the number, their integration over spatial orbitals require much more computing resources such as CPUs and RAMs. In the followings, the density functional theory (DFT) is to be introduced. This is often used for GNRs due to computational advantages compared to HF and post-HF methods of comparable quality.

2.3.2 Density Functional Theory (DFT)

Given an exact ground-state wavefunction with N electrons as Eq. 2.11, the electronic density can be calculated by

$$\rho(\mathbf{r}) = N \int d^3r_2 \int d^3r_3 \cdots \int d^3r_N \Phi^*(\mathbf{r}, \mathbf{r}_2, \cdots, \mathbf{r}_N) \Phi(\mathbf{r}, \mathbf{r}_2, \cdots, \mathbf{r}_N) \tag{2.16}$$

This quantity is of great importance in *Density Functional Theory* (DFT). The DFT is to replace the complicated N-electron wavefunction $\Phi(\mathbf{r}_1, \mathbf{r}_2, \cdots, \mathbf{r}_N)$ and the associated Schrödinger equation by the simpler electron density $\rho(\mathbf{r})$ and its associated calculation scheme.[80–82]

For an N-electron system at the ground state, the external potential $v(\mathbf{r})$—this is not restricted to Coulomb potentials—completely fixes the Hamiltonian; thus N and $\upsilon(\mathbf{r})$ determine all properties for the ground state. In other words, $\upsilon(\mathbf{r})$ defines the whole nuclear frame for a molecule, which together with a number of electrons determine all the electronic properties.

The proof of the first Hohenberg-Kohn theorem[83] legitimizes the use of electron density $\rho(\mathbf{r})$ as basic variable to describe the electronic state for the system. Since ρ determines the number of electron, it follows that $\rho(\mathbf{r})$ also determines the ground-state wavefunction Φ and all other electronic properties of the system. For example, the kinetic energy $T[\rho]$, the potential energy $V[\rho]$, and the total energy $E[\rho]$ are computed by the electron density ρ. Making E to be dependent explicitly on υ, we combine the decomposed functionals to write E_υ,

$$\begin{aligned} E_\upsilon[\rho] &= T[\rho] + V_{ne}[\rho] + V_{ee}[\rho] \\ &= \int \rho(\mathbf{r})\upsilon(\mathbf{r})d\mathbf{r} + F_{\mathrm{HK}}[\rho] \end{aligned} \tag{2.17}$$

where

$$F_{\mathrm{HK}}[\rho] = T[\rho] + V_{ee}[\rho] \tag{2.18}$$

We can calculate the energy of the system which is defined by the external potentials.

And the second Hohenberg-Kohn theorem[83] provides the energy variational principle. For a trial density $\rho'(\mathbf{r})$, such that $\rho'(\mathbf{r}) \geq 0$ and $\int \rho'(\mathbf{r})d\mathbf{r}$ =N,

$$E_\upsilon[\rho'(\mathbf{r})] = F_{\mathrm{HK}}[\rho'(\mathbf{r})] + \int \upsilon_{\mathrm{ext}}(\vec{r})\rho'(\mathbf{r})d(\vec{r}) \geq E_0 \tag{2.19}$$

where $E_\upsilon[\rho'(\mathbf{r})]$ is the energy functional, and E_0 is the ground-state energy. If we can minimize $E_\upsilon[\rho'(\mathbf{r})]$, we obtain $\rho(\mathbf{r})$ at the ground state.

If we note that F_{HK} of Eq. (2.18) is defined independently of the external potential $\upsilon(\mathbf{r})$, subsequently, we may be aware of that F_{HK} is a universal functional of $\rho(\mathbf{r})$. Once we have an explicit form for $F_{\text{HK}}[\rho]$, we can apply it to any system. However, it is difficult to achieve the explicit form of $F_{\text{HK}}[\rho]$, because the problem is for many-particle system.

Kohn and Sham[84] approximated the many-body problem by mapping the full interacting system with the real potential onto a non-interacting system with the effective potential. The exact ground-state density is represented by the ground-state density of an auxiliary system of non-interacting particles, which is so-called *non-interacting* υ*-representability.*

The Kohn-Sham equations have the form

$$\left[-\frac{\hbar^2}{2m}\nabla^2 + V(\mathbf{r}) + V_H(\mathbf{r}) + V_{XC}(\mathbf{r})\right]\phi_i(\mathbf{r}) = \epsilon_i\phi_i(\mathbf{r}) \tag{2.20}$$

where

$$V_H(\mathbf{r}) = \int \frac{\rho(r')}{|\mathbf{r}-\mathbf{r}'|}d^3r' \tag{2.21}$$

is called Hartree potential which describes the Coulomb repulsion between a electron and the mean-field of electrons. For this reason the Hartree potential includes self-interaction contributions. To account for the other effects in the real system, exchange and correlation contribution is defined as a functional derivative of the exchange-correlation energy:

$$V_{XC}(\mathbf{r}) = \frac{\delta E_{XC}(\mathbf{r})}{\delta\rho(\mathbf{r})} \tag{2.22}$$

Though theses equations are similar to Eq. (2.9), it is different from the full Schrödinger equation that the Kohn-Sham equation has no summations. Because the wavefunction in the Kohn-Sham equation is for single particle, it is a locally unique solution by the fictitious external potential. As a consequence, the Kohn-Sham DFT then looks formally like a single-particle theory, although many-body effects are still included via the so-called exchange-correlation functional. The density functional approach can be summarized by the statement that the knowledge of $\rho(\mathbf{r})$ implies the knowledge the wavefunction and the potential, and hence of all other observables.[85]

Exchange-correlation functional

To solve Kohn-Sham equations, we have to specify $V_{XC}[\phi_i]$. In fact, the true form of the exchange-correlation functional is not known for a many-body system yet. Although the equation is not derived exactly, the approximated $V_{XC}[\phi_i]$ have reproduced successfully experimental results.[86–89]

The local density approximation (LDA) is the simplest method, on which all approximate exchange-correlation functionals are based. The center of this idea is a hypothetical *uniform electron gas*. The charge density $\rho(\mathbf{r})$ is assumed to be constant. This is a system in which electrons move on a positive background charge distribution such that the total ensemble is electrically neutral. Physically, such a situation resembles the model of an idealized metal consisting of a perfect crystal of valence electrons and positive cores where the cores are smeared out to arrive at a uniform positive background charge.[84] This approach reproduces the results of experiments for calculations on solids. It has proven particularly successful to determination of properties such as equilibrium structures, harmonic frequencies or charge moments.[86,90–92]

Nonetheless, the LDA is poor at producing the binding energies of molecules. The overbinding tendency of the LDA can be rationalized in terms of the exchange hole properties. Since the LDA hole is spherically symmetric, the moderate accuracy is obtained by employing the information of $\nabla\rho(\mathbf{r})$ (the *gradient* of the charge density) into exchange-correlation functionals. It is known as generalized gradient approximations (GGAs).[93,94] Furthermore, a hierarchy of functionals can be constructed that gradually include more and more detailed physical information.

We adopted PBE functional[94,95] which is one of GGAs to study on GNRs. The functional with planewave basis sets is implemented in VASP (Vienna ab-initio simulation package)[96–98], and the result of this method is consistent with experimental results in the energetics of molecular systems, with error of less than a few kcal/mol for molecular systems.[99]

Although the methods produce results within reasonable accuracy with the requirement for less computing resources, it often fails to reproduce the energy for physisorption in which the interactions are primarily attributed to van der Waals forces between a molecule and a GNR. It underestimates the energy, because GGA functionals are of local charge density and the gradient charge density. Grimme suggested, in order to recover dispersive interaction, semiempirical GGA-type density functional constructed with a long-range dispersion correction.[100] The energy of DFT-D2 is

$$E_{\text{DFT-D2}} = E_{\text{Kohn-Sham}} + E_{\text{disp}} \tag{2.23}$$

The van der Waals interactions, which are the defects in GGA functionals, are defined by a simple pair-wise force field.

$$E_{\text{disp}} = -\frac{s_6}{2}\sum_{i=1}^{N_{at}}\sum_{j=1}^{N_{at}}\sum_{L}{}' \frac{C_6^{ij}}{\left|\mathbf{r}^{i,0}-\mathbf{r}^{j,L}\right|^6} f\left(\left|\mathbf{r}^{i,0}-\mathbf{r}^{j,L}\right|\right) \tag{2.24}$$

where the summations are over all N_{at} atoms and all translations $L(l_1, l_2, l_3)$ of the unit cell, s_6 is global scaling depending on the kind of DFT functional, C^{ij} is the dispersion coefficient for the atom pair ij, and the $f(r_{ij})$ is a damping function of which role is to scale the force field. This damping function minimize the dispersive energy within typical bond length.

External electric field

In DFT, the ground-state electronic state is determined by the external potential. This is arising due to not only the nuclei but also any other external sources such as external electric field or magnetic field. The unique functional $E_{\upsilon}[\rho(\mathbf{r})]$ for the electron density $\rho(\mathbf{r})$ in Eq. 2.17 can be rewritten in a homogeneous external electric field by a finite strength,

$$\begin{aligned} E_{\upsilon}[\rho] &= T[\rho] + V_{ne}[\rho] + V_{\text{ext}}[\rho] + V_{ee}[\rho] \\ &= \int \rho(\mathbf{r})\upsilon(\mathbf{r})d\mathbf{r} + F_{\text{HK}}[\rho] \end{aligned} \tag{2.25}$$

where $V_{\text{ext}}[\rho]$ is the potential by the external field.

However, due to the periodic boundary conditions, the total energy converges slowly with respect to the size of the supercell, but also the potential and the forces are affected by finite size errors. The effect is counterbalanced by a linear electrostatic potential that is added to the local potential, correcting the errors introduced by periodic boundary.[101] The external electric potential applied in a supercell is saw-tooth potential. The longer slope of the saw-tooth crosses the basal plane of the GNR, creating the additional electric field on its opposite sides. The shorter backward slope is introduced in the vacuum region in order to make the $V_{\text{ext}}(\mathbf{r})$ periodic.

This method is not appropriate for bulk systems. The polarization in a bulk system is not trivial in periodic boundary conditions. Because it is ambiguous how a certain electron is paired with a nuclei. The polarization is obtained by means of Berry phase.[102–106]

We applied an external electric field in a vertical direction against the longitudinal axis of the GNR. For instance, in a supercell, if the C atoms of a GNR were arranged along the y-axis, the electric field was in the x- or z-axis. And, along the x- and z-axis, the orbital overlaps between the neighboring GNRs were avoided by vacuum. Since the saw-like electric potential can be applied in the direction, at the vacuum the short-opposite electric field was applied periodically, except for the longitudinal axis of the GNR.

2.4 Reciprocal space and k-points

2.4.1 Reciprocal space

GNRs have the geometric feature in which C atoms are bonded with the next C atoms in sp^2 hybridization infinitely, and it is quasi-one-dimensional structure. The positions of atoms are defined as repeated periodically along an axis. If we are to tackle the problem in such real space, it is cumbersome to solve the function for the system. Because there are an infinite numbers of atoms to be considered, a number of functions for the atoms are formidably large.

In a case in which the atoms are ordered with a translational symmetry, as the problem of open chain was solved, we can solve the problem in reciprocal space, in an easier approach.[107–110] They can be treated effectively as infinite. We defined the shape of the supercell which is repeated periodically by lattice vectors $\mathbf{a}_1$, $\mathbf{a}_2$, and $\mathbf{a}_3$, in general. The set of all translations forms a lattice in space, in which the translation can be written as integral multiples of the primitive translation vectors, $\mathbf{a}_i$,

$$\mathbf{T}(\mathbf{n}) \equiv \mathbf{T}(n_1, n_2, n_3) = n_1\mathbf{a}_1 + n_2\mathbf{a}_2 + n_3\mathbf{a}_3 \tag{2.26}$$

Then any function $f(\mathbf{r})$ defined for the crystal, such as the density of electrons or the electronic wavefunction of an atom, is the same in each unit cell,

$$f(\mathbf{r} + \mathbf{T}(n_1, n_2, n_3)) = f(\mathbf{r}) \tag{2.27}$$

This periodic function can be represented by Fourier transforms in terms of Fourier components at wave vectors $\mathbf{q}$ defined in reciprocal space,

$$f(\mathbf{q}) = \frac{1}{\Omega}\int_{\Omega} d\mathbf{r} f(\mathbf{r})\, e^{i\mathbf{q}\cdot\mathbf{r}} \tag{2.28}$$

in which $\Omega = |\mathbf{a}_1 \cdot (\mathbf{a}_2 \times \mathbf{a}_3)|$, this is the volume of the unit cell.

In order to solve the Schrödinger equation, the solution has to follow Bloch's theorem,

$$\phi_{\mathbf{k}}(\mathbf{r}) = e^{i\mathbf{k}\cdot\mathbf{r}} u_{\mathbf{k}}(\mathbf{r}) \tag{2.29}$$

then wavefunctions with $\mathbf{k}'$ vectors outside the first Brillouin zone (BZ)—primitive cell in reciprocal space—can be rewritten in the form of $\mathbf{k}$ in the first BZ, the $\mathbf{k}$ is allowed by

$$\mathbf{k} = \mathbf{k}' + \mathbf{G} \tag{2.30}$$

where $\mathbf{G} = n_1\mathbf{b}_1 + n_2\mathbf{b}_2 + n_3\mathbf{b}_3$ are the reciprocal lattice vectors, and the primitive

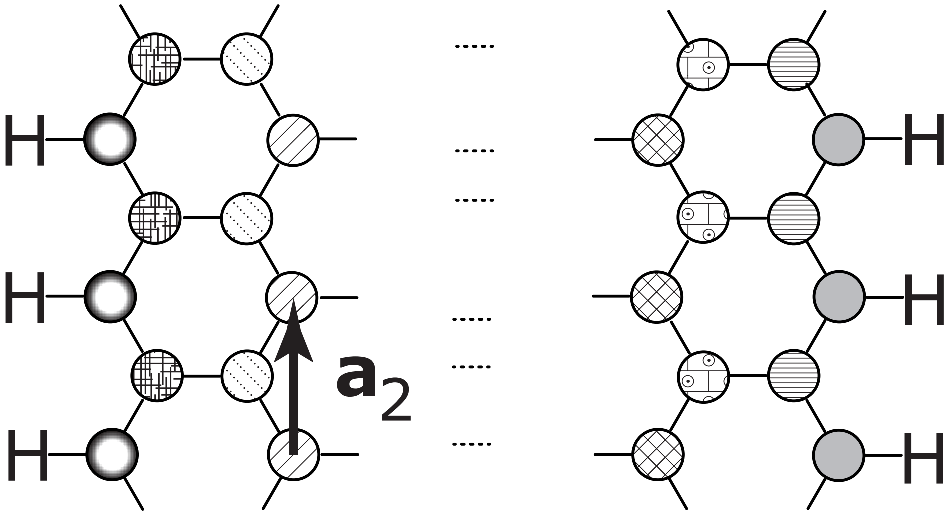

Figure 2-1: H atoms cap the ZGNR. The same pattered circles indicate identical C atoms in the periodic boundary condition with the primitive lattice vector $\mathbf{a}_2$. The other primitive lattices are omitted due to the length of arrows, including vacuum in the unit cell. The translation primitive vector $\mathbf{a}_1$ goes from the left to the right, and the $\mathbf{a}_3$ comes out of the paper in the right angle to the other axes.

vectors ($\mathbf{b}_1, \mathbf{b}_2, \text{and } \mathbf{b}_3$) in reciprocal space are defined,

$$\mathbf{b}_1 = 2\pi \frac{\mathbf{a}_2 \times \mathbf{a}_3}{|\mathbf{a}_1 \cdot (\mathbf{a}_2 \times \mathbf{a}_3)|}, \quad \mathbf{b}_2 = 2\pi \frac{\mathbf{a}_3 \times \mathbf{a}_1}{|\mathbf{a}_2 \cdot (\mathbf{a}_3 \times \mathbf{a}_1)|}, \quad \mathbf{b}_3 = 2\pi \frac{\mathbf{a}_1 \times \mathbf{a}_2}{|\mathbf{a}_3 \cdot (\mathbf{a}_1 \times \mathbf{a}_2)|} \tag{2.31}$$

To give an instance, the schematic ZGNR is in Figure 2-1. The identical C atoms are described by the same patterns. They are repeated by the translation primitive vector $\mathbf{a}_2$ along the periodic axis. Then, the $\mathbf{k}$ vectors can be interpreted in real space, as shown in Figure 2-2, as the magnitude of the phase difference between neighboring orbitals in periodic boundary condition. At $\mathbf{k}_2 = 0$, the phases of p_z orbitals are constant. Meanwhile, as $\mathbf{k}_2$ increases the distance between nodes decrease. As $\mathbf{k}_2$ is at the boundary of the first BZ ($\mathbf{k}_2 = \frac{1}{2}\mathbf{b}_2 = \frac{\pi}{\mathbf{a}_2}$), the phase of a p_z orbital is out-of-phases with those of the neighbor orbitals.

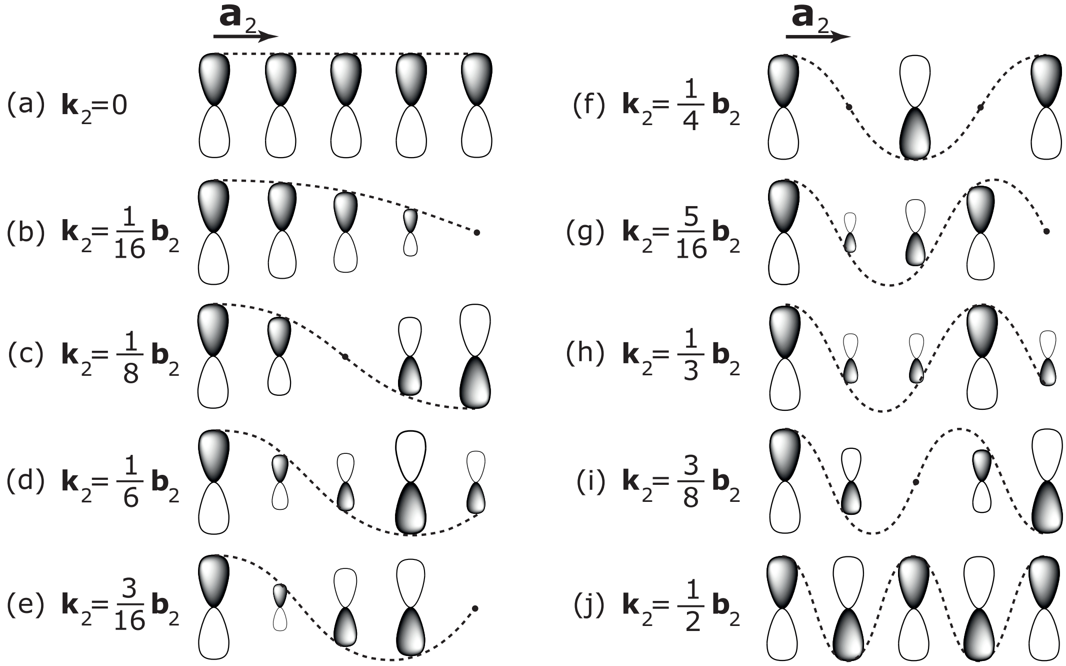
$\mathbf{a}_2$
$\mathbf{a}_2$
(a) $\mathbf{k}_2=0$
(b) $\mathbf{k}_2=\frac{1}{16}\mathbf{b}_2$
(c) $\mathbf{k}_2=\frac{1}{8}\mathbf{b}_2$
(d) $\mathbf{k}_2=\frac{1}{6}\mathbf{b}_2$
(e) $\mathbf{k}_2=\frac{3}{16}\mathbf{b}_2$
(f) $\mathbf{k}_2=\frac{1}{4}\mathbf{b}_2$
(g) $\mathbf{k}_2=\frac{5}{16}\mathbf{b}_2$
(h) $\mathbf{k}_2=\frac{1}{3}\mathbf{b}_2$
(i) $\mathbf{k}_2=\frac{3}{8}\mathbf{b}_2$
(j) $\mathbf{k}_2=\frac{1}{2}\mathbf{b}_2$

Figure 2-2: Schematic illustration of Bloch states of repeated p_z orbitals in one dimension is depicted depending on the $\mathbf{k}_2$ vectors. The each orbital is on an identical C atom in periodic boundary conditions; the same pattern depict them. The envelope is the smooth function that multiplies a periodic array of p_z orbital functions of C atoms, and the coefficients attribute to the size of the orbitals.

According to the Bloch's theorem, the calculation of the wavefunctions for all electrons in the infinitely periodic system can be mapped onto the calculation of the wavefunctions for a finite number of electrons in the unit cell by a infinite number of **k** vectors. Even though an infinite number of **k** vectors can be chosen to carry out the eigenstates, only a finite number of **k** vectors can be sampled. Because nearby **k** vectors put through similar information, it is possible to reproduce the observations to the desired accuracy, by using the wavefunctions with a finite number of the **k** vectors chosen in the first BZ with rationale.

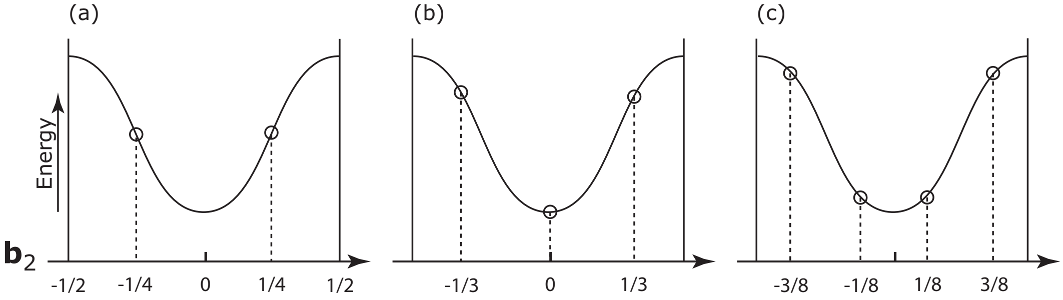

Figure 2-3: A band energy varies with respect to wave vector k in the first BZ. By the Monkhorst-Pack method, the sampled k-points are marked by empty circles. When N_2 = (a) 2, (b) 3, and (c) 4 are given, the efficient points are chosen at uniform grids in reciprocal space. At the k-points the Bloch wavefunctions are integrated.

2.4.2 Brillouin zone sampling

The state of a system, which is in periodic boundary conditions, can be expressed by the Bloch wavefunctions over all $\mathbf{k}$ vectors in the first BZ. Evaluation of many quantities of the system, such as energies and density, requires to sum over the Bloch wavefunctions. The measurement per unit cell is carried out by dividing the sum over the states by the number of $\mathbf{k}$ vectors. Since the relevant sums over all filled bands are smooth so long as all bands concerned as filled, special points can be chosen for efficient integration of smooth periodic function.[111,112]

The general method proposed by Monkhorst and Pack[111] was used during our computation. Because it leads to a uniform set of points determined by a simple formula valid for any crystal. Before calculations it should be specified only how many k-points to be used. If N_i k_i-points are sampled to sum the Bloch wavefunctions :

$$\mathbf{k}_{n_1,n_2,n_3} \equiv \sum_{i}^{3} \frac{2n_i - N_i - 1}{2N_i} \mathbf{b}_i \tag{2.32}$$

where $n_i = 1, 2, \cdots, N_i$, and $\mathbf{b}_i$ are the primitive vectors of the reciprocal lattice.

Due to the geometric feature of GNR with vacuum in real space, we chose the multiple k-points for a periodic direction $\mathbf{a}_2$ as shown in Figure 2-1; only Γ point ($\mathbf{k}_i$=0) is considered for two other non-periodic directions, since $\mathbf{b}_1$ and $\mathbf{b}_3$ are so small that one $\boldsymbol{k}$ point is enough. According to the Monkhorst-Pack method, for example, when $N_2 = 2$ the state with $\mathbf{k}_2 = \pm\frac{1}{4}\mathbf{b}_2$ is sampled. If there is a p_z orbital in a unit cell, the state can be described as shown in Figure 2-2(f). In the case of $N_2 = 3$, a vector $\mathbf{k}_2 = 0$ (Figure 2-2(a)) and two vectors $\mathbf{k}_2 = \pm\frac{1}{3}\mathbf{b}_2$ (Figure 2-2(h)) are the sampled k-points. Two Bloch states $\mathbf{k}_2 = \pm\frac{1}{8}\mathbf{b}_2$ (Figure 2-2(c)) and two other states $\mathbf{k}_2 = \pm\frac{3}{8}\mathbf{b}_2$ (Figure 2-2(i)) are integrated with $N_2 = 4$. The magnitude of the error introduced by sampling the BZ integral with a finite number of k-points can always be reduced by using a denser set of points.

Chapter 3

Computational Studies on the Properties of Pristine GNRs

Graphene is semimetallic with zero band gap. This is attributed to the hexagonal networks of sp^2 hybrid orbitals of C atoms. A p orbital (p_z) is oriented perpendicularly to the graphene plane. The highest valence band comprises this orbital. At the K points, the energy of π and π^* is degenerate with zero gap. In the meantime, as the graphene is chopped and turned into quasi-one-dimensional nanoribbon, the band gap is opening. Since the reciprocal space is no longer two dimensions for GNRs, of which unit cell is composed by multiple C and H atoms, the energy level of band is adopted by the new symmetry.

The structure of GNRs is significant to tune the electronic properties, since the band structure is related with the arrangement how the atoms are repeated. Adopting new symmetry in reciprocal space, the band energy is shifted by the change of the energy of bonding orbitals between edge atoms and by the reciprocal wave vector k. The highest valence band is from the p_z orbitals on C atoms for a conjugate bond system. As we would discuss, it is worth investigating the p_z orbitals to understand the band structure near the Fermi level according to the symmetry in reciprocal space.

Moreover, in order to determine the geometric, electronic, and magnetic structures of GNR, the fundamental factors such as lattice related parameters and magnetic moments would be discussed for our model systems of which results are computed using DFT. This may verify the value of the results of the adjustment of the total energy and the band structure by chemical modifications, in comparisons.

3.1 Computational details: preliminary calculations

In a periodic system, a *primitive cell* comprises of the atoms and the primitive bases for the direct lattice. Then, the atoms were repeated as the unit cell were translated periodically by the given periodic boundary conditions. So, as planewaves were used as basis sets in DFT calculations, we should specify deliberately some parameters which is related the periodic boundary conditions.

3.1.1 Lattice constants

Periodic carbon atoms consist of GNRs. The lattice parameter along the periodic axis is the constant distance between unit cells. This specifies the distance between repeated atoms as well. We were able to optimize the three lattice parameters, but the matter was whether we could choose those with the fictitious vacuum. If we optimize the cell as the total energy is the minimum per unit cell, the vacuum volume would down to some extent at which GNRs are stacked with each other as if they aggregate by van der Waals forces.

For the reason, we adopted the lattice parameter from the perfectly hexagonal graphene as shown in Figure 3-1(a). And the vacuum over the plane was 20 Å as a constant. In a case of GNRs, there is vacuum along two axes but for a periodic axis. For two-dimensional graphene, the vacuum is required along one less axis, so there is only the vacuum by which the basal plane is discrete in the periodic boundary condition. Furthermore, we are able to free from the problem of H atoms with which GNR is terminated. If we had to find the appropriate lattice parameter, with C−H bonds at the edges, we should have optimized the C−H bond lengths at every lattice constant, at least. Although a GNR has edges, as the width of a GNR is wider, consequently, the C$-$C lengths will be converge to the bond length of graphene.

The supercell was composed by 32 C atoms with the perfectly hexagonal network. And we found the total energy is the minimum at the C$-$C bond length of 1.422 Å. This length is consistent with experiments of graphene where there was no charge density variation.[113] Thus, as the length was taken to be the reference of lattice parameters during our calculation, we have had the primitive lattice vector $\mathbf{a}_2$ in real space to be 2.462 Å in the y-axis for ZGNRs.

3.1.2 Planewave cutoff

When a periodic part $u_{n\mathbf{k}}$ of a unit cell is given, where n states the band n and $\mathbf{k}$ is the Bloch wave vector, the wavefunction is—according to the Bloch theorem,

$$\phi_{n\mathbf{k}}(\mathbf{r}) = u_{n\mathbf{k}} e^{i\mathbf{kr}} \tag{3.1}$$

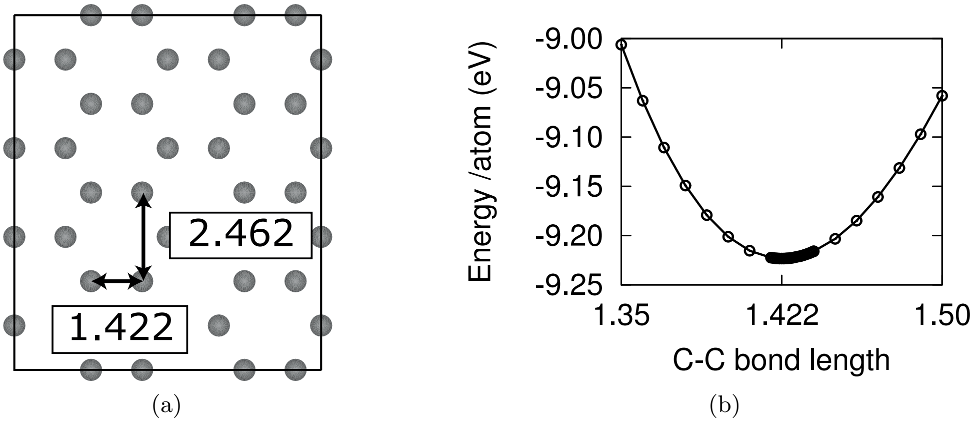

(a) (b)

Figure 3-1: The calculation was performed with PBE functional and 400 eV cutoff energy, and $13 \times 13 \times 1$ k-points are sampled by Monkhorst-Pack grids. The bond length was subject to the lattice constant, as the locations of C atoms were determined with the proportion of lattice constants. The lengths are written in Å. (a) The 32 C atoms were arranged with perfectly hexagonal network in a supercell. (b) The energy of supercell is dependent on the C$-$C bond length.

with $u_{n\mathbf{k}}(\mathbf{r}+\mathbf{R}) = u_{n\mathbf{k}}(\mathbf{r})$. Then, since $\mathbf{k}$ is usually constrained within the first BZ in reciprocal space, the wavefunction can be written as a sum of planewaves

$$\phi_{n\mathbf{k}}(\mathbf{r}) = \sum_{\mathbf{G}} c_{n(\mathbf{k}+\mathbf{G})} e^{i(\mathbf{k}+\mathbf{G})\mathbf{r}} \tag{3.2}$$

As the wavefunctions are solutions of the Schorödinger equation, the solutions with lower energies are more physically important. Because the higher energy of an atom is attributed to core electrons and the lower energy is contributed to valence electrons, the lower energies are much dependent on a system. Meanwhile, core electrons are so tightly bound to nucleus as to be negligibly perturbed by the chemical bonds. The higher energies, in addition, is not different from those of other system. Then, instead the infinite sum over all reciprocal lattice vectors $\mathbf{G}$, we can reduce as[108–110]

$$\phi_{n\mathbf{k}}(\mathbf{r}) = \sum_{|\mathbf{G}+\mathbf{k}|<G_{\text{cut}}} c_{n(\mathbf{k}+\mathbf{G})} e^{i(\mathbf{k}+\mathbf{G})\mathbf{r}} \tag{3.3}$$

in which G_{cut} is the upper limit of the reciprocal wave vector, and $(\hbar^2/2m_e)\,|G_{\text{cut}}|$ is the energy cutoff. This should be chosen according to the pseudopotential.

PAW potentials

Core electrons are tightly bound to the nucleus, so as the electrons are spatially strong localized. To describe exactly the potential requires higher reciprocal lattice vector $\mathbf{G}$. Pseudopotential replaces the electron density from a chosen set of core electrons with smoothed density chosen to match various important physical and mathematical properties of the true ion core. Therefore, the cutoff energies can be reduced accordingly by this pseudopotential.

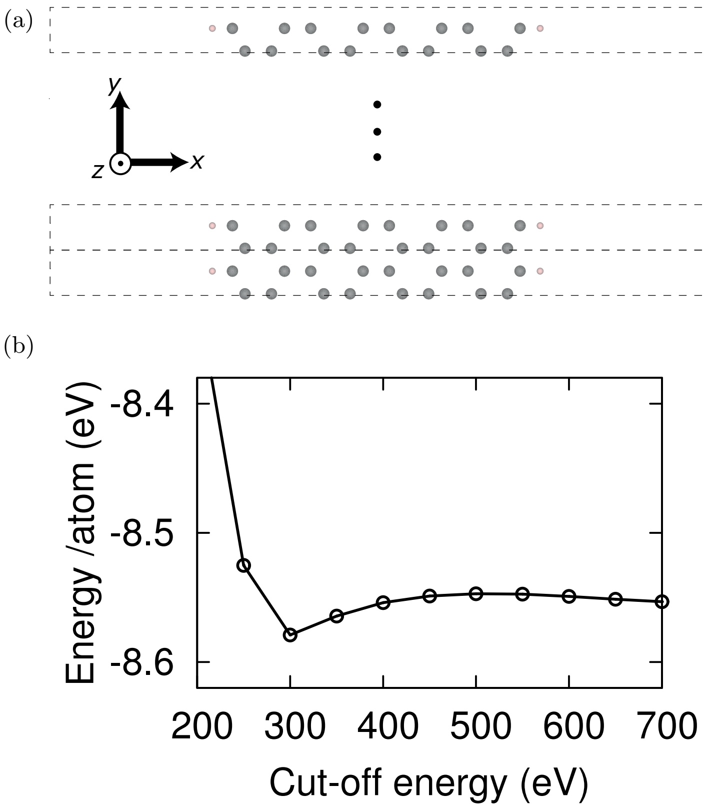

Figure 3-2: The primitive cell was prepared from the result of lattice parameters of graphene. (a) The 8-ZGNR composed of 16 C atoms and two H atoms in a unit cell with lattice constant of 2.462 Å in the y-axis. The dashed line represents the unit cell. (b) In order to verify the cutoff energy, the calculation was performed with the cutoff energy from 200 to 700 eV.

The projector augmented-wave (PAW) method is norm-conserving and ultra-soft pseudopotential.[114,115] The cutoff energy is chosen for our calculation from the result of geometry, which was given by the lattice parameter. With the ZGNR where the lengths of the C−C bonds were fixed at 1.422 Å for C−C but the bonds C−H were optimized, the energies per atom (E_{atom}) were converge to 8.553 eV at the 700 eV cutoff energy. And the accuracy reached when the cutoff energy was given by 400 eV, within 1 meV difference.

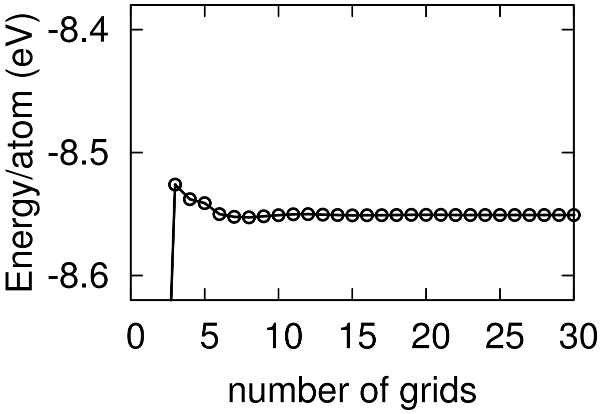

Figure 3-3: The 8-ZGNR with lattice constant of 2.462 Å in the y-axis was calculated with the 400 eV cutoff energy. By the Monkhorst-Pack method, from 1 to 30 k-points were used to integrate the Bloch states.

3.1.3 k-points sampling

The Monkhorst-Pack method was used to sample the k-points. The ZGNR in a unit cell is periodic along only one axis. For two other axes, the ZGNR is isolated from the neighbors by vacuum. Thus, though multiple k-points were used in the periodic axis, only one k-point was sampled during the calculations for the non-periodic axes.

More dense grids for sampling produce a more accurate result of the integral, as mentioned in 2.4.2. However, we should compromise between computational accuracy and efficiency. As the number of grid increases the results converge to 8.552 eV with 30 grids, as shown in Figure. 3-3. It was found that the E_{atom} is stable over $1 \times 6 \times 1$, within the range from 8.550 to 8.553 eV, in this model. For the reason, more k-points are unnecessarily required.

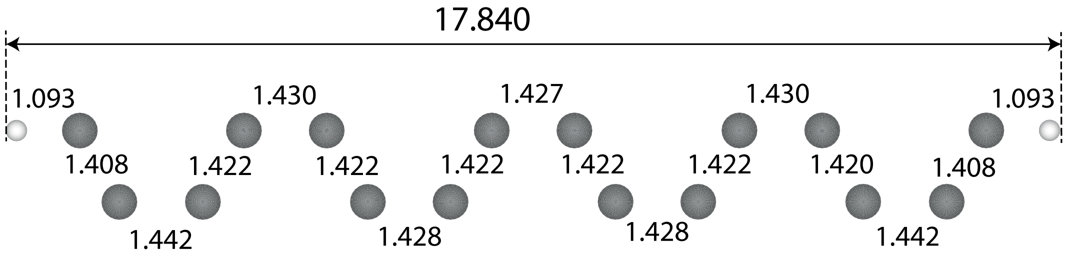

Figure 3-4: The geometry of a row of 8-ZGNR was optimized in the periodic boundary condition. The lattice constant was 2.462 Å along the y-axis, and the distances are written in Å.

Geometry of pristine GNR

The Figure 3-4 is the relaxed geometry of 8-ZGNR until the forces acting on each atom was less 0.01 eV/Å. The results of preliminary calculations were adopted to specify the computational details for relaxing ions. Computational accuracy is usually loosen to compromise the computational efficiency to some extent at which E_{atom} is different from the converged E_{atom} by less 10 meV. The planewaves were used with the energy cutoff of 400 eV, by means of DFT-PBE. And $1 \times 11 \times 1$ k-points were integrated by the Monkhorst-Pack method. There were eight C atoms and two H atoms in a supercell, which represented 8-ZGNR. This primitive row constitutes of ZGNRs. The diagonal C−C bond length was 1.422 Å, which was similar to the bond length of graphene, but the C−C at edge was shorten as 1.408 Å. The C−C bonds which are parallel with the x-axis were longer than the diagonal bond lengths, in contrast to the diagonal bonds, the outmost of C−C parallel with x-axis is longest as 1.442 Å. Because of the H atom by which the nanoribbon is terminated, the geometric feature is different passing through the width. And this implies that the state of C atom, including the state of p_z orbital, is not identical in GNRs from the middle to the edge. At edges, the C atoms are discerned from the others.

3.2 Electronic and magnetic structure

There are two types of graphene edge. These edges have a difference in their orientation in graphene's hexagonal lattice. Due to the difference, the π-electronic structure is induced by the two types of graphene edges.[4,116] In particular, a zigzag edge exhibits localized states, where an armchair edge dose not exhibit such localized states. The edge states may be a source of the peculiar magnetic and transport properties of nanoscale graphene.[14,29–31]

3.2.1 Supercell and band structure

If there is a molecule at every other row, the 16 C atoms are no longer enough for 8-ZGNR, as the supercell is shown in Figure 3-5(a). As a unit cell consists of 32 C atoms, the molecule should be arranged occupying a primitive row and the other row should be vacant without any molecules. So, we can avoid the unlikely periodicity in which molecules are packed in too short distance, in a finite size. The unit cell including a GNR which consists of multiple row is a supercell. Figure 3-5(a) is the unit cell, which is the identical in Figure 3-4. This involves only one primitive row of GNR structure. And the supercells in Figure 3-5 (b), (c), and (d) are composed of double, triple, and quadruple primitive rows. The number of atom and the lattice parameters are as two, three, and four times as those of the unit cell of a single row. And the supercells are denoted from the single primitive supercell as 8-ZGNR-1P, 8-ZGNR-2P, 8-ZGNR-3P, and 8-ZGNR-4P, respectively.

Although the number of atom in the cell is different, the supercells are physically same states as they all are the pristine 8-ZGNR. The calculation results of DOS (density of states) appear that the band gaps are 0.49 eV constantly. The band energies of the α-spin state electrons and the β-spin state electrons are the plot in Figure 3-6. The dispersion relation is the energy of the valence bands with respect to the k vectors of the corresponding supercells of 8-ZGNR-1P, 8-ZGNR-2P, 8-ZGNR-3P, and 8-ZGNR-4P. For each supercell, the lines overlapped with the band of each other state for corresponding energy in the whole k space. The only difference is the symmetry of bands in reciprocal space. Because the supercell comprise a different numbers of repeated C atoms, the symmetry of valence bands are different in the first Brillouin zone.

The primitive vectors in reciprocal space are defined by the relation

$$\mathbf{b}_2 = 2\pi \frac{\mathbf{a}_3 \times \mathbf{a}_1}{\mathbf{a}_2 \cdot (\mathbf{a}_3 \times \mathbf{a}_1)} \tag{3.4}$$

and our unit cells are orthorhombic (rectangular cuboid), thus

$$\mathbf{b}_2 = 2\pi \frac{\mathbf{a}_2}{|\mathbf{a}_2|^2} \tag{3.5}$$

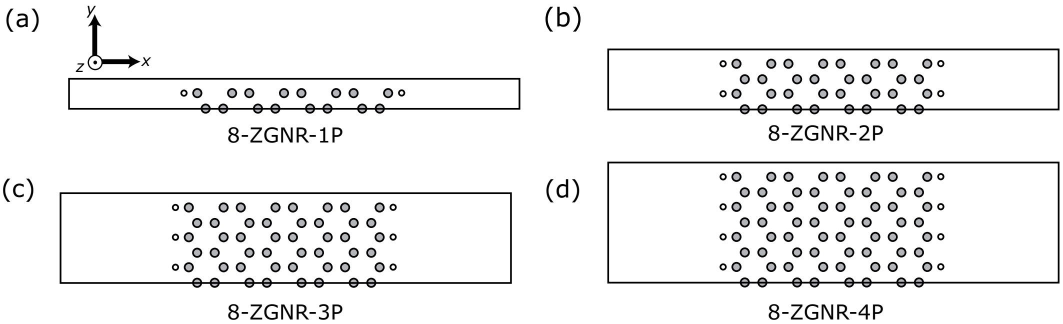

Figure 3-5: Supercells consisted of multiple primitive rows. The supercell is the area enclosed by solid lines. The gray circles are C atoms and the empty circles are H atoms. The 8-ZGNR composed of (a) 16 C + 2H, (b) 32 C + 4 H, (c) 48 C + 6 H, and (d) 64 C + 8 H in a supercell. Depending on the number of C atom in a supercell, the lattice constant was 2.462, 4.924, 7.836, 9.848 Å, respectively, along the y-axis.

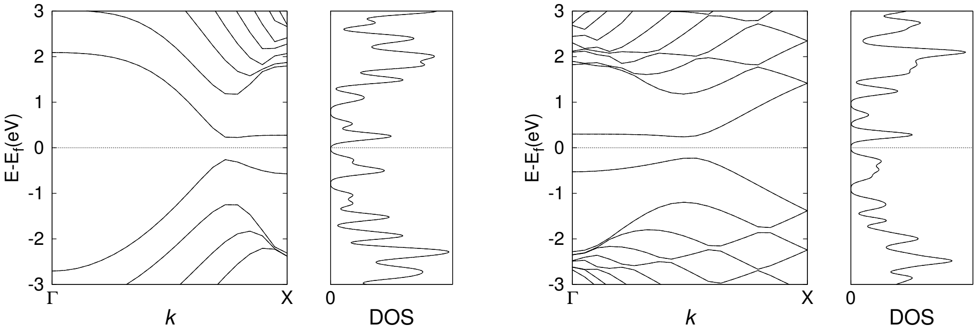

(a) 8-ZGNR-1P (b) 8-ZGNR-2P

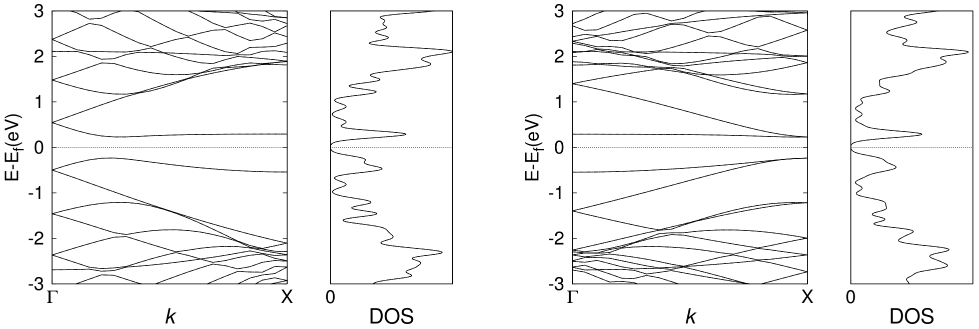

(c) 8-ZGNR-3P (d) 8-ZGNR-4P

Figure 3-6: The plots are the band energy with respect to k in the first Brillouin zone (left) and the DOS (right) corresponding to the supercells of 8-ZGNR, where $E_{\mathbf{f}}$ denotes the Fermi energy. The supercells comprised (a) only the primitive cell, (b) two primitive cells, (c) three primitive cells, and (d) four primitive cells. The band in the α-spin state (solid line) was degenerated with the band in the β-spin state (dashed line).

As the lattice parameter is larger in real space, the lattice vector is shorter in reciprocal space. In the comparisons of the band structures in Figure 3-6, the larger supercells have the energy change slower with respect to the vector k. In other words, we can sample less k-points for larger supercells.

We affirmed the appropriate number of the Monkhorst-Pack grid for the supercells, at which the Bloch states were integrated. The Figure 3-7 is the energy with respect to the number of the k space grid, depending on the size of supercells. The size

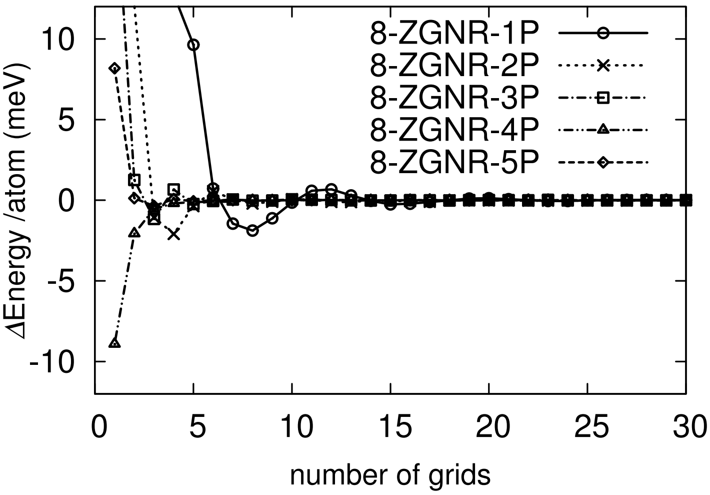

Figure 3-7: The energy is different depending on the number of grids to be sampled in k-space. The reference energy is the total energy calculated by 30 Monkhorst-Pack grids for corresponding supercells. The supercells consisted of multiple primitive rows. As the supercell is larger in real space, the energies is converged with less grids. The circle, cross mark, square, triangle, diamond are for the 8-ZGNR-1P, 8-ZGNR-2P, 8-ZGNR-3P, 8-ZGNR-4P, and 8-ZGNR-5P supercell, respectively.

of supercells led the energies to be quickly converged. The supercell in which two primitive rows are put together was converged with four k-point grids, within 3 meV difference.

As usual, the number of grid to integrate Bloch states is chosen with the accuracy within 10 meV error per atom. The supercell which was made up of over four primitive cells requires only one k-point to be sampled to reach the energy accuracy within the criterion. It should be noted that in periodic boundary conditions we can use one k-point for isolated states which are distant from the neighbors in real space. If a molecule absorbs at a primitive row and the molecule is distant from the neighboring molecules in periodic boundary conditions, the overlap between the states induced by the molecule can be negligible. Thus, we can compute the isolated adsorption

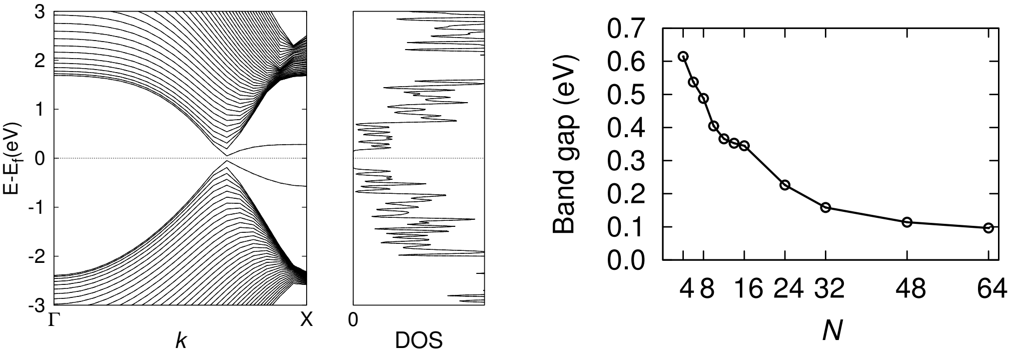

(a) 64-ZGNR

(b) Band gaps

Figure 3-8: (a) For 64-ZGNR, the band structure and DOS are plotted with respect to k space. During the calculation, spin-polarized wavefunctions were used. (b) The band gap is dependent on the width. The N-ZGNR have the width N.

which occurs locally on an infinitely periodic system by the periodicity with more than four primitive rows.

3.2.2 Band gaps related with the width of ZGNR

Not fragmented zigzag nanoribbons which are yet a part of a graphene sheet have the degenerate edge states at $k = \pi/\mathbf{a}_2$ (at the K point, $\mathbf{k} = \frac{2}{3}\mathbf{b}_1 + \frac{1}{3}\mathbf{b}_2$ for graphene). The band gap of the zigzag ribbons is zero and the system is semimetallic. However, the energy bands have a gap but for the K points, because the π and π^* configurations develop between two edges originating to each other by the angle of 30°. It was shown by Fujital et. al. by means of tight binding band calculations that from $k = \pi/\mathbf{a}_2$ to $k = \frac{2}{3}\pi\mathbf{a}_2$ the localized edge state penetrate the inner sites.[4] Hence, the band gap is open as soon as the ZGNRs are fragmented and terminated by H atoms, due to the absence of reciprocal vector crossing the edges.

The feature of graphene can be recovered approximately when a ZGNR is much wider. As the width is wider, the gap is narrower.[33,117] And the gap will be eventually zero at infinite width as the gap is zero in graphene. The Figure 3-8 is the results of our calculations. The band gaps reduced from 0.61 to 0.10 eV while the width was wider from 4- to 64-ZGNR. Based on the method of the DFT calculation, we could observe that the gap was narrowed inversely with the width of ZGNR.

As we turn into the quantities, for the 8-ZGNR, the band gap was 0.49 eV from our results. This is similar to the result of BYLP functional.[118] And their B3LYP result was 1.34 eV. The method of the hybrid functional accounts for nonlocal exchange interaction and it resulted in interactions from one edge to the other edge. In comparisons, the gap was 0.31 eV by LDA functional.[33,118,119] The gradient corrections attributed to the difference between LDA and GGA.

3.2.3 Magnetism of pristine GNR

In ZGNRs, the edge state is attributed to the repetition of a sublattice of graphene in a zigzag edge, meanwhile both sublattices are repeated in armchair edge. According to the broken symmetry in ZGNRs, the spin-polarized electrons are distributed spatially for the nonbonding π-states. And the feature was observed by experiments.[120]

The electrons are spin polarized at edges. And the unpaired electrons contribute the ferromagnetic state along an edge, we compared two magnetic structure: at both edges the same spin-state is localized (ferromagnetic), and at each edge the different spin-state electrons are localized along the corresponding edge (antiferromagnetic). Figure 3-9 is the isosurface of the charge density difference density ($\rho_\alpha(\mathbf{r}) - \rho_\beta(\mathbf{r})$). Ferromagnetic (FM) structures appeared that the α-spin state electrons were localized at both edges as in Figure 3-9(a), in the meantime, antiferromagnetic (AF) structures come out the configure where the α-spin state electrons were at an edge (red) and the β-state electrons were at the other edge (blue). In the

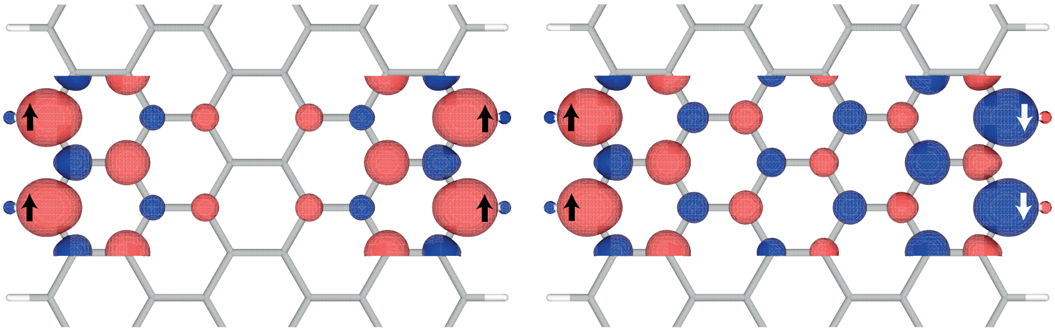

(a) Ferromagnetic (b) Antiferromagnetic

Figure 3-9: For 6-ZGNR, the charge density difference is depicted for the α-spin electrons (red) and the β-spin electrons (blue). The zigzag edges have ferromagnetic structure along an edge. There are two states: (a) the same spin states are localized in both edges as ferromagnetic and (b) the different spin states are localized in each edge as antiferromagnetic.

antiferromagnetic configuration, the valence bands of 8-ZGNR is below the Fermi level and the conduction band is above the Fermi level for both spin states. In the ferromagnetic configuration, the highest valence band corresponding to each α- and β-spin state is now partly upper than the Fermi level and partly lower than the Fermi level.

Table 3.1: The magnetic moments with H terminations for N-ZGNRs with various widths for AF and FM configurations.

	Antiferromagnetic		Ferromagnetic	
Width (N)	Total magnetic moment(μ_B)	Magnetic moment (μ_B/edge atom)	Total magnetic moment (μ_B)	Magnetic moment (μ_B/edge atom)
4	0.0	0.135	0.308	0.104
5	0.0	0.143	0.308	0.105
6	0.0	0.148	0.615	0.153
7	0.0	0.151	0.615	0.153
8	0.0	0.153	0.615	0.153
16	0.0	0.153	0.615	0.153
64	0.0	0.153	0.615	0.153

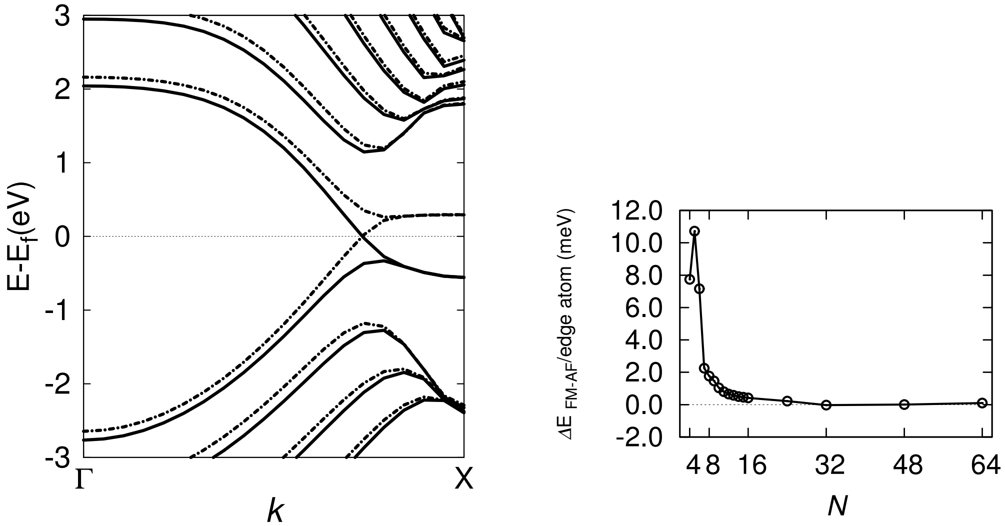

(a) 8-ZGNR in FM (b) $\Delta E_{\mathrm{FM-AF}}$

Figure 3-10: (a) The band structures of 8-ZGNR in FM. The solid line is the band for the α-spin state and the dot-dash line is the band for the β-spin state. (b) The relative energy ($E_{\mathrm{FM}} - E_{\mathrm{AF}}$) is for an edge atom. N is the width of N-ZGNRs.

The antiferromagnetic ZGNR have the sublattices of which p_z orbitals are antiferromagnetic through the width, in which the electrons are localized in every C atoms with surplus electron densities in alternate spin states. Subsequently, the total energy is lower than the ferromagnetic ZGNR in which two spin states are degenerate at the middle site. Their relative energies are plotted in Figure 3-10(b). The energy differences were dependent on the width of ZGNRs. As the band gap was smaller with the increasing width, the energy difference between ferromagnetic and antiferromagnetic configuration also was close to zero with larger width. The effect of localized edge states decayed trough the inner site of ribbons. As the magnetic moments are given in Table 3.1, the magnetic moment of the edge atom increased as the width is wider from 4- to 7-ZGNR. Nonetheless, the magnetic moment of the edge atom is not changed significantly by the width from 8- to 64-ZGNR for both magnetic configurations.

3.3 DFT-PBE calculations of GNRs

We studied pristine ZGNRs in DFT method with the PBE functional. From the perfect hexagonal graphene, we were able to determine the lattice constant of GNRs. The model system which is referred to as ZGNRs were repeated in periodic boundary conditions and separated with vacuum from the neighbors in other supercells. As the energy with more mesh grids results in to be more accurate by the integral of Bloch states, we were able to have reasonable accuracy over six k-points Monkhorst-Pack girds with less computational resources.

The ban gap that we obtained was smaller for pristine GNRs, compared with GW method, or hybrid functionals. Because only the information of local charge density and gradient are involved in PBE functional, it fails to correct the long-range exchange and correlation between electrons and between an electron and a hole. However, our results of the tendency of the electronic and magnetic structure were consistent with other theoretical and experimental researches for pristine GNRs.

With this method, the calculations have been performed for the GNRs of which band structures are induced by small molecules and functional groups. The state localized at edges contributes to highest valence bands. And the state at an edge is separated from the localized state at another edge across the width. Thus, if the edge state is perturbed by introducing molecules and functional groups we may tune the band structure of ZGNRs. We would discuss the study on such systems in the following chapters 4 and 5. The method would support the validation of the results of the model system for functional GNRs and be compared with the properties of doped GNRs in comparisons.

Chapter 4

Tuning of the Band Structures of GNRs by and Electric Field and adsorption of molecules*

---

*The contents of this chapter are based on the published article "H. Park, J. Y. Lee, and S. Shin *J. phys. chem. C* **2012**, *116*, 20054" [121]

4.1 Introduction

ZGNRs have recently been shown by spin polarized calculations to have an antiferromagnetic spin state with paramagnetic spin ordering at each edge with opposite spins for the two edges.[122] By applying an external magnetic field, the antiferromagnetic state can be converted into a ferromagnetic state with parallel (ferromagnetic) edge states, which could be utilized as a spin-valve device.[123,124] Furthermore, the edge spin state could be controlled by an external electric field and be turned into half-metallic. Hence, ZGNRs are a potential candidate for spintronic device applications. As a derivative, zigzag silicon carbon nanoribbons (ZSiCNRs) are also known to yield similar electronic and magnetic properties. For a narrow ZSiCNR, it has a small band gap for one spin and can be considered as a half-semimetal with antiparallel spin ordering similar to a ZGNR.[125] A ZSiCNR showed similar spin behavior to a ZGNR under electron/hole doping and chemical doping[126] as well as an external electric field.[127]

Graphene is composed of sp^2 carbon atoms arranged in a two-dimensional honeycomb lattice. The p orbitals corresponding to π electrons are perpendicular to the graphene plane. These orbitals comprise the highest valence band and the lowest conduction band and therefore, reflect the properties of graphene. In particular, in ZGNRs, the spin densities of the highest valence and the lowest conduction bands near the Fermi level are localized at edges.[4,122,128–131] Thus, the spin state at the edges of a GNR should be significantly affected by chemical or physical modification near the edges. The fabrication of GNRs with uniformly functionalized edges is very challenging. Recently, precise fabrication of GNRs with the edges passivated by H atoms was realized using surface-assisted coupling of molecular precursors.[7] Accordingly, by utilizing the proper precursors, chemically modified GNRs may be achieved. Therefore, it is very intriguing to investigate the electronic and spin properties of GNRs under the influence of chemical modification. Such perturbation at the C atoms of ZGNRs can lead to shifts of the energy level in the effective potential for π or π^* orbitals by chemical decorations of functional group with covalent bond[8,130,132–140] and by dipole moments of absorbed polymers with non-covalent interactions.[141]

Pyridine is a typical Lewis base and may influence N-doping when it is adsorbed on a GNR. In this work, the influence of chemical and physical modification by pyridine on the band structures and DOSs and hence, the metallicity of ZGNR was investigated without and with an external electric field. Further modifications of ZGNR by the addition of a Lewis acid such as BF_3 are also investigated. In this work, we considered two cases, covalent interaction and noncovalent interaction. We replaced a pyridine molecule with a hydrogen atom of hydrogen-passivated ZGNRs where nitrogen and carbon atoms form a bond and we put a nitrogen atom in the plane of ZGNRs. Plus, we added pyridine at edge into ZGNR without losing hydrogen atoms of the pristine ZGNR. And secondly, we set pyridine periodically on the various locations of ZGNRs to figure out noncovalent interactions.

4.2 Computational Details

To investigate the effects of chemical and physical adsorptions of pyridine on ZGNRs, we carried out the calculations by using Vienna *ab initio* simulation package (VASP) code[96–98], employing the projected augmented wave (PAW) potentials[114,115]. And the exchange-correlation functional with the spin polarized generalized gradient approximation (GGA) in the Perdew–Burke–Ernzerhof (PBE) form[94,142] was employed.

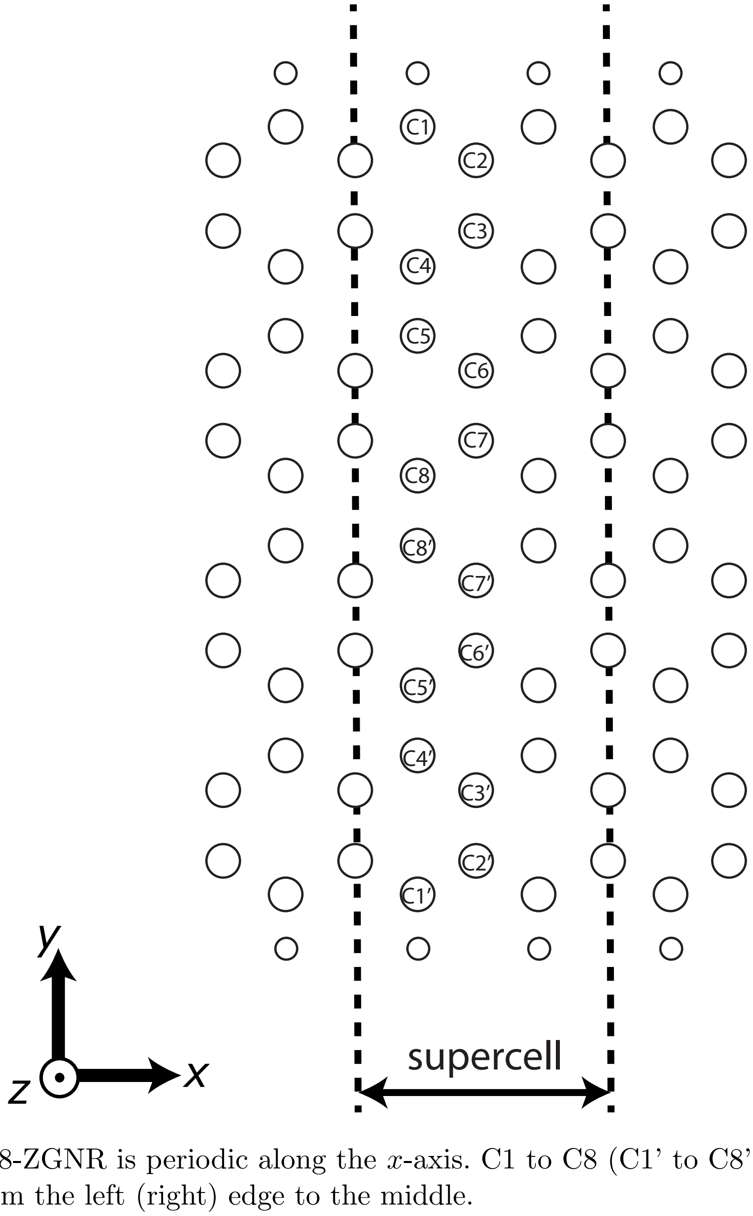
C1
C2
C3
C4
C5
C6
C7
C8
C8'
C7'
C6'
C5'
C4'
C3'
C2'
C1'
y
x
z
supercell

Figure 4-1: 8-ZGNR is periodic along the x-axis. C1 to C8 (C1' to C8') denote the C atoms from the left (right) edge to the middle.

In our model, 8-ZGNR is flat in the x-y plane with 8-zigzag chains along the x direction. The edges of the ZGNRs were passivated by H atoms. A periodic

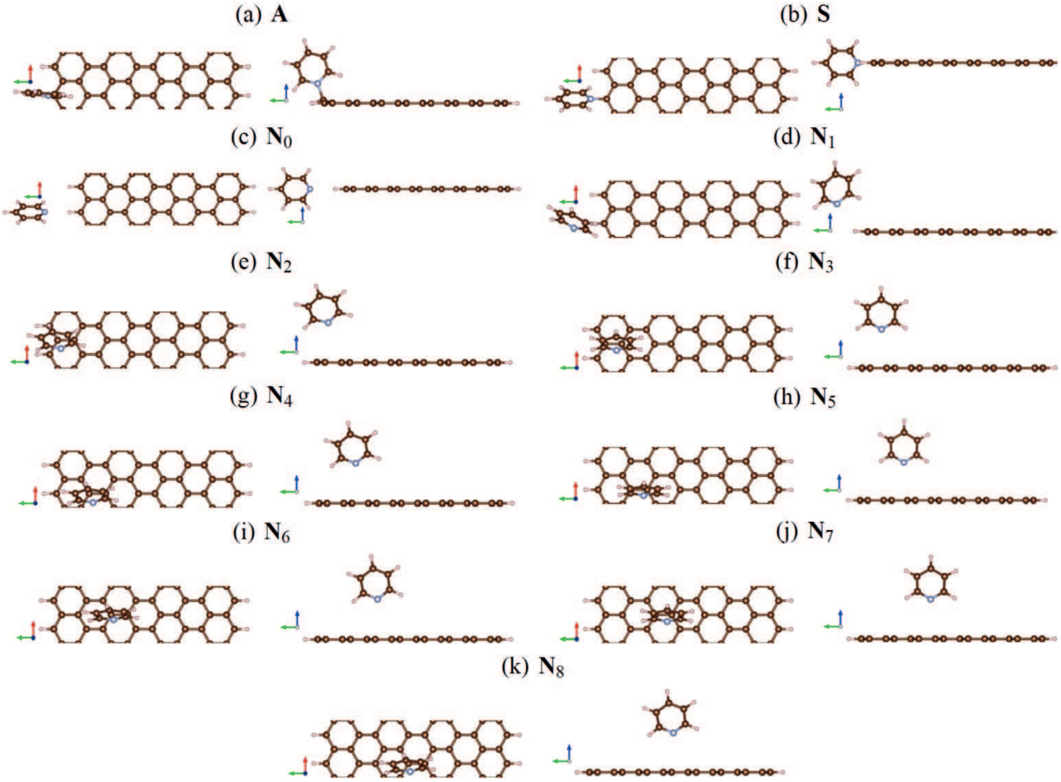
(a) **A**
(b) **S**
(c) $\mathbf{N}_0$
(d) $\mathbf{N}_1$
(e) $\mathbf{N}_2$
(f) $\mathbf{N}_3$
(g) $\mathbf{N}_4$
(h) $\mathbf{N}_5$
(i) $\mathbf{N}_6$
(j) $\mathbf{N}_7$
(k) $\mathbf{N}_8$

Figure 4-2: Optimized geometries of different bindings of pyridine with the ZGNRs fabricated in this work. Atom colors: carbon (brown); hydrogen (white); nitrogen (light blue).

boundary condition was used to consider ZGNRs with an infinite length (Figure 4-1). We adapted a supercell geometry where the lengths of the vacuum region along the non-periodic directions along the y and z-axis were 35 Å and 25 Å, respectively, which include enough vacuum space to avoid interactions with adjacent neighbors. We verified the appropriate lattice constant by which the total energy was the lowest for graphene. The lattice constant of 4.92 Å along the x-axis, obtained by verification of the lattice constant and subsequent relaxation of ions, resulted in a C−C bond length of 1.42 Å with sp^2 hybridizations. For pyridine adsorption, we considered several systems: addition on an edge C atom (denoted as **A**), edge H atom substitution by pyridine (denoted as **S**), and non-covalent physisorptions (denoted as $\mathbf{N}_0$, $\mathbf{N}_1$, ..., $\mathbf{N}_8$). For $\mathbf{N}_0$, the nitrogen atom of pyridine faces the hydrogen atom of the ZGNR along the plane. For $\mathbf{N}_1$, ..., $\mathbf{N}_8$, the nitrogen atom of pyridine was located on the C1, ..., C8 of the ZGNR, respectively (Figure 4-2).

The geometries were optimized until the Hellmann-Feynman forces were less than 0.01 eV/Å (= 1.9410^{-4} Hartree/bohr). The convergence of the energy was 10^{-5} eV (= 3.6810^{-7} Hartree). We used 400 eV as the planewave cutoff energy and $10 \times 1 \times 1$ k-point sampling in the Brillouin zone integration. Even in the case of pyridine adsorption on the ZGNR, the lengths of the vacuum along the y- and z-axis were over 17 Å and 20 Å, respectively, which exclude possible interactions between nanoribbons within the adapted supercell. In addition, we obtained the energies and electron densities using a planewave cutoff of 400 eV and a k-mesh of $25 \times 1 \times 1$ with more k-points to ensure accuracy of the self-consistent calculation. The formation energy of pyridine on the graphene sheet was quantified as follows,

$$E_{\text{form}} = E\left(\text{ZGNR} + \sum_i n_i e_i\right) - E(\text{ZGNR}) - \sum_i n_i E(e_i) \tag{4.1}$$

where $E\left(\text{ZGNR} + \sum_i n_i e_i\right)$ is the total energy of the system with n_i groups and e_i (−H or pyridine) bonds on the pristine graphene nanoribbon, $E(\text{ZGNR})$ is the energy of the pristine ZGNR which was fully relaxed, and $E(e_i)$ is the total energy of the group e_i. The reference energy value for the hydrogen atom was evaluated in an isolated H_2 molecule as a spin polarized state.

4.3 Results and discussion

4.3.1 Covalent and noncovalent interactions

Here, we studied a hexagonal network of H-terminated 8-zigzag graphene nanoribbons (8-ZGNRs). On the basis of the results obtained for this 8-ZGNR, we compared the electronic structures of 8-ZGNRs perturbed by pyridine. As shown in Figure 4-1, we considered a ZGNR with a unit cell of 32 C atoms and four H atoms. It was found that when pyridine was located at the outermost C atom (C1) of the ZGNR, forming a 1.54 Å covalent N−C bond (denoted as **A**), the C1 atom of the ZGNR puckered outward from the plane of the ZGNR by 0.26 Å along the z-axis. Although we were able to observe this geometry for the covalent bond with the C1 atom, we were not able to obtain the geometries including covalent bonds for C2 through C8. It should be noted that the process of forming **A** is endothermic (energetically unfavorable) with an energy increment of 0.94 eV because of the loss of aromaticity and the resonance energy which exceeds the energy gain by N−C bond formation. For **S**, the pyridine molecule replaces the hydrogen atom on only one edge in the unit cell, as seen in Figure 4-2. This structure has a N−C bond length of 1.43 Å. The formation of **S** is endothermic by 1.02 eV; therefore, **S** is much more unfavorable than **A**.

Noncovalent interactions between pyridine and the ZGNR were also considered. We fully relaxed the ions after we put pyridine on C1 through C8. To attach the pyridine, we made the lone pair of the N atom point toward the chosen atom on the ZGNR. These structures are denoted as $\mathbf{N}_1$ to $\mathbf{N}_8$, respectively, depending on the chosen C atom, as seen in Figure 4-1. In addition, we also investigated a structure in which the pyridine interacts with the H atom of the ZGNR; this structure is denoted

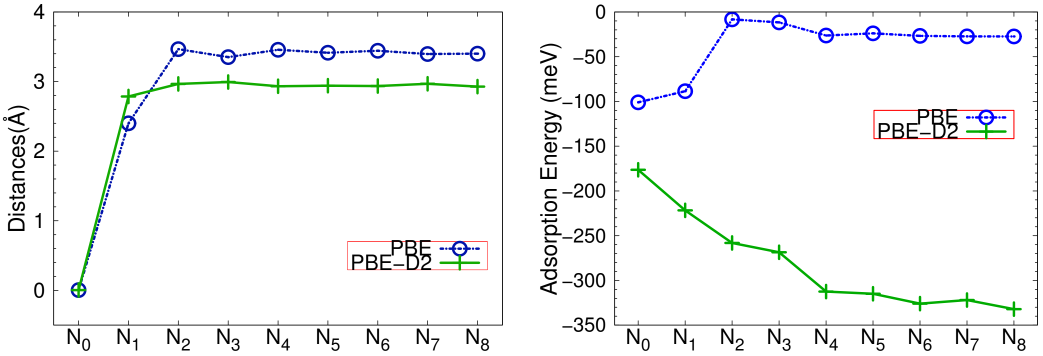

(a) (b)

Figure 4-3: Distances and adsorption energies were obtained with or without accounting for dispersion effects. (a) The distance between pyridine and graphene is defined as a distance between N atom of pyridine and the graphene surface. (b) Adsorption energies with and without the consideration of dispersive interactions are green-cross points and blue-empty-circle points, respectively.

as $\mathbf{N}_0$. The initial distance between the N of the pyridine and each C ($d_{\text{N-C}}$) of the ZGNR was 1.8 Å. After the geometry optimization with the PBE functional, pyridine molecules moved away from the ZGNRs, resulting in a distance ($d_{\text{N-C}}$) ranging from 3.35 to 3.46 Å. The formation energies of $\mathbf{N}_0$ and $\mathbf{N}_1$ were calculated to be -0.10 and -0.09 eV, respectively, which are much smaller than those of **A** and **S**.

For the other interacting systems, $\mathbf{N}_2$-$\mathbf{N}_8$, the formation energies are shallow, ranging from -0.01 to -0.03 eV. On the other hand, after the geometry optimization with the PBE-D2 method, the pyridine molecules moved closer to the ZGNRs. The interatomic distance ($d_{\text{N-C}}$) is shorter by about 0.5 Å than that resulting from the PBE approach, as shown in Figure 4-3(a). As a result, the adsorption energies per unit cell were calculated to be about 70 and 300 meV larger than those obtained from the PBE method for $\mathbf{N}_0$ and $\mathbf{N}_8$, respectively. The adsorption energy and the distance of pyridine-ZGNR for $\mathbf{N}_8$ obtained by the PBE-D2 method are consistent with previous results for pyridine-graphene.[143] Moreover, as shown in Figure 4-3(b),

(a) pristine (b) **A** (c) **S**

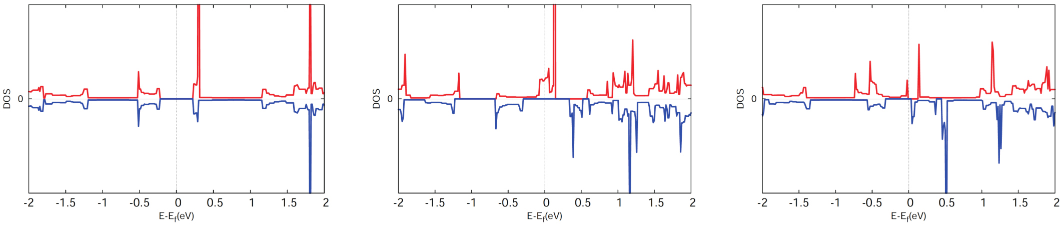

(d) $\mathbf{N}_0$ (e) $\mathbf{N}_1$ (f) $\mathbf{N}_2$

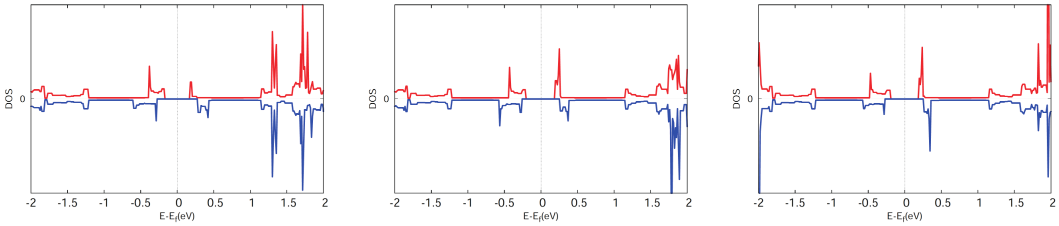

(g) $\mathbf{N}_3$ (h) $\mathbf{N}_4$ (i) $\mathbf{N}_5$

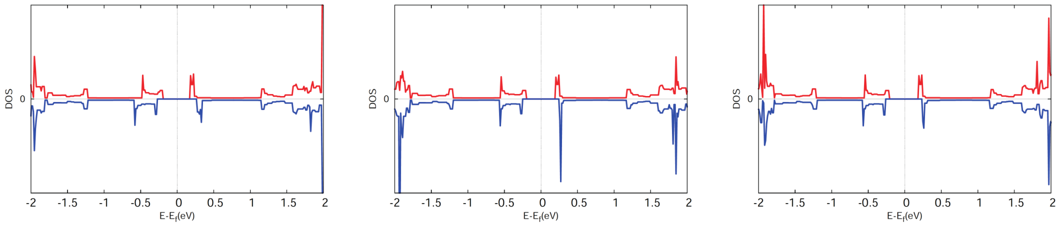

(j) $\mathbf{N}_6$ (k) $\mathbf{N}_7$ (l) $\mathbf{N}_8$

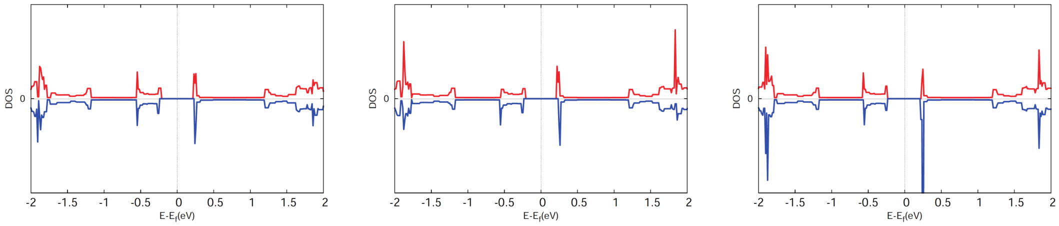

Figure 4-4: Density of state (DOS) with a (red) and b (blue) state: (a) pristine ZGNR (b) **A**, (c) **S**, (d)-(l) for from $\mathbf{N}_0$ to $\mathbf{N}_8$

$\mathbf{N}_0$, in which pyridine is out of the surface of the ZGNR, was found to be the most stable complex by the PBE approach, while $\mathbf{N}_8$, in which pyridine is on the middle of the ZGNR, was the most favorable complex in the PBE-D2 results. This implies that the dispersive interactions could be critical to study molecular adsorption on ZGNRs.

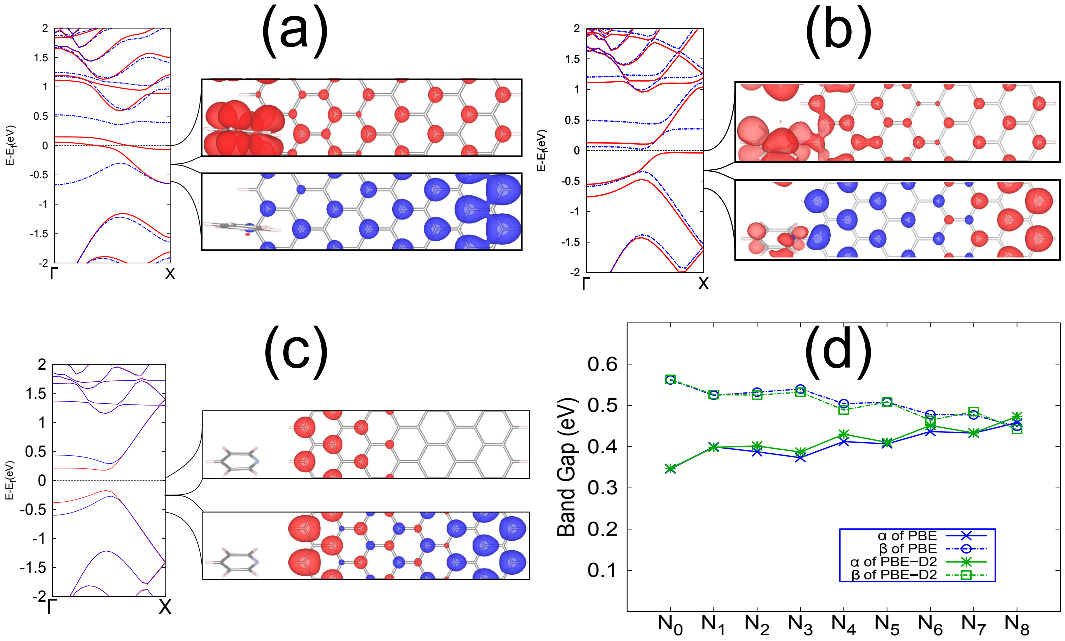

Figure 4-5: Band structures and spin densities of (a) **A**, (b) **S**, and (c) $\mathbf{N}_0$ and (d) band gaps of the α- and β-spin states. The spin densities correspond to the partial charge ranging from $E - E_\mathrm{f}$ values of -0.30 (-0.25) to 0 eV in the upper figures and from -0.60 (-0.5) to -0.30 (-0.25) eV in the lower figures for **A** and **S** ($\mathbf{N}_0$). The band gaps of α-spin (solid line) and β-spin (dotted line) was obtained by calculations using PBE (blue) and PBE-D2 (green).

$\mathbf{N}_8$ is more favorable than $\mathbf{N}_0$ and $\mathbf{N}_2$ by about 0.16 and 0.07 eV, respectively, in the absence of an electric field (Figure 4-3); however, $\mathbf{N}_8$ becomes more unstable upon the electric field along the y-axis, and finally, $\mathbf{N}_0$ and $\mathbf{N}_2$ are more stable than $\mathbf{N}_8$ when the electric field is applied by over 0.2 eV in either direction along the y-axis (Figure 4-4). It appears that the favorable site is dependent on the strength of the external electric field along the y-axis, and consequently the band gap could be manipulated.

Figure 4-5 shows the band structures and spin densities of **A**, **S**, and $\mathbf{N}_0$. As shown in Figure 4-5(a), both the valence and conduction bands of the α-spin cross the Fermi level, while those of the β-spin do not. Therefore, **A** is half-metallic and has a β-spin band gap of 0.65 eV. It is worth noting that modifying only one edge with pyridine resulted in this half-metallicity, which could also be realized using a strong electric field or carrier doping. The partial spin density $(\rho_{\uparrow}(\mathbf{r}) - \rho_{\downarrow}(\mathbf{r}))$ of the highest valence band reflects the influence of pyridine as well as that of the ZGNR edges. As seen in Figure 4-5(a), for **A**, the spin density of the valence band of the α-spin is mostly localized at the LUMO of pyridine, whereas that of the β-spin is localized at the opposite edge. The valence bands of the α-spin and β-spin meet each other at X. The α-spin electrons are localized at the LUMO of the pyridine because of the covalent bond between pyridine and the ZGNR. Because pyridine has two electrons (lone pair), one electron of the C atom in the ZGNR is transferred to the LUMO when a N$-$C bond is formed, and the sp^2 hybridization of C changes to sp^3 hybridization.

For **S**, it is also seen that electrons of the valence band of the α-spin are localized at the LUMO of pyridine. To make the supercell neutral, when a pyridine replaces a H atom in **S**, there should be an extra electron on pyridine. Thus, the LUMO of each pyridine may be occupied by one electron. The highest valence band below the Fermi level of the α-spin state approaches the Fermi level at X, while the lowest conduction band above the Fermi level of the β-spin state is lower than that of the α-spin state at all k-points. Thus, **S** is semiconducting with a small band gap. The band gap of the α-spin is 0.14 eV, and that of the β-spin is 0.36 eV. The partial spin density $(\rho_{\uparrow}(\mathbf{r}) - \rho_{\downarrow}(\mathbf{r}))$ of the valence bands of **S** is significantly different than that of **A**. As seen in Figure 4-5(b), the spin density of the valence bands shows that the α-spin is mostly localized at the LUMO of pyridine and at the opposite edge, whereas the β-spin is mostly localized only at the edge near the

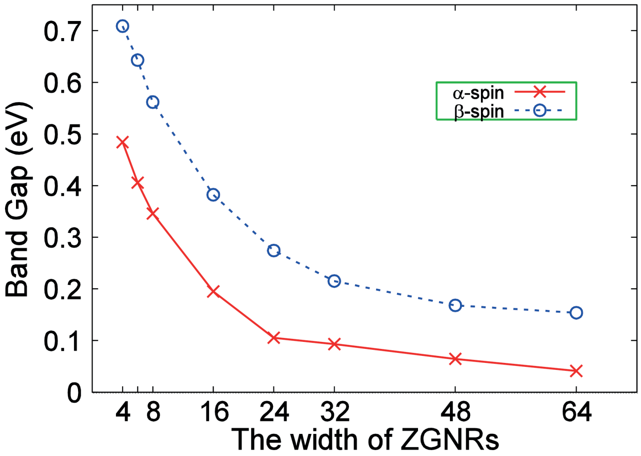

Figure 4-6: Band gaps of the α- and β-spin states for N-ZGNRs ($N = 4, 6, 8, \cdots, 64$).

pyridine. This is consistent with a previous report where the covalent N−C bond between the ZGNR and pyridine creates an antiaromatic radical in the LUMO of pyridine[144] and the N−C bond formation generates a pyridinium that is favored with a resonance-stabilized carbanion in which the charge is essentially neutralized by the delocalization of electrons onto the N of the pyridinium ring.[145] It should be noted that the formation of both **A** and **S** is energetically unfavorable though their metallicity is very interesting. Nevertheless, our study suggests that a proper and stable chemical modification could be used for band gap, hence metallicity, manipulation.

In the case of noncovalent bond formation ($\mathbf{N}_0$-$\mathbf{N}_8$), the change in the band structures from that of the ZGNR is much smaller than that obtained for **A** and **S** (Figure 4-5(c) and Figure 4-7). A remarkable difference was found between the α-spin and β-spin electrons below the Fermi energy level. The α-spin density of $\mathbf{N}_0$ is mostly localized only near the pyridine edge, while the energy of the valence band of the β-spin is lower than that of the pristine ZGNR. This implies that the local

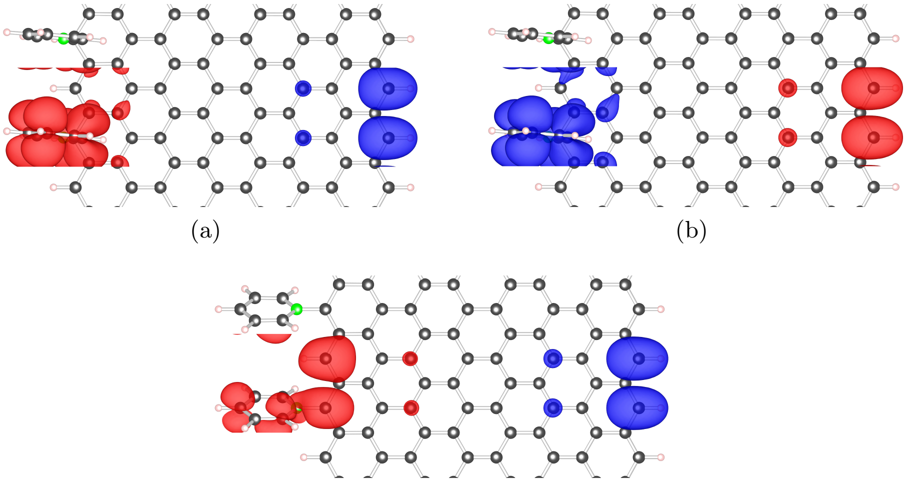

(a) (b)

(c)

Figure 4-7: Spin density of the highest valence bands: (a) the highest-1 bands of **A**, (b) the highest band of **A** (c) the highest bands of **S**.

electric field (due to electron redistribution) induced by pyridine decays slowly in space. We found that such an effect remains for larger ZGNRs up to 64-ZGNR, which has band gaps of the α- and β-spin states of 0.04 and 0.15 eV, respectively, as shown in Figure 4-6.

It would be interesting to investigate the change of band gap with different coverage ratios of adsorbing pyridine on the ZGNR. To investigate the effects of changes in coverage ratio, the band gaps of $\mathbf{N}_0$ were obtained for various lattice constants along the x-axis. The band gap difference between the α- and β- spin states of $\mathbf{N}_0$ decreases as the distance between the neighboring pyridine molecules increases (i.e., as the coverage decreases) as shown in Figure 4-8. With the configuration where the distance between absorbing pyridines is about 15 Å ($l = 6$), the band gaps of the α- and β-spin states are 0.42 and 0.50 eV, respectively. This tendency is also expected for ZGNRs with different widths. For the infinite dilute adsorption (zero

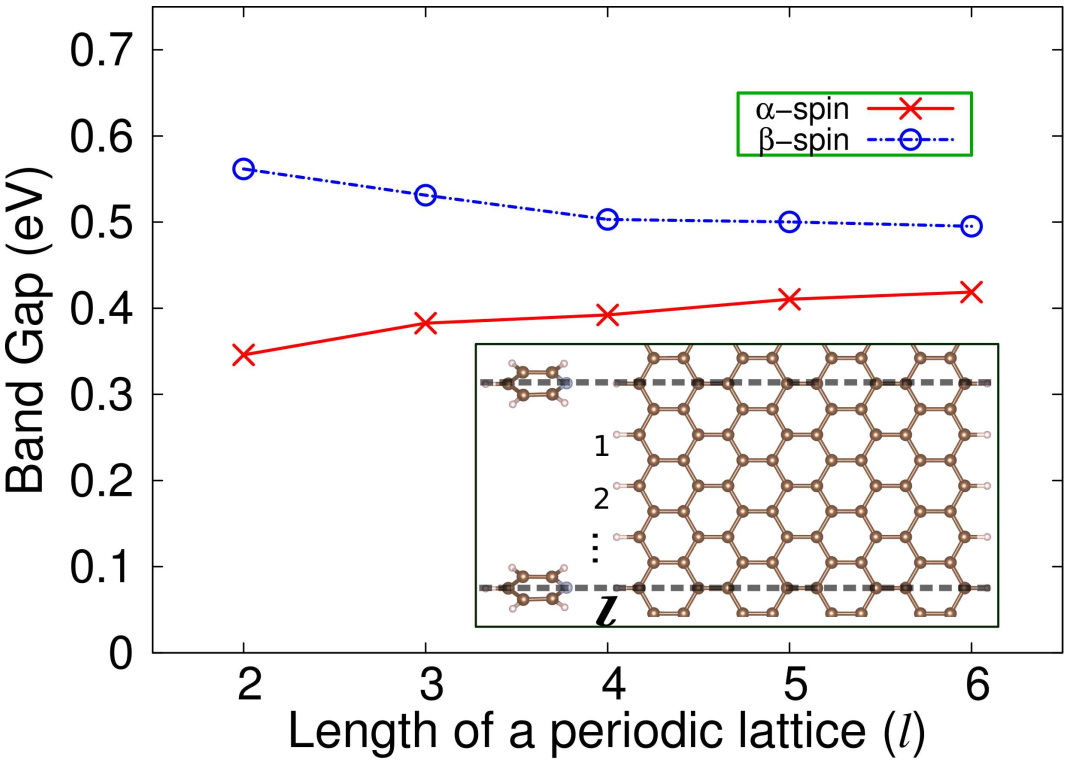

Figure 4-8: Band gaps of the α- and β-spin states for 8-ZGNRs depending on the distance between the neighboring pyridine molecules. For $l = 2$, the lattice constant is 4.92 Å along the periodic axis.

coverage limit) with a wide width, the band gaps of the α- and β-spin states should be equal to those of the pure ZGNR. As a matter of fact, the calculated system using a unit cell dimension of 4.92 Å would be very challenging to achieve experimentally. Nevertheless, the qualitative trends found in this study may be preserved in the presence of slight deviations from the simulated geometries.

These results are similar to the case of the larger band gap of the β-spin due to the decreased energy level of the valence band of the ZGNR under a weak external electric field.[119] Even though an external electric field is absent, in the case of noncovalent interactions, the energy level of the valence band of the α-spin is increased, and

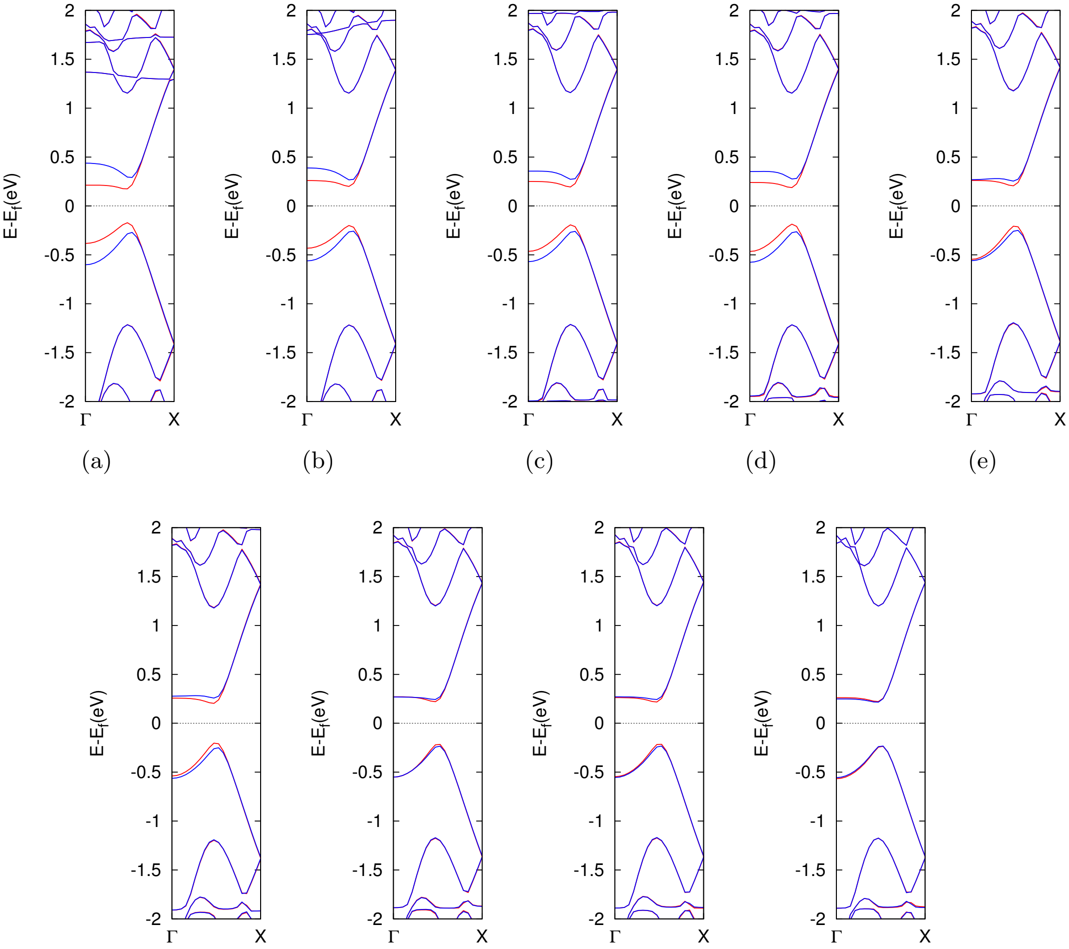

(a) (b) (c) (d) (e)

(f) (g) (h) (i)

Figure 4-9: Band structures with α (red) and β (blue) state: (a)-(i) for from $\mathbf{N}_0$ to $\mathbf{N}_8$.

that of the β-spin is decreased. For the conduction bands, the energy level of the α-spin state is lower than that of pristine ZGNRs, while that of the β-spin state is higher. The band gap difference decreases as the pyridine approaches the middle of the ZGNR along the y-axis. As seen in Figure 4-9, consequently, the band structure of $\mathbf{N}_8$ is almost equivalent to that of the pristine ZGNR. It was found that, in spite of the difference of the geometries obtained by the PBE and PBE-D2 methods, the band gap variation is less than 180 meV for the physisorbed systems ($\mathbf{N}_0$-$\mathbf{N}_8$), as shown in Figure 4-5(d). Even though the dispersive interaction should be included to determine the correct geometry, the results for the band gaps obtained in the calculations using PBE and PBE-D2 show small differences. It should be noted that the apparent insensitivity of band gap calculations to the inclusion of dispersion interaction may be related with the limitations of Kohn-Sham DFT, which does not take into account the long-range polarization effects.[146,147] The effects of long-range interaction on band gaps can be treated more accurately by advanced many-body perturbation theories such as GW approximation.[147–149] In the present study, our main focus is the qualitative trend of band gaps, which can be described reasonably well with the DFT calculations including dispersion effects.

Certain changes in the highest valence band and the lowest conduction band of the α- and β-spins were obtained only for $\mathbf{N}_0$-$\mathbf{N}_7$, and these changes became smaller from $\mathbf{N}_0$ to $\mathbf{N}_1$ to $\mathbf{N}_2$, ..., to $\mathbf{N}_7$; i.e., the change became smaller as the pyridine was adsorbed on a more central carbon atom along the y-axis of the ZGNR. As noted in Figure 4-5(d), the band gap of the α-spin decreased, while that of the β-spin increased compared with the pristine ZGNR when pyridine was adsorbed on carbon atoms of the ZGNR closer to the edge. The band gaps of the α-spin of $\mathbf{N}_0$ and $\mathbf{N}_2$ were reduced to 0.35 and 0.39 eV, while the band gaps of the β-spin were

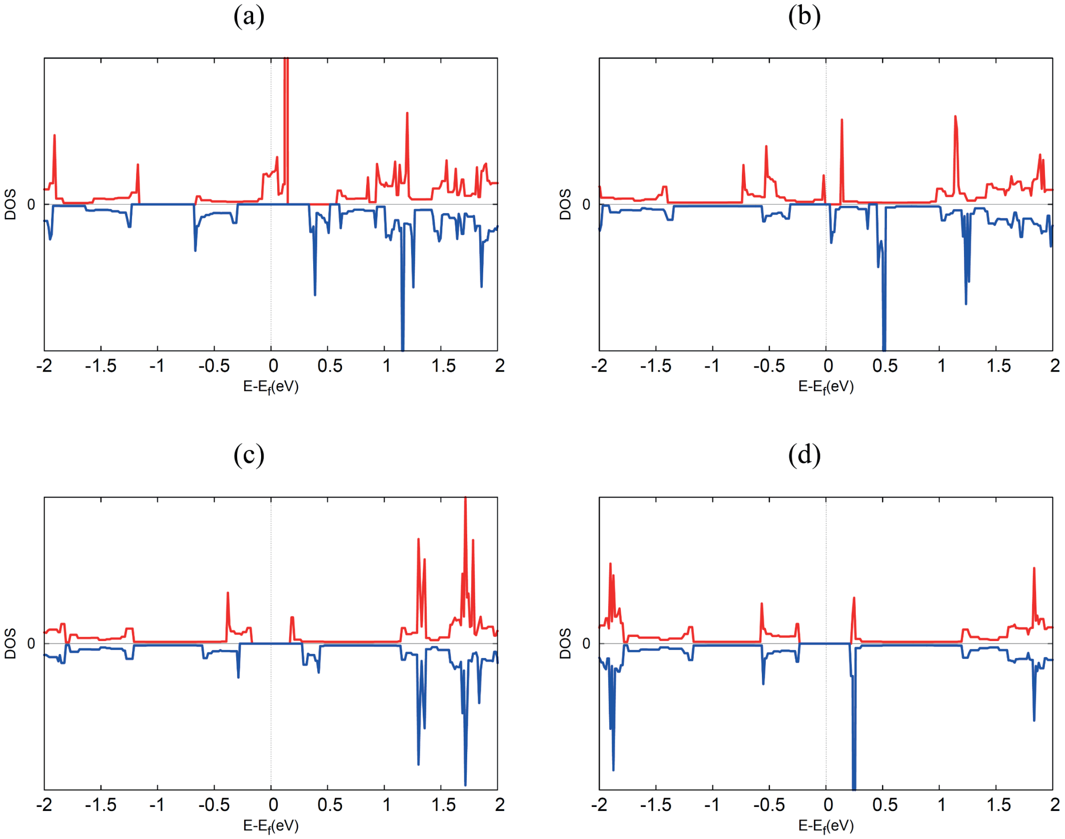

Figure 4-10: Density of states (DOS) of (a) **A**, (b) **S**, (c) $\mathbf{N}_0$, and (d) $\mathbf{N}_8$ for the α-spin (red) and β-spin (blue) states.

increased to 0.56 and 0.54 eV, respectively. As shown in Figure 4-5(d), the trend of the band gap variation of $\mathbf{N}_0$-$\mathbf{N}_8$ is due to the different environments (symmetry) of the odd-numbered carbon atoms (C1, C3, C5, and C7) and even-numbered carbon atoms (C2, C4, C6, and C8). Figure 4-10 shows the density of states (DOS) of **A**, **S**, $\mathbf{N}_0$, and $\mathbf{N}_8$. As seen in Figure 4-10, only the α-spin of **A** has a metallic character, while all of the others have band gaps. Thus, **A** should be a half-metal, while the others are semiconductors.

For noncovalent interactions, from $\mathbf{N}_0$ to $\mathbf{N}_8$, we analyzed charge transfer by the Bader method.[150–152] The plot in Figure 4-11 is a comparison of charge between the

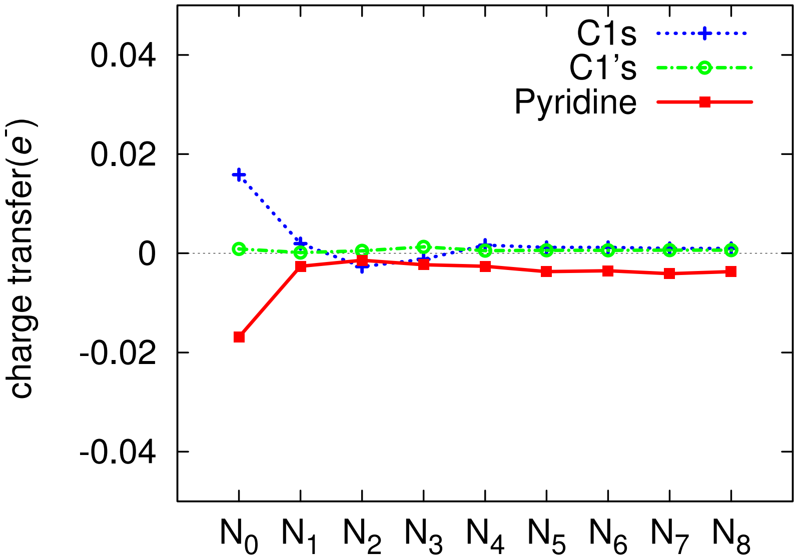

Figure 4-11: The charge transfer of the outmost atoms, which is corresponding to C1 (blue cross and dot line) and C1' (green empty circle and dot-dash line), is plotted in a comparison with pristine ZGNR from $\mathbf{N}_0$ to $\mathbf{N}_8$. And that of pyridine (red filled square and solid line) is plotted in a comparison with the isolated pyridine.

absorbed ZGNRs and the pristine ZGNR. The charge transfer was analyzed for the outmost C atoms in the supercell. At the edge to which pyridine is closer, a C atom gained 0.016 e^- in $\mathbf{N}_0$ and it dropped dramatically to 0.001 or 0.002 as pyridine absorbed in the middle site. The C atoms that were located at the opposite edge gained charges as well but the quantity is small. And the charge of pyridine also was compared between the absorbed on ZGNRs and the isolated. As pyridine absorbed, the charge transferred from pyridine to ZGNR. The loss of the charge of pyridine was the maximum in $\mathbf{N}_0$ by 0.017 e^-. Pyridine played a role of electron donor, and ZGNRs accepted charge from pyridine. The excess charges at an edge in ZGNRs may have partly contributed to the narrow band gap for the α-spin state. Moreover, it is noted that the location of pyridine is the significant factor to tune the band structure.

4.3.2 External electric field

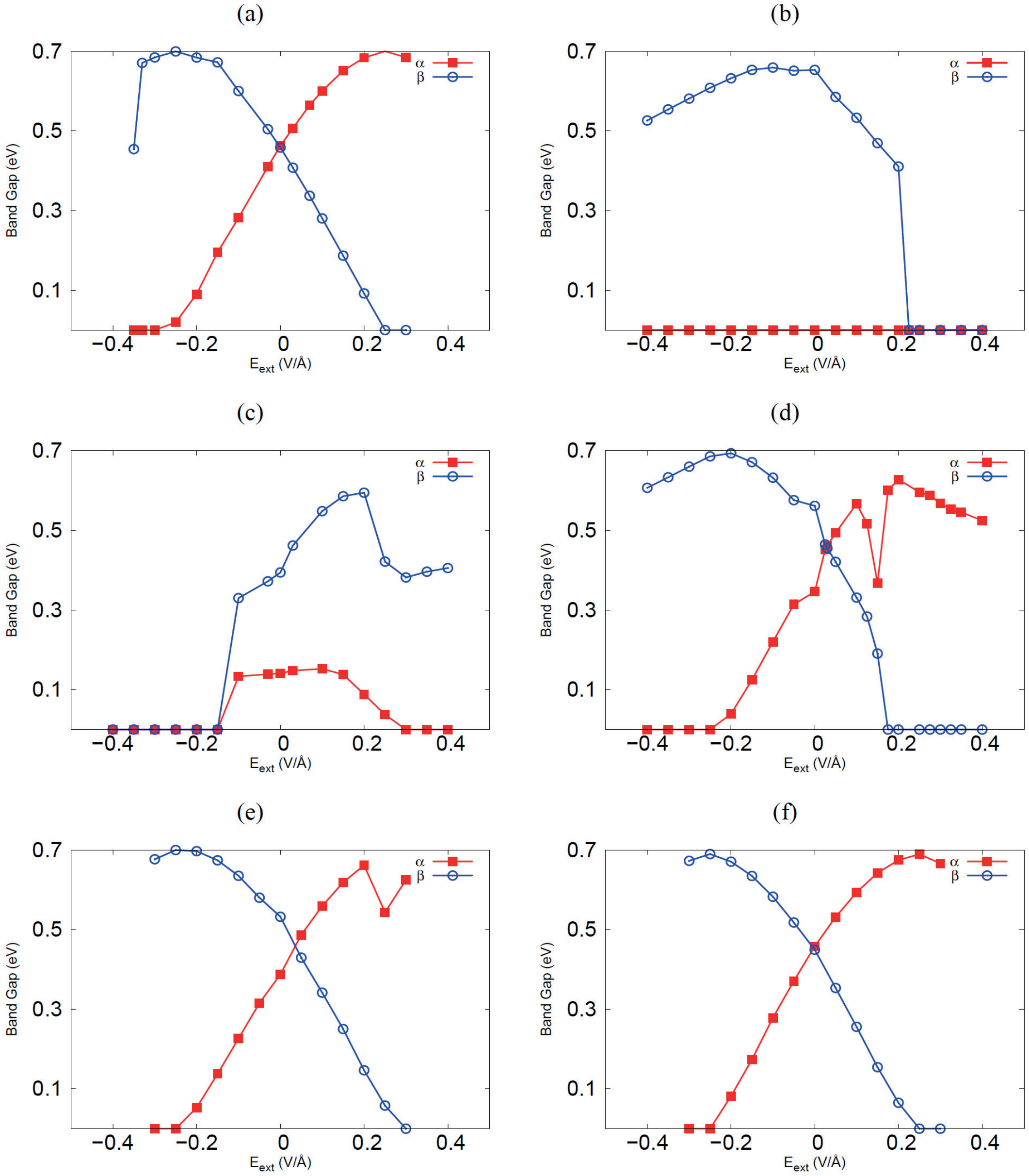

Figure 4-12: Band gaps of each α (red filled squares)- and β (blue empty circles)-states: (a) pristine graphene, (b) **A**, (c) **S**, (d) $\mathbf{N}_0$, (e) $\mathbf{N}_2$, and (f) $\mathbf{N}_8$.

We investigated the variation in the band gaps under different external electric fields along the y-axis. Figure 4-12 shows the band gap variation of a pristine ZGNR, **A**, **S**, $\mathbf{N}_0$, $\mathbf{N}_2$, and $\mathbf{N}_8$, under applied electric fields ranging from -0.4 to 0.4 V/Å. For the pristine ZGNR, the band gap of the α-spin increased, and that of the β-spin decreased as the field strength increased in the positive direction. The opposite behavior for the negative field was obtained, as shown in Figure 4-12(a). As such, the semiconducting ZGNR became half-metallic under an external electric field strength of around 0.25 V/Å, regardless of the direction, because the band gap of the β-spin (α-spin) disappears with field strengths higher than 0.25 V/Å (lower than -0.25 V/Å). This behavior is consistent with previous results.[118,119]

The electric field dependency of the band gaps of **A** and **S** is quite different from that of the pristine ZGNR. For **A**, the α-spin state does not have a band gap under the applied electric field, while the band gap of the β-spin decreased as the strength of the electric field increased in both directions and decreased more rapidly in the positive direction. As seen in Figure 4-12(b), for electric fields up to 0.20 V/Å, **A** retains its half-metallicity and becomes metallic under electric field higher than 0.2 V/Å. It appears that, near the Fermi level, the highest valence band of the α-spin state can be ascribed to the LUMO of the pyridine as well as to the delocalized π valence band of the ZGNR. For **S**, without an applied electric field, the band gap of the α-spin is lower than that of the β-spin. This is because the α-spin density is mostly localized at the pyridine, while the β-spin density is localized at the opposite edge. Thus, pyridine adsorption has a larger effect on the band gap of the α-spin state. As seen in Figure 4-12(c), for a positive applied electric field (ZGNR → pyridine), the band gap of the α-spin state changed little up to 0.15 V/Å and then decreased almost linearly to zero for fields higher than 0.30 V/Å. For a negative applied electric field, the trend is similar, but the cutoff electric field at which there is no band gap for the α-spin (E_0^α) is -0.20 V/Å. On the other hand, as the strength of the electric field increases in the positive direction, the band gap of the β-spin state of S increases, reaches a maximum at $\sim$ 0.2 V/Å, and then sharply decreases to a certain value. The trend of the field-dependent band gap of the β-spin in the negative direction looks similar to that of the α-spin, with a cutoff electric field for the β-spin (E_0^β) of -0.20 V/Å.

The electric field dependencies of the band gaps of $\mathbf{N}_0$, $\mathbf{N}_2$, and $\mathbf{N}_8$ are similar to that of the pristine ZGNR, as shown in Figure 4-12(d), (e), and (f). In particular, the band gaps of $\mathbf{N}_8$ showed almost identical behavior to that of the ZGNR. For $\mathbf{N}_0$ and $\mathbf{N}_2$, there is slight difference from the behavior observed for the ZGNR. At zero field, the band gaps of the α-spin for $\mathbf{N}_0$ and $\mathbf{N}_2$ are lower than those of the β-spin for the same reason as in the case of **S**. Thus, the band gaps of the α- and β-spin states can be equivalent under a positive electric field ($\sim$ 0.03 V/Å). The values of E_0^α (E_0^β) were calculated to be -0.25 V/Å (0.19 V/Å) and -0.25 V/Å (0.30 V/Å) for $\mathbf{N}_0$ and $\mathbf{N}_2$, respectively. It is interesting that the field-dependent band gaps of the α-spin for $\mathbf{N}_0$ and $\mathbf{N}_2$ show dips at $\sim$ 0.17 and 0.25 V/Å, respectively, although the reason is unclear at this point.

To investigate the influence of a Lewis acid on the band structures, we obtained band gaps by introducing BF_3 on the edge opposite to the edge at which the pyridine is bound. First, when only BF_3 is added on C2 of an otherwise pristine ZGNR, the β-spin band decreases down to 0.43 eV as listed in Table 4.1; the electrons of this band are localized at the edge far from the BF_3 as shown in Figure 4-13. This is opposite to the result obtained when pyridine was on C2. We then compared the interactions of pyridine-ZGNR with BF_3. We located BF_3 on the C0′, C1′, or C2′ of

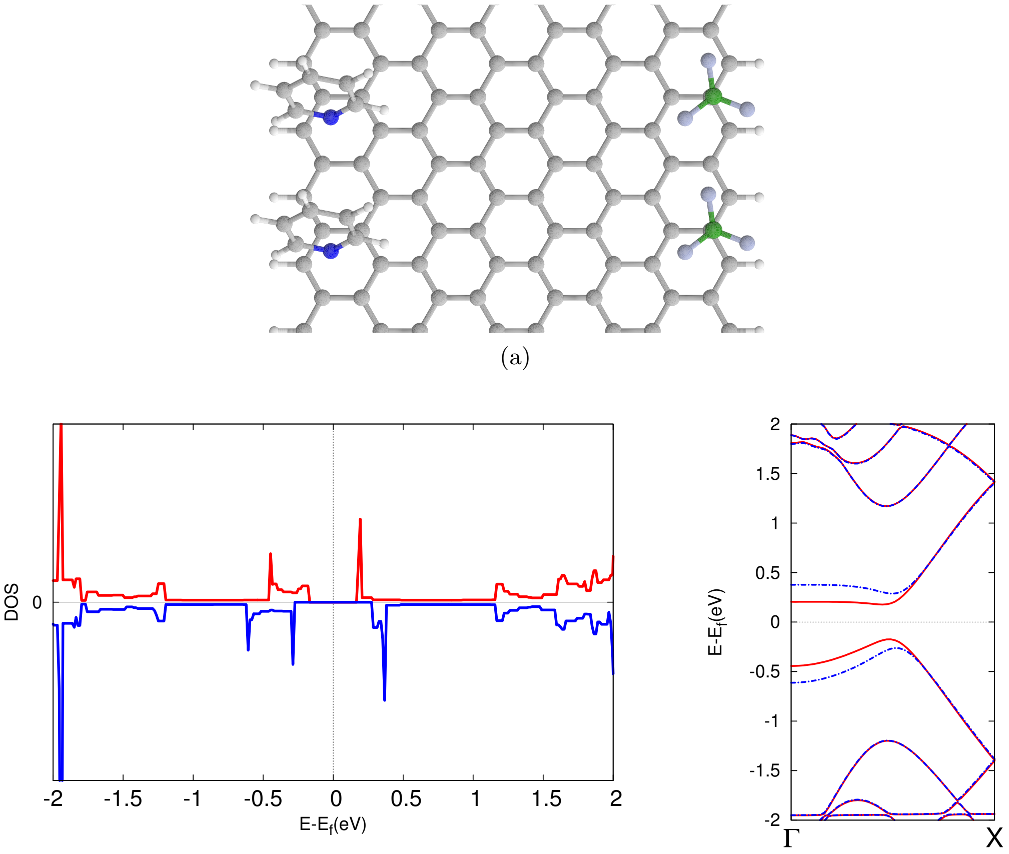

(a)

(b)

(c)

Figure 4-13: (a) Optimized geometries in which pyridine locates on C2 and BF_3 stays on C2', (b) DOS, and (c) band structure.

$\mathbf{N}_0$, and the results are shown in Table 4.2. BF_3 further reduced the band gap of the α-spin, while it increased the band gap of the β-spin. As noted in Table 4.2, BF_3 is most effective when it is on C1$'$, where the band gap of the α-spin state is reduced down to 0.28 eV (0.23 eV) as calculated using the PBE (PBE-D2) functional. This implies that a proper combination of electron acceptor and electron donor, which are absorbed chemically or physically on the ZGNRs, can be used to tune the band gaps of the α- and β-spin electrons of ZGNRs.

Table 4.1: Band Gaps (eV) of ZGNRs by Pyridine or BF_3 Adsorption on C2

absorbate	the α-spin state			the β-spin state		
	none	pyridine	BF_3	none	pyridine	BF_3
PBE	0.46	0.39	0.49	0.46	0.53	0.43
PBE-D2	0.46	0.40	0.49	0.46	0.52	0.42

Table 4.2: Band Gap (eV) Variation of $\mathbf{N}_0$ by BF_3 Adsorption at C0$'$, C1$'$, or C2$'$

	the α-spin state				the β-spin state			
	^{a}none	C0’	C1’	C2’	^{a}none	C0’	C1’	C2’
PBE	0.35	0.33	0.28	0.32	0.56	0.57	0.60	0.57
PBE-D2	0.35	0.34	0.23	0.31	0.56	0.56	0.59	0.58

^{a} No BF_3 adsorption (i.e., $\mathbf{N}_0$); ^{b} Carbon sites at which BF_3 interacts with $\mathbf{N}_0$.

4.4 Conclusions

We studied systematically the band structures of ZGNRs influenced by pyridine adsorption and external electric fields by means of first-principles calculations. It was found that modifying only one edge with pyridine resulted in half-metallicity, as is observed under strong electric fields or after carrier doping. In the case of pyridine adsorption (not a covalent bond), the band gap of the α-spin decreased, while that of the β-spin increased compared to the pristine ZGNR. For example, the band gaps of the α-spin of $\mathbf{N}_0$ and $\mathbf{N}_2$ structures were reduced to 0.35 and 0.39 eV, while the band gaps of the β-spin increased to 0.56 and 0.54 eV, respectively. Since pyridine is a base and an electron-donating group, it is expected that the band gap of ZGNRs could be enlarged by the adsorption of an electron-accepting molecule.

For a pristine ZGNR, the band gap of the α-spin increases, and that of the β-spin decreases as an electric field is applied in the $+y$ direction of Figure 4-1. The opposite behavior is observed for the $-y$ direction. As such, the semiconducting ZGNR becomes half-metallic at an external electric field strength of around 0.25 V/Å

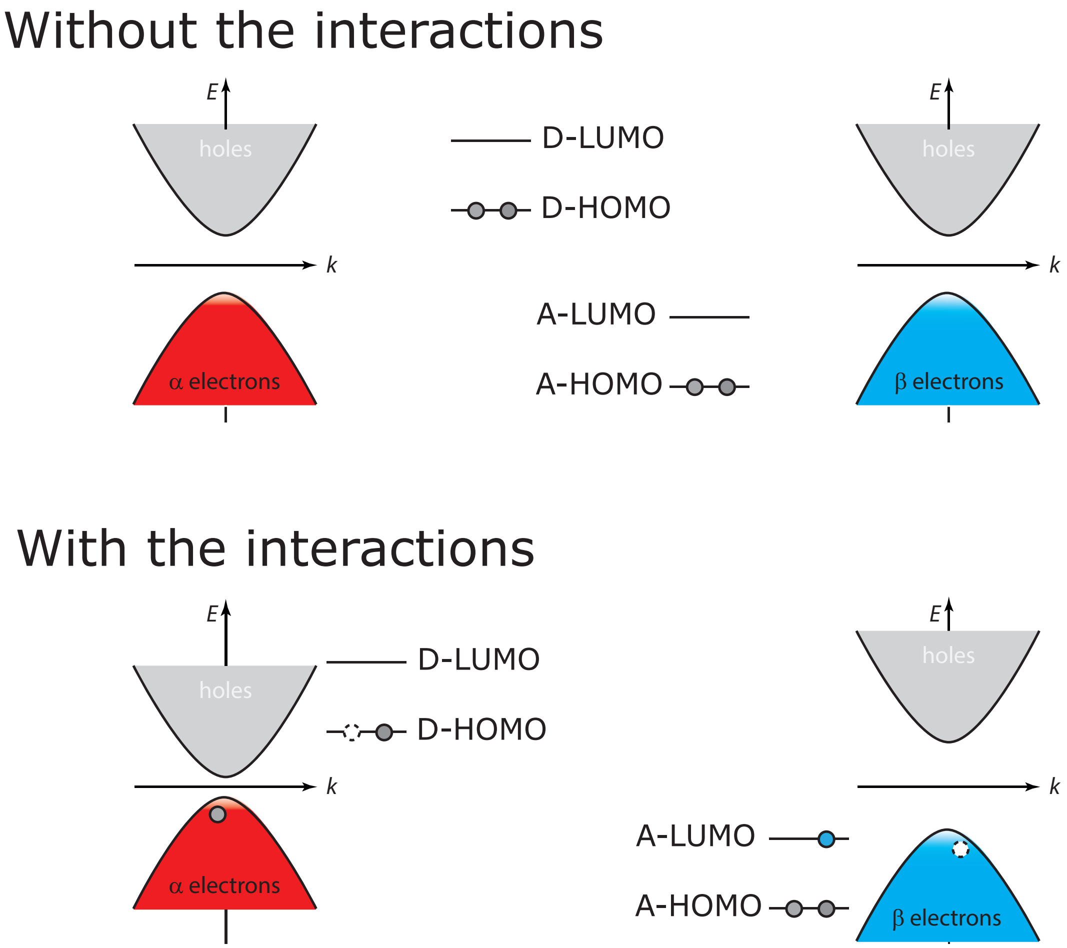
Without the interactions
E
holes
k
α electrons
D-LUMO
D-HOMO
A-LUMO
A-HOMO
E
holes
k
β electrons
With the interactions
E
holes
k
α electrons
D-LUMO
D-HOMO
A-LUMO
A-HOMO
E
holes
k
β electrons

Figure 4-14: The localized edge states and the band energy by electron donor and electron acceptor.

regardless of the direction of the field because the band gap of the β-spin (α-spin) disappears for field strengths higher than 0.25 V/Å (lower than -0.25 V/Å). However, the electric field dependency of the band gaps of **A** and **S** was quite different from that of the pristine ZGNR. For **A**, the α-spin state does not have a band gap under the applied electric field, while the band gap of the β-spin decreased as the strength of the electric field increased in both directions and decreased more rapidly in the positive direction.

Pyridine adsorption has a larger effect on the band gap of the α-spin state because the α-spin density is mostly localized at the pyridine, while the β-spin state is more localized at the opposite edge of the ZGNR. It was found that this tendency remained up to 64-ZGNR, which had band gaps of 0.04 eV for the α-spin and 0.15 eV for the β-spin. When electron-donating (pyridine) and -accepting (BF_3) molecules coexist at opposite edges from each other, the half-metallicity was enhanced (Figure 4-14). By introducing molecules at edges, it was found that the valence band was perturbed resulting in the band gap was modified. On the basis of our study, we propose that the adsorption of pyridine or any electron-accepting molecule on ZGNRs will be an easy and useful way to engineer the band gap (or open the band gap) for the use of GNRs in various devices.

Chapter 5

Migration and Removal of an Epoxide in Graphene Nanoribbons by the Width and an Electric Field

5.1 Introduction

The experimental achievement of GNR is limited to a few kinds of GNRs yet, of which geometry is simple and rough than the sophisticatedly designed model system.[7,20,37,53,54,56–61] To tune the band structure, it requires developing the synthesis method of precisely controlling width and edge geometry of GNRs at the atomic scale. The study on pristine GNR has, by the means of theoretical study, offered explanations of the chemical reactions for the synthesis of desirable geometry as well as the band gap. We are to deliberate this chapter to our DFT studies of ZGNRs with an epoxide group.

The features of zigzag graphene nanoribbons (ZGNRs) are distinguished from graphene and other derivatives.[10,153–156] They are owing to the different topology of the C-C bond from other derivatives, in which the edge is zigzag structure. On both edges are the valence and conduction state localized leading ZGNRs to be semiconducting with a finite gap within 1 eV,[4,157–159] which is called *edge state*. Otherwise, the gap of graphene is semiconducting with zero band gap. And it is possible that the gap size and the electronic structure is adjusted by the width of ZGNRs or the structure of edge by decorating chemically.[160,161] There, in other respects, are efforts in chemical bonds by interacting noncovalently with other metal atoms, polymers, or molecules.[141,162,163] For the purpose of the desirable matter, it requires the band gap to be open tactfully.

Graphene oxide (GO) is insulator in spite of metallic character of pristine graphene. But GO has two advantages compared with graphene. The conductivity can be controlled. The conductivity of GOs is increased by up to 4 orders of magnitude by reducing oxygen functional groups, while the oxidized areas are restored to

sp^2-bonded carbon networks.[44–46] Even though that is still lack behind that of pristine graphene by a factor of 10-100.[42,47] A number of atomically structural defects and oxygen functional groups with insulating properties are present on the plane.[48] In addition to the controllability for the conduction, it is feasible to obtain mass yield. Once graphite is oxidized, a stable aqueous dispersion of graphene is obtained in the form of individual graphene oxide sheet. The hydrophilic functional groups of basal plane of graphene facilitate exfoliation and dispersion in aqueous solutions. The method of mechanical exfoliation graphene limits to throughput or high-yield despite the highest quality of graphene, in the meantime, diverse techniques have been reported to acquire desirable fragments such as graphene nanoribbon and large size flakes with good quality at low cost as a result of much effort to circumvent such physical difficulties using GOs.[37] Chemical modification in solution would be one of the most efficient methods in which we can produce desirable derivatives from graphene. Especially, an epoxide group plays a role to graft molecules or polymers by opening the epoxide ring.[164–167] The synthesis of functional GNRs and the reaction on the basal plane may be achieved by understanding the reaction mechanism of GNRs depending on the oxygen functional groups.

A carbon monoxide (CO) molecule is taken as a reductant to study the reduction mechanism of an epoxide group from ZGNR in our study. A CO molecule takes up an O atom of epoxide group as the O atom was removed by CO experimentally.[168] There are theoretical studies as well that CO removes an epoxide group from graphene,[169,170] and CO adsorption on graphene sheet and the sp^2 reconstruction were observed at low temperature.[171] Furthermore, to trigger opening a bond of epoxide and C=C, it was proposed to reduce GO by CO under an external electric field.[172,173] By applying an electric field on ZGNRs, the removal of an epoxide group out of the basal plane of ZGNRs have been relatively less studied to our knowledge, although some studies are reported about reduction from graphene or graphene flake as above. It is significant to find the difference of the reaction from graphene due to the anisotropic structure of graphene fragments. In this work, we focused on the control of reduction reaction as well as the band structure by epoxide groups. Epoxy group is able to unzip graphene basal. GO unzipping is initiated by the strain generated by the cooperative alignment of epoxide group on a carbon lattice of graphene.[56–58] And the epoxide groups on ZGNRs is important for another reason for which CNTs (carbon nanotubes) are unzipped to form graphene nanoribbons by epoxide groups arranged linearly.[174,175] Moreover, an epoxide group is feasible to be controlled than a hydroxyl group. Most of the epoxide groups can be removed and form a C=C structure restoring sp^2 hybridization, though hydroxyl ($-$OH) groups bonded to the surface of GO cannot be reduced by hydrazine even at relative high temperature.[43]

Not only the reduction of GO is aimed at manipulating the matter restoring C=C bond, but also the control of the location of epoxide on graphene nanoribbon is a goal to design it by sophisticated patterns of oxidation. We hope our study contributes to the works of the electrochemically synthesis in which large-area and patterned graphene oxide was reduced by the potentiostatic method.[53] Opening the prospect of patterning oxidized regions on (reduced graphene oxide) RGO with nanometric resolution, RGO sheets was controllably reoxdized on a local scale by means of STM lithography.[54]

An epoxide group was in the middle of basal plane of ZGNR, as both the reactant state and the product state are shown in Figure 5-1. As the width is widening, the epoxide group is farther from the edges. But C atoms are connected infinitely along the longitudinal axis. The reduction of an epoxide group from anisotropy structure of ZGNRs would be compared with graphene and graphene nano-flakes.

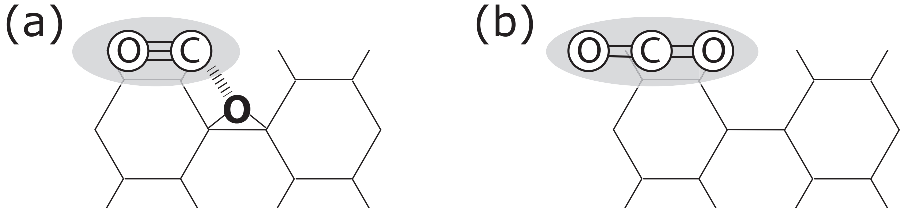

Figure 5-1: The scheme for the reaction: (a) the reactant state, and (b) the product state.

5.2 Computational Methods

Using Vienna *ab initio* simulation package (VASP) based on DFT with planewave [96–98], we performed calculations of 4, 6,and 8-ZGNRs with an epoxide group in the middle site. And the removal of epoxide by CO was compared with respect to the width.

In a supercell, as a scheme shown in Figure 5-2(a), there were five primitive rows of ZGNR where a unit cell was composed of 40, 60, and 80 carbon atoms for 4, 6, and 8-ZGNR, respectively. As the length of C−C bond was 1.42 Å the lattice length was 12.31 Å along the repeating axis. So as an epoxide group is distant 12.31 Å from the neighboring epoxide as repeated along the y-axis. And ZGNRs are separated by over 15 Å with vacuum, in the direction normal to the adjacent graphene nanoribbon.

During this DFT simulation, the electron-ionic core interaction was represented by the PAW potentials.[114,115] And the Perdew-Burke-Ernzerhof (PBE)[94,142] formulations of the GGA was implemented to treat electron exchange and correlation in the spin-polarized mode. And we included van der Waals interactions by Grimme's method[100] for the adsorption of CO and CO_2. The energy of physisorption for CO and CO_2 on graphene is reproduced poorly by GGA functional[176–178], so it was necessary to compensate the lack of dispersive forces in the geometry optimization for CO and CO_2. The cutoff energy for the planewaves was 400 eV. The k-point was sampled according to the Monkhorst-Pack automatic generation scheme with $1 \times 7 \times 1$ points.

Before we produced the transition state, we had optimized the geometries of the initial conformation and the final conformation. The initial state is the configuration where the physisorption of CO occurred around an epoxide group on ZGNR. When we relaxed the geometry of CO_2 on ZGNRs in the final state, we contemplated obtaining the geometry in the transition state by nudged elastic band (NEB) method. Because the configuration in the final state is ambient although the initial state is the configuration where CO approaches an epoxide group with energetically favorable conformation. The configuration of the final state may be the physisorption of CO_2 wherever a CO_2 molecule adsorbs favorably on ZGNR. We ought to obtain adequately the transition state geometry by NEB, so the final state should be chosen deliberately as the O atom left vertically from the ZGNR.

We compared the reaction paths and the barrier energies by NEB method, taking CO as a reductant. In order to obtain the transition state for the reduction by CO, we compared two paths of the reduction procedure as shown scheme of Figure 5-2(b). **E** denotes the reaction in which the reaction coordinate are started by CO being close to an edge, meantime, **M** describes the path in which the reaction coordinates are in the middle of the ZGNR. The rotational dynamics of CO_2 was ignored after the transition state for the reduction reaction. Therefore, the corresponding final states are the conformation where the CO_2 is parallel to the x-axis and y-axis in **E** reaction path and **M** reaction path, respectively. During the geometry optimization, the initial and final state were completed without any constraints. The energies and the forces on each ion are converges within 1.0×10^{-4} eV/atom and 0.01 eV/Å.

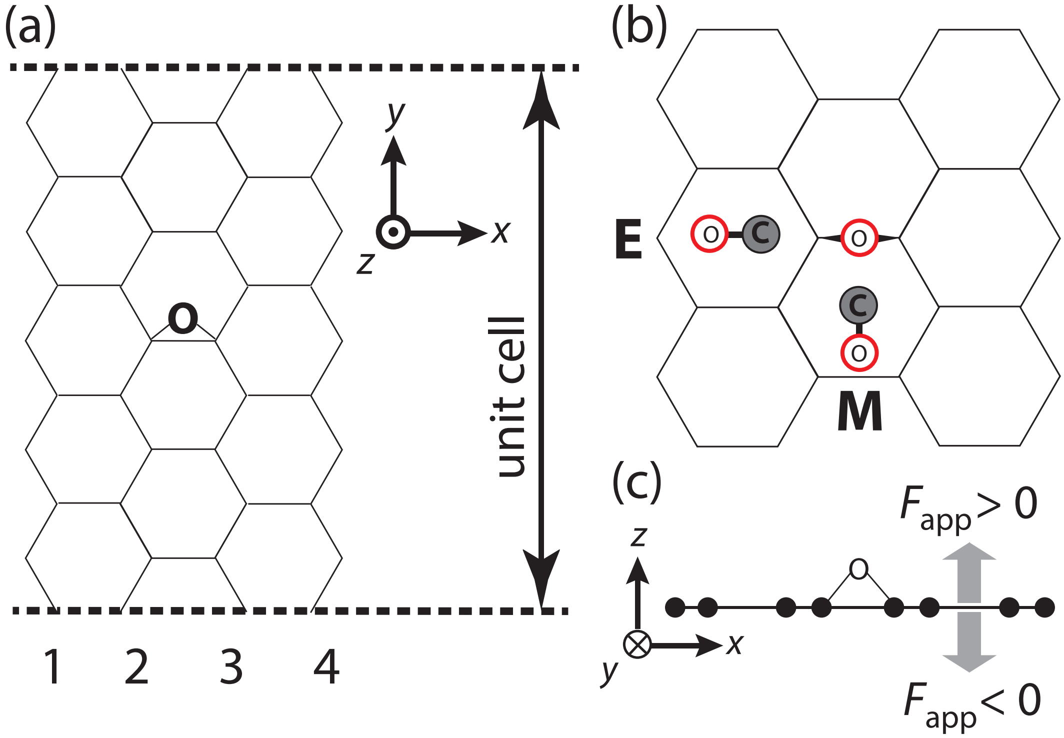

Figure 5-2: (a) An epoxide group is at the middle site of the plane of 4-ZGNR. (b) **E** and **M** are discerned by the different location at which a CO molecule absorbs. (c) The positive (negative) F_{app} means that the external electric field is applied in the same (opposite) direction of the z-axis.

5.3 Results and discussion

The electronic structure of ZGNRs is distinguished from pristine graphene by the localized state at edges. The edge state of ZGNRs appears ferromagnetic along the edges and antiferromagnetic to the opposite edge, in the ground state. Such electronic structures of ZGNRs might be perturbed by oxygen functional groups in the basal plane, in which an oxygen functional group forms covalent bonds on C atoms and even in which it is the transition state. While the functional group is interacting with π band of ZGNRs, the forming of bonds may shift the energy levels of π bands. We studied of the band structure depending on the location of an epoxide group in the basal plane of ZGNRs with various epoxide locations and ZGNRs widths. In order to control the locations for the purpose, furthermore, we relate the reaction barriers at the transition states. We investigated the influence of the reactions also under the change of the strength of an electric field, of which direction was along the z-axis.

5.3.1 Epoxide migration

While we studied the reduction reaction of an epoxide group from ZGNRs, we compared it with the migration reaction to a neighbor site on the ZGNR. It happens during the reaction in common that a bond of an epoxide is broken from initial conformation. Under the influence of the external electric field, if the external electric field assists to break a bond from the ZGNR, the migration of epoxide group for a neighbor C−C bond occurs possibly as it competes with the reduction to CO molecules, in the process of breaking and making bonds. As a result from the reduction reaction a CO molecule is oxidized to a CO_2 molecule, meantime, after the migration the product state is the conformation where an epoxide group is on the neighbor C atoms (Figure 5-3). By this comparison, moreover, we expect that it is helpful to understand the resultant conformation of a ZGNR with an epoxide depending on the features of the transition states with various strength of a vertical electric field and the possibility to control the location of the epoxide group.

We started the investigation of migration reactions as we relaxed the geometries of 4-, 6-, and 8-ZGNR with an epoxide group to be on the middle site along the width, as an schematic example in Figure 5-3(a). And we optimized the conformation in which the epoxide group is on the neighbor site, for the product state (Figure 5-3(a)). Taking the conformations as the reactant and product states, we found the geometry at the transition state by NEB method, as shown in Figure 5-3(b). With various widths for ZGNRs, total energies were analyzed. Their energies in the reaction were dependent on the width of ZGNR. Moreover, we measured the variation of the energies and bond lengths for the transition states applying an external electric field (F_{app}) with the strength from $-0.5\mathrm{V/Å}$ to $+0.5\mathrm{V/Å}$; in the sign of $+(-)$ of F_{app}, the positive (negative) electric field means along the same (opposite) direction with the z-axis.

As shown in Figure 5-4(a), the migration reactions from the middle site were exothermic reactions ($\Delta E^0 < 0$). When the epoxide group is out of the initial C−C site, the product conformation is more stable. Among the ZGNRs, 4-ZGNR appeared that the migration of epoxide change the ZGNR to be favorable by the greatest difference of 0.57 eV. And this difference was smaller as the width of ZGNR is large, as plotted in Figure 5-4(a). The energy difference ΔE^0 of the migration reaction was -0.27 and -0.16 eV for 6-ZGNRs and 8-ZGNRs, respectively.

The relative energies are in Figure 5-5, as an epoxide was at from the edge to the

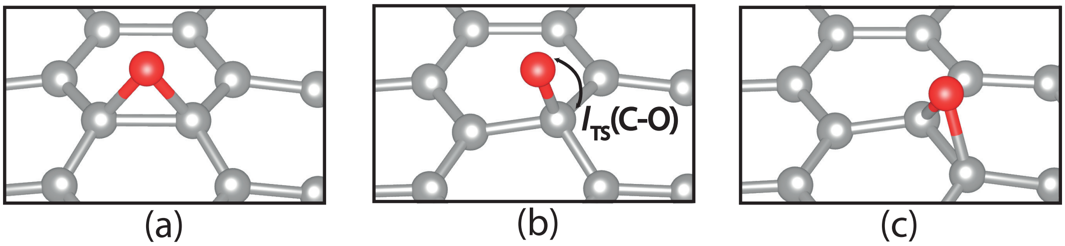

Figure 5-3: The figure depicts the bond and the geometry in the migration reaction, from (a) the reactant state, (b) the transition state, and (c) to the product state.

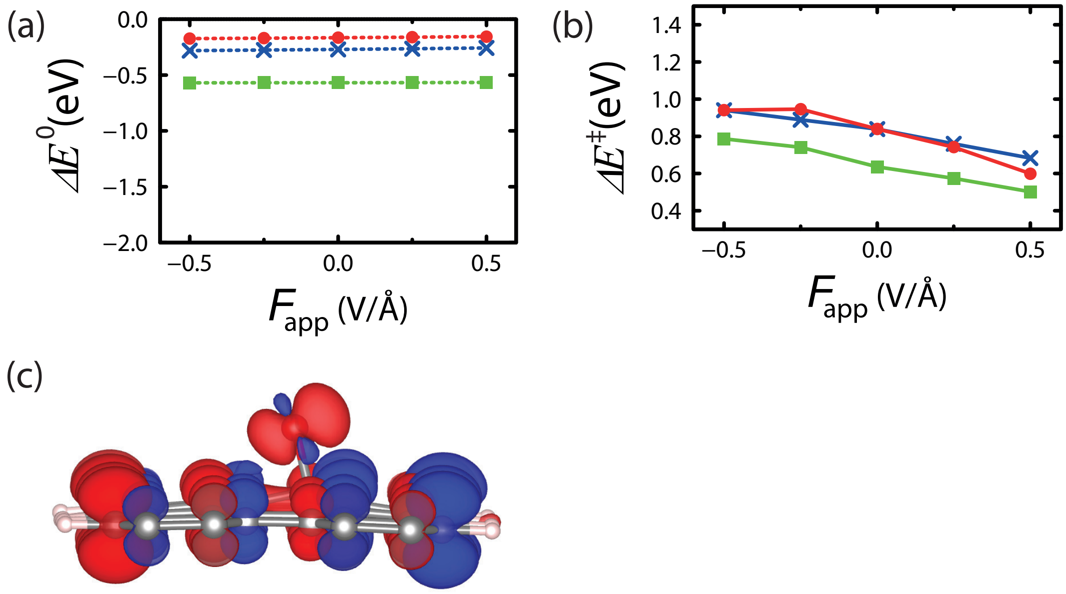

Figure 5-4: The plot depicts (a) the differences of the total energies between the reactant state and the product state (dotted line), $\mathit{\Delta} E^0$, and (b) the migration barriers (solid line), $\Delta E^{\ddagger}$ with respect to the electric field strength F_{app}. The green, blue, and red lines are for 4 (filled square)-, 6 (cross mark)-, and 8 (filled circle)-ZGNR, respectively. (c) The charge density difference is described, as the α- (β)-state charge is red (blue) at the transition state for 4-ZGNR.

middle site. When the epoxide is at the diagonal sites (C1−C2, C3−C4, C5−C6, and C7−C8), the conformation is more stable than the conformation of the neighbor sites. And the outmost site (C1−C2) is the lowest. The neighbor C−C bond is surrounded by fewer C atoms to the closer edge than the middle C−C bond, and the epoxide in a wider ZGNR is surrounded by more C atoms and C−C bonds. Otherwise, the epoxide move from the crosswise sites (C2−C3, C4−C5, C6−C7, and C8−C9), the migration reaction is exothermic reaction. We may infer that after the migration reactions the epoxide group is favorably at the diagonal sites.

It is the narrowest ZGNR that the barrier is the lowest among the epoxide-ZGNRs

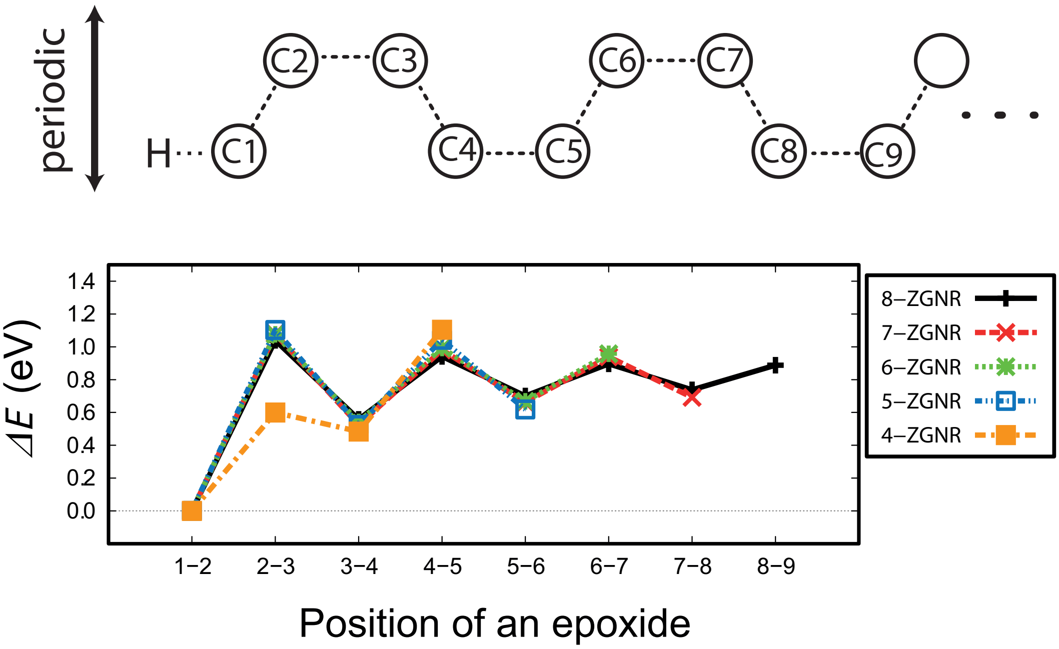

Figure 5-5: For ZGNRs with an epoxide, the relative total energies are referenced to the energy of the corresponding N-ZGNR in which an epoxide is at C1−C2 site.

in the absence of an electric field. The barrier was 0.64 eV for 4-ZGNR. It is lower by about 0.2 eV compared to 6- and 8-ZGNR. Although the energy difference between the initial and final state is not determined significantly by the strength of applying an F_{app}, the migration barrier dropped linearly by increasing F_{app} along the z-axis. The barrier energy for the ZGNRs dropped by about 0.3 eV under the variation of F_{app} from -0.50 to 0.50 V/Å along the z-axis. When an electric field was applied in the $+z$ direction (bottom → top), it assisted the migration by lowering the barrier height at the transition state. The geometric feature of the transition state is that an O atom retains a bond but the other bond was broken. And the length of C−O bond (l_{TS}(C-O)) is shorter than that of an epoxide group. The lengths were 1.456, 1.460, and 1.461 Å for 4-, 6-, and 8-ZGNR, respectively. This length was varied under the influence of an electric field. The length, l_{TS}(C-O), for the transition state was longer by about 0.02 Å as the l_{TS}(C−O) are in Table 5.1.

The Figure 5-4(c) depicts the charge density difference that the density of one spin (α-spin) state is subtracted by the density of another spin (β-spin) state. As shown in the figure, mainly α-spin state electrons at the transition state occupied a p-character orbital. It appeals to the reduction by a CO molecule to provide possibly the orbital to make a new σ-type bond.

5.3.2 Reduction of an epoxide

We are to compare the reaction barrier in the reduction of epoxide from ZGNRs with the migration reaction, applying the vertical electric field by various strengths in both directions: along the $+z$ (bottom → top) and $-z$ (top → bottom) axis. And the functional group was at the middle site along the width of ZGNRs as the migration reaction was. When ZGNRs are oxidized, an O atom forms two bonds with two C atoms. And the bonds of the C atoms turn into sp^3 hybridization by the oxidation. The reduction is a reverse reaction of an oxidation. In order for a CO molecule to reduce the ZGNR, two-single bond of epoxide should be broken and a double-bond be formed in CO_2. In the reduction, it is less stable configuration where one of two C−O bonds remain forming a bond meanwhile another is broken. For the reason, the reduction path in stepwise may results in remnants such as hydroxyl group.[179]

Table 5.1: In the transition state, the l_{TS}(C-O) (in Å) is varied depending on F_{app}.

F_{app} (V/Å)	4-ZGNR	6-ZGNR	8-ZGNR
-0.50	1.423	1.422	1.414
-0.25	1.425	1.420	1.420
0.00	1.436	1.426	1.426
0.25	1.433	1.429	1.436
0.50	1.444	1.437	1.446

As CO is a reductant, it is the purpose of the vertical electric field to assist the reduction reaction by lowering barrier energy. While we apply an electric field along the z-axis, these reductions by CO may be helpful in understanding of the breaking bonds of epoxide from the basal plane of ZGNR.

A reduction reaction is prepared by physisorption in which a CO molecule adsorbs around an epoxide group. The adsorption energies were compared in the case where CO are at either **E** or **M**. And we examined the favorable reaction path. And, by applying an electric field, we observed that the barrier heights were influenced by the direction and the strength of the electric field.

The **E** conformation is featured as the plane being given by CO and epoxide is parallel to the zx-plane, and the CO is relatively closer to an edge. At the middle, in the meantime, the **M** is the conformation in which the plane represented by CO and epoxide, and the plane is parallel to the yz-plane. The resultant CO_2, which is a linear molecule, is parallel to the x-axis and the y-axis, for **E** and **M**, respectively. The side view of **E** is shown in Figure 5-6(a) representatively.

As shown in Figure 5-6, the adsorption energies increased, as the applying electric filed (F_{app}) was stronger in the direction of $+z$. The adsorption energies was raised by about 20 meV. Even when F_{app} is applied, if the vertical electric field is applied from the plane of the ZGNR to an epoxide group ($+z$), the physisorption of CO is more favorable. It is noted that the conformation is stable under the influence of the positive F_{app}. In $+z$ direction, an electric field consistently strengthens the absorption and decrease the barrier height, the electric field efficiency will be greater. For the dependence of the width, however, it appeared that it is not a determinant factor to the adsorption energies. As increasing the width from 4 to 8-ZGNRs, the adsorption energies were larger within 0.01 eV, along the corresponding conformations under

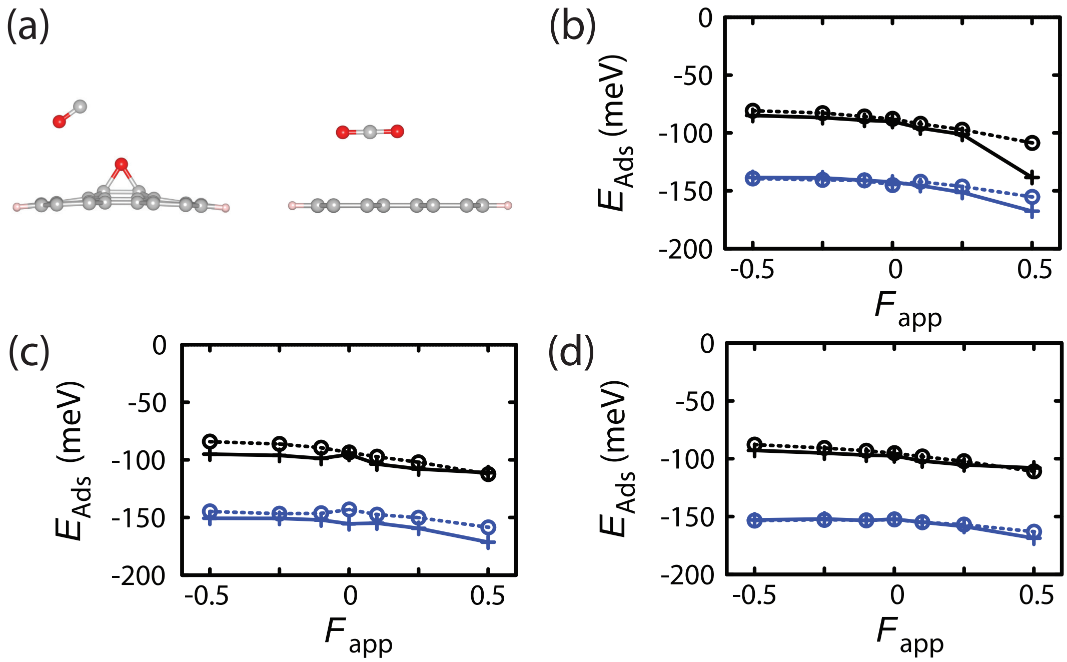

Figure 5-6: The adsorption energies (E_{ads}) are dependent on the conformation and F_{app}. (a) CO and CO_2 physisorb on the ZGNRs in **E**. The E_{ads} of (b) 4, (c) 6, and (d) 8-ZGNR increase as the F_{app} varies from -0.50 to 0.50 V/Å in the z-axis . The solid with cross and dotted lines with empty circle are for the conformation **E** and **M** respectively. The black line is for CO and the blue line is for CO_2.

the same strength F_{app}.

As the energy difference was slightly changed by the electric field, the reduction reaction is constantly exothermic reaction (Figure 5-7(a)). Before taking a close look into the transition state of **E** path, in comparisons with **M** reaction path, we found that **E** reaction path is favorable. We observed that the barrier height of **M** path is higher by about 0.3 eV at the corresponding strength of electric field, as shown in Figure 5-7(b). This reflects that stepwise reaction occur favorably than concerted reaction. In the Figure 5-8, the charge density difference is depicted for the **E** and **M** path at the transition state. A bond to which a p-orbital attribute was broken from the ZGNR as it forms newly a bond with CO in the **E** path. The charge density

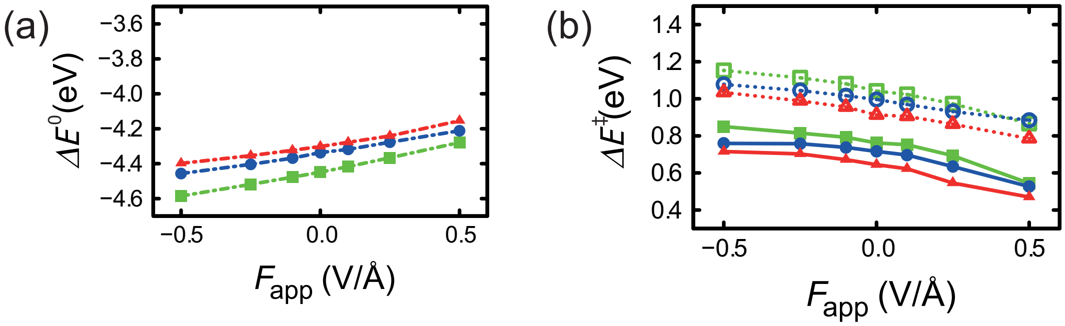

Figure 5-7: (a) F_{app} reduces the difference of total energies between the reactant and product state. (b) The plot depicts that the barrier heights was lowered by applying a vertical electric field. The solid with filled mark (dotted line with empty mark) denote **E** (**M**) reaction paths, and the green, blue, and red lines are for 4, 6, and 8-ZGNR, respectively.

difference was shown in the transition state of the migration, as shown in Figure 5-8(a). In the meantime, the p-orbitals are degenerate in the **M** path. It resulted in the higher barrier in their reaction paths.

The lowest barrier was for 4-ZGNR in the migration reaction. In contrast to the migration reaction, the barrier height $\Delta E^{\ddagger}$ was reduced as the width of ZGNR was wider. Among these reduction reactions, the lowest barrier was resulted from the 8-ZGNR, which is the widest ZGNR. It was 0.64 eV, and this is lower than the barrier in the migration reaction by 0.20 eV, in the absence of an electric field. Apart from

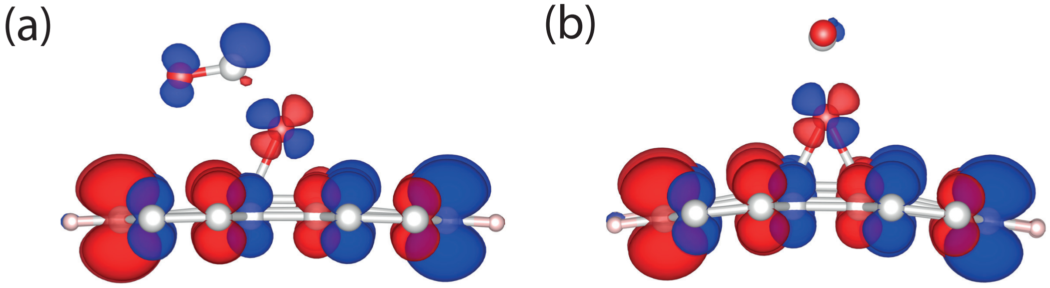

Figure 5-8: In the transition state, the charge density difference of (a) **E** and (b) **M** path is described by red and blue iso-surface, for the α- and β-state, respectively.

that, for 4-ZGNR, the barrier in the reduction reaction is higher than the barrier in the migration reaction. The reduction reaction requires more activation energy than the migration energy by 0.12 eV. This implies that by CO the reduction path occurs favorably than the migration for 8-ZGNR. By CO the reduction path is more stable than the migration by kinetic reaction control as a ZGNR is wider. If we want to get rid of an epoxide group of 4-ZGNR by CO, we should consider the pathway of migration consciously. Because the barrier in the migration reaction is lower than in the reduction reaction for 4-ZGNR. And it implies that the migration and reduction reactions are affected by the width of ZGNR or by the distance from an edge. An epoxide near edge would be unlikely removed than an epoxide near the middle site. Due to the lower barrier, the migration reaction is advantageous in kinetic control for 4-ZGNR. However, the reduction reaction is favorable for 8-ZGNR.

F_{app} influenced the barrier height.. The effect of F_{app} was similar to the case of the migration of epoxide. The Figure 5-7(b) shows that the barrier was reduced by applying a vertical electric field. In the reaction path **E**, $\Delta E^{\ddagger}$ decreased by about 0.20 eV, as F_{app} is from -0.50 ($-z$ direction) to 0.50 ($+z$ direction). With the assistance of a vertical electric field, the reduction by CO can be triggered. The l_{TS}(C-O) is longer as F_{app} is from -0.50 to 0.50. (Table 5.2) This supports that lengthened C$-$O bond is more stable as F_{app} is stronger in the $+z$ direction.

The lowering barrier height by an vertical electric field can be understood by the site-projected density of states (DOS), as the site-projected DOS is shown in Figure 5-9, in which for the O atom of the epoxide group p_x, p_y, and p_z states are decomposed. The p_x character orbital was influenced as the energy level was reduced (increased) by applying an electric field in the $+z$ ($-z$) direction. In the case of the broken bond, the electron in the p_x-orbital was localized, and this orbital is at lower level as the F_{app} increases. The p_y and p_z states are shown such that the band energies were lowed under the vertical electric field. But it is not as much as the p_x state. This implies that the electric field makes the orbitals be polarized and the p_x characters are more overlapped by the polarization. It results in the lower barrier height by the overlap of the LUMO of CO and p_x-character state of epoxide at the transition state.

5.4 Conclusions

By CO as a reductant, we studied the reduction of epoxide from ZGNRs under the influence of a vertical electric field. And the reactions were compared as an epoxide functional group was on the middle of 4, 6, and 8-ZGNRs. With this constraint for the initial position of the epoxide, we expected that the reduction is understood not only of the dependence on the width of ZGNR but also of the reliance on how close to the zigzag edge of graphene an epoxide is.

We studied the reduction reaction as well as the migration to the neighbors. And it was found that the reduction reactions can be competed with the migration reaction

Table 5.2: The l_{TS}(C-O) (in Å) is varied depending on F_{app}, in the reactant state (RS) and the transition state (TS).

State	F_{app} (V/Å)	4-ZGNR	6-ZGNR	8-ZGNR
RS	-0.50	1.445	1.448	1.450
	-0.25	1.449	1.453	1.456
	0.00	1.454	1.456	1.459
	0.25	1.459	1.463	1.467
	0.50	1.464	1.467	1.472
TS	-0.50	1.675	1.558	1.519
	-0.25	1.679	1.560	1.517
	0.00	1.682	1.565	1.522
	0.25	1.698	1.578	1.530
	0.50	1.703	1.582	1.533

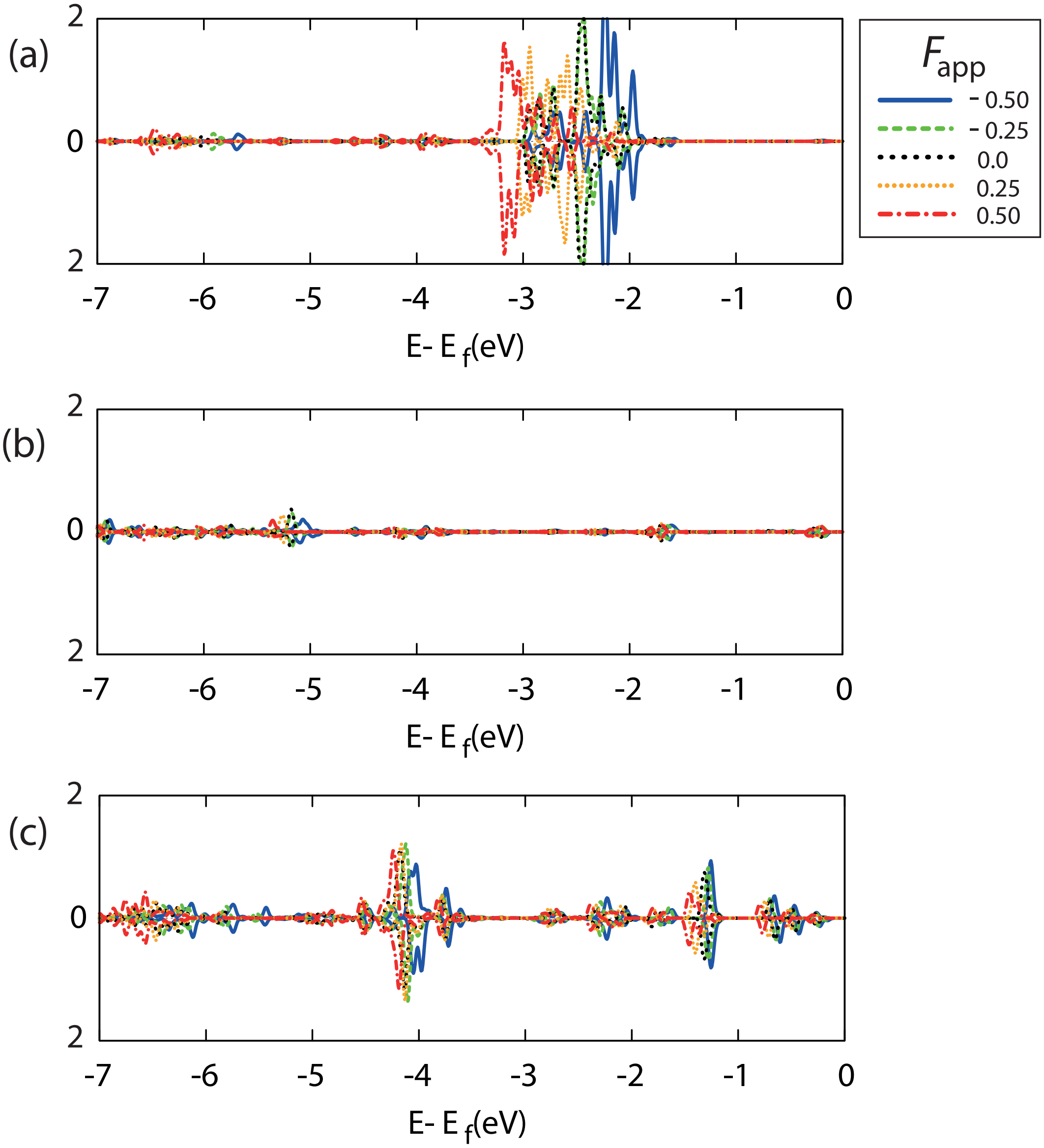

Figure 5-9: The site-projected DOS is plotted for the O of epoxide in the transition state for (a) p_x, (b) p_y, and (c) p_z states. In each plot, the upper and lower site-projected DOS is for α- and β-spin state, respectively.

for narrow ZGNRs. Due to the favorable migration, it ought to be appreciated more carefully whether the height of the reaction barrier is comparable to the barrier of the reduction reaction under the vertical electric field. By the consideration of the barrier height, the result showed that an epoxide migration occurs at most frequently on the narrowest ZGNR, which was 4-ZGNR, by the lowest potential barrier in the exothermic reaction.

As we researched paths by relating **E** to **M** in the reduction reaction of epoxide by CO from ZGNRs, it was unraveled that the reduction reaction occurs likely in the asynchronous transition structure in **E** than **M** path. And we took a close look into the **E** reduction path. Although the reaction barrier was lower as the ZGNR is narrower in the migration reaction, the incremental width of ZGNR reduced the barrier height in the reduction reaction. It is worth noting that the potential barrier of the reduction is higher for 4-ZGNR, in contrast to, that of the migration is higher for 8-ZGNR. This fact reflects that in the transition state the reorganization energy increased with the increments of ZGNR width, in the reduction reaction by CO. For wider ZGNRs, using CO as a reductant, the reduction of epoxide is more efficient.

By applying a vertical electric field, it appeared that the potential barrier is lowered when the external electric field in the direction being perpendicular to the basal plane, from the bottom to an epoxide (the top). The lowering barrier height was shown in the both case of the migration and the reduction reaction. The vertical electric field stabilizes the transition state. We observed the p_x-state orbital of the O of epoxide was most effectively lowered by applying a vertical electric field in $+z$ (bottom → top) direction at the transition state of the reduction by CO. As a result, the barrier height decreased by about 0.3 eV within the range of F_{app} from -0.5 to 0.5 eV. It is applicable that by applying a vertical electric field an epoxide group would be removed by CO to be tuned to the desirable structure.

Chapter 6

Concluding Remarks

Graphene comprise C atoms and the C−C bonds in hexagonal networks, and the bonds are in sp^2 hybridization. The feature of the electronic structure of graphene is mainly attributed to the p_z orbital on each C atom in the two-dimensional arrangement, in real space. As the highest valence band and the lowest conduction band are degenerate in a linear dispersion relation, at the K points in reciprocal space, graphene appears to have unique properties such as massless Dirac fermions and quantum Hall effects. However, the two-dimensional structure turns into the quasi-one-dimensional structure with a finite width and the edges. It is graphene nanoribbon (GNR). The electronic structure is different from that of graphene by the edge structure. Due to the symmetry in reciprocal space, the band gap is no longer zero nor in liner dispersion relation, as the two-dimensional periodicity is broken. Depending on the edge structure especially, the GNR is metallic or semiconducting. In particular, a GNR with zigzag edge structure has a finite band gap, and a state of which energy is near the Fermi level is localized at the edge. Because it is the ground state that the α- or β-spin state is alternating on every p_z orbital of C atoms, a spin state is localized along an edge. We were willing to manipulate the electronic structure by introducing the localized state in molecules and functional groups. The spin state could be tuned in zigzag graphene nanoribbon (ZGNR).

In order to understand the properties of the electronic band structure that is represented in reciprocal space, it was intriguing issue for us to comprehend the relation the arrangement in real space and the energy in reciprocal space. The atoms of GNR are arranged in real space and the repeated local states result in a band structure in reciprocal space. Because of the edge state, at an edge or near the edge is the chemical reaction important to be controlled the location of adsorbates and functional groups. The properties of GNRs, however, have been observed in much less number of successful experiments and the the GNRs are limited to some derivatives still, compared with the experiments of graphene. It is the reason for which it is difficult to synthesis a GNR with a finite width with repeated functional groups. To synthesize a desired structure of GNR is a challenging work.

We studied on functional molecular systems for graphene nanoribbons by density functional theory. The DFT method is advantageous to compute a system in periodic boundary conditions. The uncorrelated electronic wavefunctions are expressed and integrated over the spatial coordinates for the Coulomb and exchange energies in the Hartree-Fock method. In the meantime, the electron density is determined and the physical property is obtained by the approximated functional to the exchange-correlation energy that is expressed by the local electron density and the gradient of electron density usually. In the DFT, as we used PBE functional, we verified the results and compared with other reported results which were given by the tight-binding model and other functionals—such as LDA (local density approximation), GGA (generalized gradient approximations), and hybrid-functionals. We found that our results are consistent with other reported results, in terms of the tendency of the electronic and magnetic structure depending on the geometric features such as edge structures, widths, and periodicities. And we noticed that the physical and electronic properties are constant for the supercells of which number of C atoms are various but identical for the corresponding width of ZGNR and for the magnetic structure.

As the electronic band structures of ZGNRs were studied systematically by means of first-principles calculations, it is noted that the influence of absorbates and external electric fields lead the valence band to shift the energy level. By forming a covalent bond, to modify only one edge with pyridine resulted in half-metallicity, as it was observed under strong electric fields or after carrier doping. In the case of pyridine adsorption (not a covalent bond), the band gap of the α-spin decreased, while that of the β-spin increased compared to the pristine ZGNR. Furthermore, as the distance between a pyridine molecule and the neighboring pyridine increased or the width of ZGNR was wider, the effect of pyridine was weaker as the coverage was lower. The band gap difference between the α- and β-spin states was reduced. The charge transfer showed that pyridine donated electrons to ZGNR and this turned out that the band gap was narrowed, for the spin state in which the electrons are localized at the near-pyridine edge and that the band gap was wider for the opposite spin state in which the electrons are localized at the far-pyridine edge. Since pyridine is a base and it is prone to donate its electrons, it is expected that the band gap of ZGNR could be enlarged by the adsorption of an electron-accepting molecule by the redistributing of electrons. Pyridine adsorption has a larger effect on the band gap of the α-spin state because the α-spin density is mostly localized at the pyridine, while the β-spin state is more localized at the opposite edge of the ZGNR. In addition to the role of the electron donor and acceptor alone, when electron-donating (pyridine) and -accepting

(BF_3) molecules coexist at opposite edges from each other, the half-metallicity was enhanced.

For a pristine ZGNR, the band gap of the α-spin increases, and that of the β-spin decreases as an electric field is applied in the $+y$ direction (α-electrons localized edge $\rightarrow$ β-electrons localized edge). The opposite behavior is observed for the $-y$ direction (β-electrons localized edge $\rightarrow$ α-electrons localized edge). As such, the semiconducting ZGNR becomes half-metallic by a sufficient strength of an external electric field. We observed that a less strength electric field is required to make ZGNR half-metallic when pyridine and BF_3 are located at the opposite edge. However, the electric field dependency of the band gaps of **A** and **S** was quite different from that of the pristine ZGNR. For **A**, the α-spin state does not have a band gap under the applied electric field, while the band gap of the β-spin decreased as the strength of the electric field increased in both directions and decreased more rapidly in the positive direction. The half-metallicity is persistent to an electric field when the band structure was originated in the covalent bond. On the basis of our study, we propose that the adsorption of pyridine or any electron-accepting molecule on ZGNRs will be an easy and useful way to engineer the band gap (or to open the band gap) for the use of GNRs in various devices.

Removal of epoxide is crucial to recover the defected bonds. Furthermore, as we tuned the band structure by pyridine and BF_3, it was noted that the location of a molecule and a functional group should be controlled. Because it is relatively easy to oxidize graphene, if the location epoxy can be controlled the epoxide group would provide the anchor to adsorb or the initial site to reaction on a specific site. By CO as a reductant, we studied the reduction of epoxide from ZGNR under the influence of a vertical electric field. And the reactions are compared ZGNRs with various widths, as an epoxide functional group was on the middle of 4, 6, and 8-ZGNRs. We investigated the migration reactions as well to the neighbor site. Due to the favorability of migration, it ought to be appreciated more carefully whether the barrier height of the migration reaction is comparable to the barrier of the reduction reaction under the vertical electric field.

The result showed that the migration reaction of an epoxide occurs on the narrowest ZGNR with the lowest barrier in exothermic reaction, which is 4-ZGNR. Subsequently, we compared the reduction reaction of epoxide by CO, from ZGNRs. It was unraveled that the reduction reaction occurs likely in the asynchronous transition structure. In contrast to the migration reaction, moreover, the incremental width of ZGNR reduced the barrier height in the reduction reaction. It is worth noting that the potential barrier of the reduction is higher for 4-ZGNR, on the other hand, that of the migration is higher for 8-ZGNR. By applying a vertical electric field in common, the result of applying an external electric field appeared that the potential barrier is lowered when the direction perpendicular to the basal plane and from the bottom to an epoxide. The lowering barrier height was shown in the both case of the migration and the reduction reaction. The vertical electric field stabilize the transition state by shifting the p_x-characteristic orbital of the O atom of epoxide to the lower energy level. It is applicable that by applying a vertical electric field an epoxide group would be removed by CO or moved to the neighbor sites to be tuned to the desirable electronic band structure.

It is challenging yet to synthesis a desirable GNRs with a narrow width within 10 nm. The GNRs which is chemically modified in sophisticated structure may be much more difficult practically. However, the chemically decorated ZGNRs have been shown to be promising for spintronics through many theoretical studies, and we found the possibility by means of DFT that GNRs can be tuned by small molecules as well. The arrangement of molecules as well as an electric field may lead to GNRs to be half-metallic. In addition, we proposed the reduction epoxide from the basal plane of ZGNR by the assisting of an electric field. Because the covalent bonds contribute to the band structure with more stable coordinate and with stronger interactions, a tuned GNR can be acquired by controlling the epoxide on the basal plane under applying an electric field.

There is practically a limit to control the reactions in solutions, in order to construct an asymmetric structure along a longitudinal GNR with a very narrow width, because it is in a homogeneous condition in the solution. As for the reason, it is difficult to make a reaction intentionally to locate a functional group or a molecule on a specific site across the width of ZGNR, of which edges are unbalanced with them. However, by applying an electric field, the energy level of the band is shifted with the polarization of orbitals, and the condition in chemical reactions are varied in the space within the system. We found the clue of the method to tune the electronic structure of GNRs, by coupling with small molecules and functional groups with assisting of an electric field. And the changed electronic structure results in different reaction condition. These would provide the controllable reaction paths by an electric field with the adequate direction and strength in the chemical reactions of GNRs.

Appendix A

Band structures under an external electric field

In the chapter 4, we presented the band structures when an electric field was absent. Here, the figures are the band structures when an electric field was given by various strengths for $\mathbf{A}$ and $\mathbf{N}_0$.

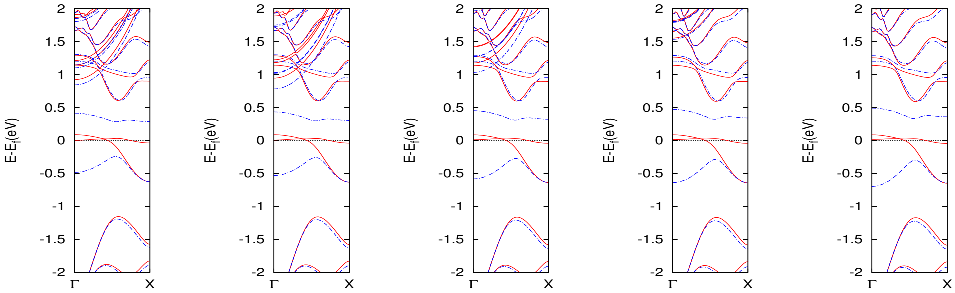

(a) -0.40 eV/Å (b) -0.35 eV/Å (c) -0.30 eV/Å (d) -0.25 eV/Å (e) -0.20 eV/Å

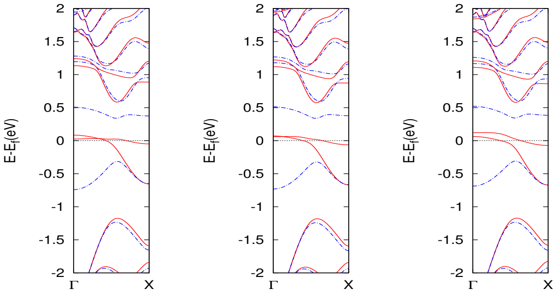

(f) -0.15 eV/Å (g) -0.10 eV/Å (h) -0.05 eV/Å

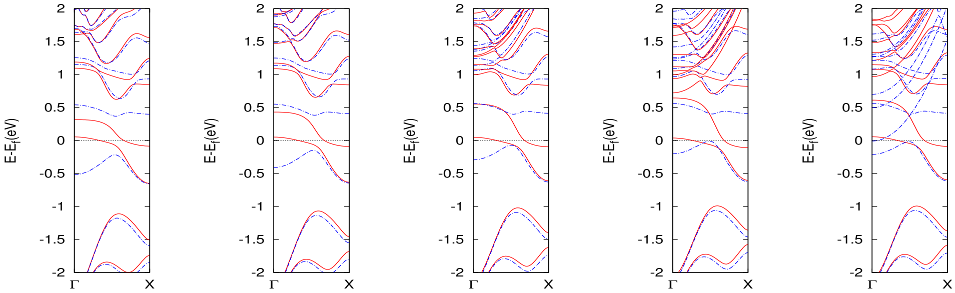

(i) 0.05 eV/Å (j) 0.10 eV/Å (k) 0.15 eV/Å (l) 0.20 eV/Å (m) 0.225 eV/Å

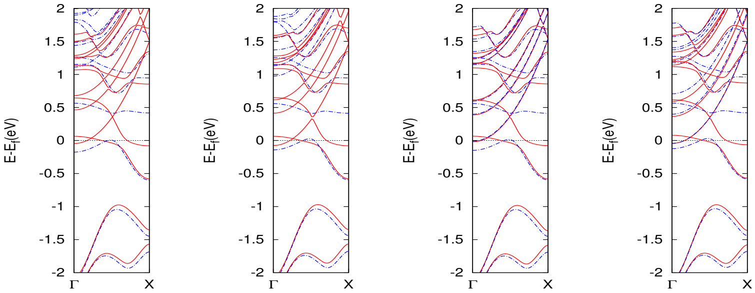

(n) 0.25 eV/Å (o) 0.30 eV/Å (p) 0.35 eV/Å (q) 0.40 eV/Å

Figure A-1: Band structure of **A**. The valence and conduction band is shifted under the external electric field.

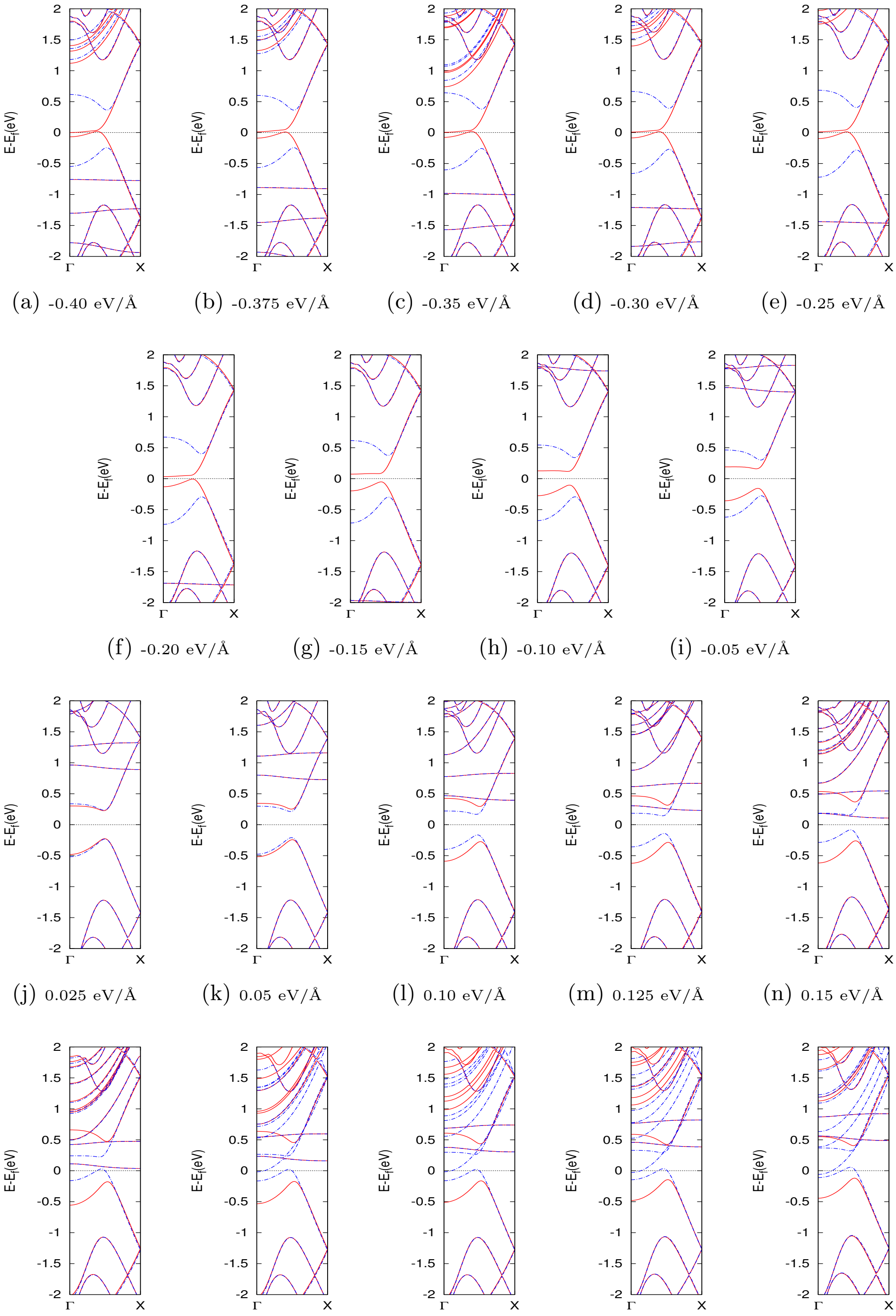

(a) -0.40 eV/Å (b) -0.375 eV/Å (c) -0.35 eV/Å (d) -0.30 eV/Å (e) -0.25 eV/Å

(f) -0.20 eV/Å (g) -0.15 eV/Å (h) -0.10 eV/Å (i) -0.05 eV/Å

(j) 0.025 eV/Å (k) 0.05 eV/Å (l) 0.10 eV/Å (m) 0.125 eV/Å (n) 0.15 eV/Å

(o) 0.175 eV/Å (p) 0.20 eV/Å (q) 0.25 eV/Å (r) 0.30 eV/Å (s) 0.40 eV/Å

Figure A-2: Band structure of $\mathbf{N}_0$. The valence and conduction band is shifted under the external electric field.

Appendix B

Band structures of 8-ZGNR with an epoxide group

On the basal plane of ZGNR, an epoxide group forms covalent bonds. The total energy of a complex is different by the location of epoxide. The total energies were presented in Chapter 5, with the respect to the location of epoxide along the width. In order to tune the band structure by the location, we investigated the band structures as well. The band structures were varied depending on the location as shown in Figure B-1. When the epoxide group is at edge and the orientation of C$-$C is diagonal, there is a band gap difference between α- and β-spin states. As the difference diminished as the epoxide is nearer the middle site and the epoxide is at the horizontal direction sites (Figure B-2). The epoxide which is at the middle site affects no longer the band gap difference between the α and β-spin state bands.

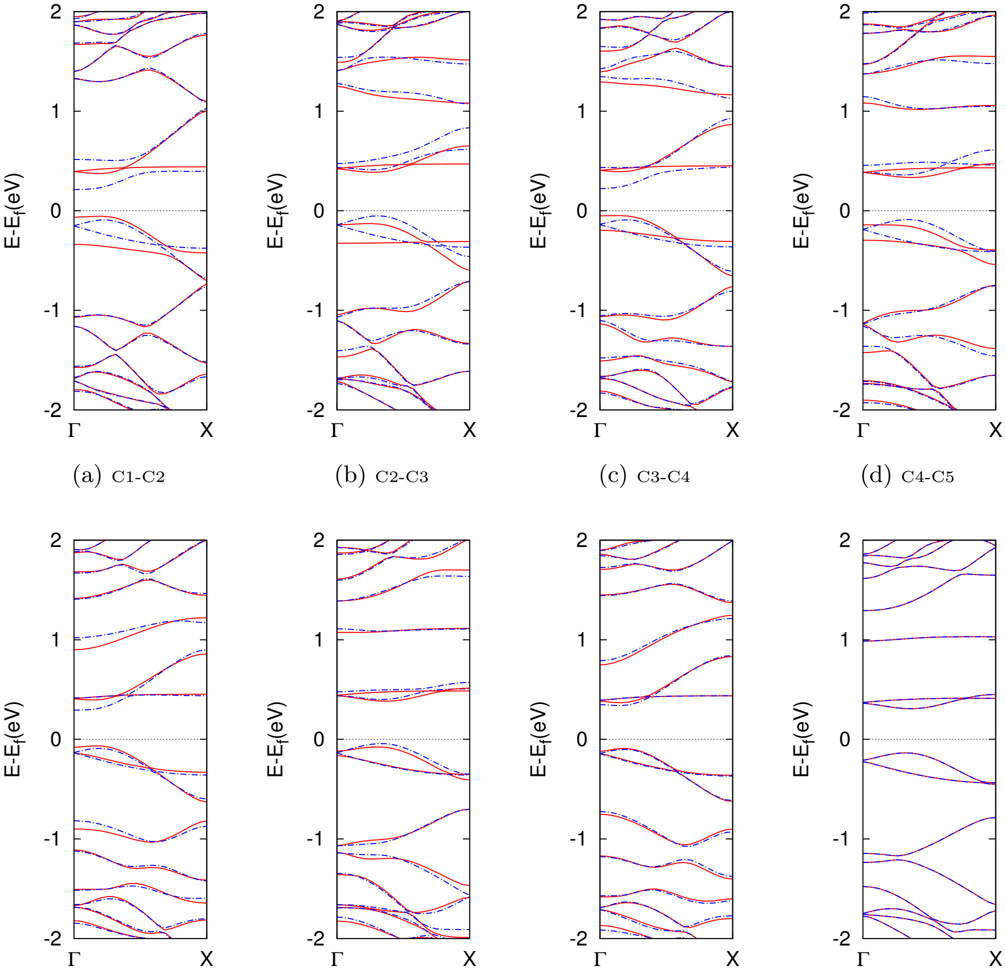

(a) C1-C2 (b) C2-C3 (c) C3-C4 (d) C4-C5

(e) C5-C6 (f) C6-C7 (g) C7-C8 (h) C8-C9

Figure B-1: The band structures of 8-ZGNRs with an epoxide group. The location of an epoxide group is at between (a) C1 and C2, (b) C2 and C3, (c) C3 and C4, (d) C4 and C5, (e) C5 and C6, (f) C6 and C7, (g) C7 and C8, and, (h) C8 and C9.

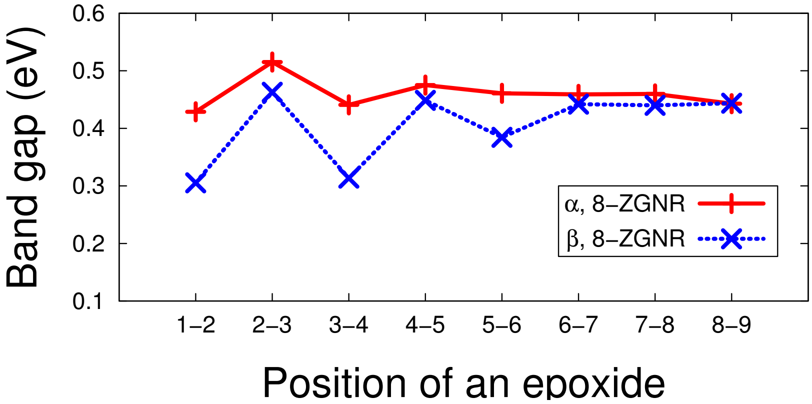

Figure B-2: The band gaps for the α- and β-spin states with respect to the location of epoxide.

Bibliography

[1] P. Wallace, "The band theory of graphite," *Phys. Rev.*, vol. 71, no. 9, pp. 622–634, 1947.

[2] J. Slonczewski and P. Weiss, "Band structure of graphite," *Phys. Rev.*, vol. 109, no. 2, pp. 272–279, 1958.

[3] N. Hamada, S.-I. Sawada, and A. Oshiyama, "New one-dimensional conductors: Graphitic microtubules," *Phys. Rev. Lett.*, vol. 68, no. 10, pp. 1579–1581, 1992.

[4] M. Fujita, K. Wakabayashi, K. Nakada, and K. Kusakabe, "Peculiar localized state at zigzag graphite edge," *J. Phys. Soc. Japan*, vol. 65, no. 7, pp. 1920–1923, 1996.

[5] K. Wakabayashi, M. Fujita, H. Ajiki, and M. Sigrist, "Electronic and magnetic properties of nanographite ribbons," *Phys. Rev. B*, vol. 59, no. 12, pp. 8271–8282, 1999.

[6] Y. Zheng and T. Ando, "Hall conductivity of a two-dimensional graphite system," *Phys. Rev. B*, vol. 65, no. 24, pp. 2454201–24542011, 2002.

[7] J. Cai, P. Ruffieux, R. Jaafar, M. Bieri, T. Braun, S. Blankenburg, M. Muoth, A. P. Seitsonen, M. Saleh, X. Feng, K. Müllen, and R. Fasel, "Atomically precise

bottom-up fabrication of graphene nanoribbons," *Nature*, vol. 466, no. 7305, pp. 470–3, 2010.

[8] O. Hod, V. Barone, J. E. Peralta, and G. E. Scuseria, "Enhanced half-metallicity in edge-oxidized zigzag graphene nanoribbons," *Nano Lett.*, vol. 7, no. 8, pp. 2295–9, 2007.

[9] A. B. Kaiser and V. Skakalova, "Electronic conduction in polymers, carbon nanotubes and graphene," *Chem. Soc. Rev*, vol. 40, no. 7, pp. 3786–3801, 2011.

[10] K. S. Novoselov, A. K. Geim, S. V. Morozov, D. Jiang, Y. Zhang, S. V. Dubonos, I. V. Grigorieva, and A. A. Firsov, "Electric field effect in atomically thin carbon films," *Science*, vol. 306, no. 5696, pp. 666–669, 2004.

[11] K. Novoselov, A. Geim, S. Morozov, D. Jiang, M. Katsnelson, I. Grigorieva, S. Dubonos, and A. Firsov, "Two-dimensional gas of massless Dirac fermions in graphene," *Nature*, vol. 438, no. 7065, pp. 197–200, 2005.

[12] Y. Zhang, Y.-W. Tan, H. L. Stormer, and P. Kim, "Experimental observation of the quantum hall effect and Berry's phase in graphene," *Nature*, vol. 438, no. 7065, pp. 201–204, 2005.

[13] A. K. Geim, "Graphene: Status and prospects," *Science*, vol. 324, no. 5934, pp. 1530–1534, 2009.

[14] A. K. Geim and K. S. Novoselov, "The rise of graphene," *Nat. Mater.*, vol. 6, no. 3, pp. 183–191, 2007.

[15] A. H. C. Neto and K. Novoselov, "New directions in science and technology: two-dimensional crystals," *Rep. Prog. Phys.*, vol. 74, no. 8, p. 082501, 2011.

[16] K. S. Kim, Y. Zhao, H. Jang, S. Y. Lee, J. M. Kim, K. S. Kim, J.-H. Ahn, P. Kim, J.-Y. Choi, and B. H. Hong, "Large-scale pattern growth of graphene films for stretchable transparent electrodes," *Nature*, vol. 457, no. 7230, pp. 706–710, 2009.

[17] A. Reina, X. Jia, J. Ho, D. Nezich, H. Son, V. Bulovic, M. S. Dresselhaus, and J. Kong, "Large area, few-layer graphene films on arbitrary substrates by chemical vapor deposition," *Nano Lett.*, vol. 9, no. 1, pp. 30–35, 2009.

[18] X. Li, W. Cai, J. An, S. Kim, J. Nah, D. Yang, R. Piner, A. Velamakanni, I. Jung, E. Tutuc, S. K. Banerjee, L. Colombo, and R. S. Ruoff, "Large-area synthesis of high-quality and uniform graphene films on copper foils," *Science*, vol. 324, no. 5932, pp. 1312–1314, 2009.

[19] P. Sutter, M. S. Hybertsen, J. T. Sadowski, and E. Sutter, "Electronic structure of few-layer epitaxial graphene on Ru(0001)," *Nano Lett.*, vol. 9, no. 7, pp. 2654–2660, 2009.

[20] C. Berger, Z. Song, X. Li, X. Wu, N. Brown, C. Naud, D. Mayou, T. Li, J. Hass, A. N. Marchenkov, E. H. Conrad, P. N. First, and W. A. de Heer, "Electronic confinement and coherence in patterned epitaxial graphene," *Science*, vol. 312, no. 5777, pp. 1191–1196, 2006.

[21] L. Ci, Z. Xu, L. Wang, W. Gao, F. Ding, K. F. Kelly, B. I. Yakobson, and P. M. Ajayan, "Controlled nanocutting of graphene," *Nano Res.*, vol. 1, no. 2, pp. 116–122, 2008.

[22] Z. Chen, Y. . Lin, M. J. Rooks, and P. Avouris, "Graphene nano-ribbon electronics," *Phys. E*, vol. 40, no. 2, pp. 228–232, 2007.

[23] L. L. Song, X. H. Zheng, R. L. Wang, and Z. Zeng, "Dangling bond states, edge magnetism, and edge reconstruction in pristine and B/N-terminated zigzag graphene nanoribbons," *J. Phys. Chem. C*, vol. 114, no. 28, pp. 12145–12150, 2010.

[24] Y. Chen, B. Zhang, G. Liu, X. Zhuang, and E.-T. Kang, "Graphene and its derivatives: switching on and off," *Chem. Soc. Rev*, vol. 41, no. 13, pp. 4688–707, 2012.

[25] A. H. Castro Neto, F. Guinea, N. M. R. Peres, K. S. Novoselov, and A. K. Geim, "The electronic properties of graphene," *Rev. Mod. Phys.*, vol. 81, pp. 109–162, 2009.

[26] M. Y. Han, B. Özyilmaz, Y. Zhang, and P. Kim, "Energy band-gap engineering of graphene nanoribbons," *Phys. Rev. Lett.*, vol. 98, no. 20, p. 206805, 2007.

[27] N. M. R. Peres, A. H. C. Neto, and F. Guinea, "Spin-dependent electronic and magnetic properties of Co nanostructures on Pt(111) studied by spin-resolved scanning tunneling spectroscopy," *Phys. Rev. B*, vol. 73, p. 195411, 2006.

[28] X. R. Wang, Y. J. Ouyang, X. L. Li, H. L. Wang, J. Guo, and H. J. Dai, "Experimental verification of $\mathrm{PbBi_2Te_4}$ as a 3D topological insulator," *Phys. Rev. Lett.*, vol. 10, p. 206803, 2008.

[29] L. A. Ponomarenko, F. Schedin, M. I. Katsnelson, R. Yang, E. W. Hill, K. S. Novoselov, and A. K. Geim, "Chaotic dirac billiard in graphene quantum dots," *Science*, vol. 320, p. 356, 2008.

[30] Q. M. Yan, B. Huang, J. Yu, F. W. Zheng, J. Zang, J. Wu, B.-L. Gu, F. Liu, and

W. H. Duan, “Intrinsic currentvoltage characteristics of graphene nanoribbon transistors and effect of edge doping,” *Nano Lett.*, vol. 6, p. 1469, 2007.

[31] B. Standley, W. Z. Bao, H. Zhang, J. Bruck, C. N. Lau, and M. Bockrath, “Graphene-based atomic-scale switches,” *Nano Lett.*, vol. 10, p. 3345, 2008.

[32] L. G. Cançado, M. A. Pimenta, B. R. A. Neves, G. Medeiros-Ribeiro, T. Enoki, Y. Kobayashi, K. Takai, K. . Fukui, M. S. Dresselhaus, R. Saito, and A. Jorio, “Anisotropy of the raman spectra of nanographite ribbons,” *Phys. Rev. Lett.*, vol. 93, no. 4, pp. 047403–1, 2004.

[33] Y.-W. Son, M. L. Cohen, and S. G. Louie, “Energy gaps in graphene nanoribbons,” *Phys. Rev. Lett.*, vol. 97, no. 21, p. 216803, 2006.

[34] H. Park, J. A. Rowehl, K. K. Kim, V. Bulovic, and J. Kong, “Doped graphene electrodes for organic solar cells,” *Nanotechnology*, vol. 21, no. 50, p. 505204, 2010.

[35] X. Wang, L. Zhi, and K. Mullen, “Transparent, conductive graphene electrodes for dye-sensitized solar cells,” *Nano Lett.*, vol. 8, no. 1, pp. 323–327, 2008.

[36] P. Blake, P. D. Brimicombe, R. R. Nair, T. J. Booth, D. Jiang, F. Schedin, L. A. Ponomarenko, S. V. Morozov, H. F. Gleeson, E. W. Hill, A. K. Geim, and K. S. Novoselov, “Graphene-based liquid crystal device,” *Nano Lett.*, vol. 8, no. 6, pp. 1704–1708, 2008.

[37] S. Y. Jeong, S. H. Kim, J. T. Han, H. J. Jeong, S. Yang, and G.-W. Lee, “High-performance transparent conductive films using rheologically derived reduced graphene oxide,” *ACS Nano*, vol. 5, no. 2, pp. 870–878, 2011.

[38] X. Li, Y. Zhu, W. Cai, M. Borysiak, B. Han, D. Chen, R. D. Piner, L. Colombo, and R. S. Ruoff, "Transfer of large-area graphene films for high-performance transparent conductive electrodes," *Nano Lett.*, vol. 9, no. 12, pp. 4359–4363, 2009.

[39] S. Stankovich, D. A. Dikin, R. D. Piner, K. A. Kohlhaas, A. Kleinhammes, Y. Jia, Y. Wu, S. T. Nguyen, and R. S. Ruoff, "Synthesis of graphene-based nanosheets via chemical reduction of exfoliated graphite oxide," *Carbon*, vol. 45, no. 7, pp. 1558 – 1565, 2007.

[40] D. A. Dikin, S. Stankovich, E. J. Zimney, R. D. Piner, G. H. B. Dommett, G. Evmenenko, S. T. Nguyen, and R. S. Ruoff, "Preparation and characterization of graphene oxide paper," *Nature*, vol. 448, no. 7152, pp. 457–460, 2007.

[41] H. C. Schniepp, J.-L. Li, M. J. McAllister, H. Sai, M. Herrera-Alonso, D. H. Adamson, R. K. Prud'homme, R. Car, D. A. Saville, and I. A. Aksay, "Functionalized single graphene sheets derived from splitting graphite oxide," *J. Phys. Chem. B*, vol. 110, no. 17, pp. 8535–8539, 2006.

[42] V. C. Tung, M. J. Allen, Y. Yang, and R. B. Kaner, "High-throughput solution processing of large-scale graphene," *Nat. Nanotechnol.*, vol. 4, no. 1, pp. 25–29, 2009.

[43] P. G. Ren, D. X. Yan, X. Ji, T. Chen, and Z. M. Li, "Temperature dependence of graphene oxide reduced by hydrazine hydrate," *Nanotechnology*, vol. 22, no. 5, p. 055705, 2011.

[44] I. Jung, D. A. Dikin, R. D. Piner, and R. S. Ruoff, "Tunable electrical con-

ductivity of individual graphene oxide sheets reduced at “low” temperatures,” *Nano Lett.*, vol. 8, no. 12, pp. 4283–4287, 2008.

[45] S. Gilje, S. Han, M. Wang, K. L. Wang, and R. B. Kaner, “A chemical route to graphene for device applications,” *Nano Lett.*, vol. 7, no. 11, pp. 3394–3398, 2007.

[46] C. Gómez-Navarro, R. T. Weitz, A. M. Bittner, M. Scolari, A. Mews, M. Burghard, and K. Kern, “Electronic transport properties of individual chemically reduced graphene oxide sheets,” *Nano Lett.*, vol. 7, no. 11, pp. 3499–3503, 2007.

[47] V. López, R. S. Sundaram, C. Gómez-Navarro, D. Olea, M. Burghard, J. Gómez-Herrero, F. Zamora, and K. Kern, “Chemical vapor deposition repair of graphene oxide: A route to highly-conductive graphene monolayers,” *Adv. Mater.*, vol. 21, no. 46, pp. 4683–4686, 2009.

[48] C. Gómez-Navarro, J. C. Meyer, R. S. Sundaram, A. Chuvilin, S. Kurasch, M. Burghard, K. Kern, and U. Kaiser, “Atomic structure of reduced graphene oxide,” *Nano Lett.*, vol. 10, no. 4, pp. 1144–1148, 2010.

[49] L. Guo, R. Shao, Y. Zhang, H. Jiang, X. Li, S. Xie, B. Xu, Q. Chen, J. Song, and H. Sun, “Bandgap tailoring and synchronous microdevices patterning of graphene oxides,” *J. Phys. Chem. C*, 2012.

[50] M. Ezawa, “Peculiar width dependence of the electronic properties of carbon nanoribbons,” *Phys. Rev. B*, vol. 73, no. 4, pp. 1–8, 2006.

[51] M. Ezawa, “Graphene nanoribbon and graphene nanodisk,” *Phys. E*, vol. 40, no. 5, pp. 1421–1423, 2008.

[52] M. Ezawa, "Metallic graphene nanodisks: Electronic and magnetic properties," *Phys. Rev. B*, vol. 76, no. 24, p. 245415, 2007.

[53] M. Zhou, Y. Wang, Y. Zhai, J. Zhai, W. Ren, F. Wang, and S. Dong, "Controlled synthesis of large-area and patterned electrochemically reduced graphene oxide films," *Chem. Eur. J.*, vol. 15, no. 25, pp. 6116–6120, 2009.

[54] P. Solís-Fernández, J. I. Paredes, S. Villar-Rodil, L. Guardia, M. J. Fernández-Merino, G. Dobrik, L. P. Biró, A. Martínez-Alonso, and J. M. D. Tascón, "Global and local oxidation behavior of reduced graphene oxide," *J. Phys. Chem. C*, vol. 115, no. 16, pp. 7956–7966, 2011.

[55] L. Zhang, S. Diao, Y. Nie, K. Yan, N. Liu, B. Dai, Q. Xie, A. Reina, J. Kong, and Z. Liu, "Photocatalytic patterning and modification of graphene," *J. Am. Chem. Soc.*, vol. 133, no. 8, pp. 2706–2713, 2011.

[56] J. L. Li, K. N. Kudin, M. J. McAllister, R. K. Prud'homme, I. A. Aksay, and R. Car, "Oxygen-driven unzipping of graphitic materials," *Phys. Rev. Lett.*, vol. 96, no. 17, p. 176101, 2006.

[57] X. Z. Zhou, G. Lu, X. Y. Qi, S. X. Wu, H. Li, F. Boey, and H. Zhang, "A method for fabrication of graphene oxide nanoribbons from graphene oxide wrinkles," *J. Phys. Chem. C*, vol. 113, no. 44, pp. 19119–19122, 2009.

[58] S. Fujii and T. Enoki, "Cutting of oxidized graphene into nanosized pieces," *J. Am. Chem. Soc.*, vol. 132, no. 29, pp. 10034–10041, 2010.

[59] A. V. Talyzin, I. V. Anoshkin, A. V. Krasheninnikov, R. M. Nieminen, A. G. Nasibulin, H. Jiang, and E. I. Kauppinen, "Synthesis of graphene nanoribbons

encapsulated in single-walled carbon nanotubes," *Nano Lett.*, vol. 11, no. 10, pp. 4352–4356, 2011.

[60] Y.-C. Chen, D. G. de Oteyza, Z. Pedramrazi, C. Chen, F. R. Fischer, and M. F. Crommie, "Tuning the band gap of graphene nanoribbons synthesized from molecular precursors," *ACS Nano*, vol. 7, no. 7, pp. 6123–6128, 2013.

[61] K. S. Kim, Y. Zhao, H. Jang, S. Y. Lee, J. M. Kim, K. S. Kim, J.-H. Ahn, P. Kim, J.-Y. Choi, and B. H. Hong, "Large-scale pattern growth of graphene films for stretchable transparent electrodes," *Nature*, vol. 457, no. 7230, pp. 706–710, 2009.

[62] H. W. Kroto, J. R. Heath, S. C. O'Brien, R. F. Curl, and R. E. Smalley, "C_{60}: Buckminsterfullerene," *Nature*, vol. 318, no. 6042, pp. 162–163, 1985.

[63] S. Iijima, "Helical microtubules of graphitic carbon," *Nature*, vol. 354, no. 6348, pp. 56–58, 1991.

[64] R. Saito, M. Fujita, G. Dresselhaus, and M. S. Dresselhaus, "Electronic structure of graphene tubules based on C_{60}," *Phys. Rev. B*, vol. 46, pp. 1804–1811, 1992.

[65] N. Hamada, S.-i. Sawada, and A. Oshiyama, "New one-dimensional conductors: Graphitic microtubules," *Phys. Rev. Lett.*, vol. 68, pp. 1579–1581, 1992.

[66] R. Hoffmann, *Solids and Surfaces: A Chemist's View of Bonding in Extended Structures.* Wiley-VCH, 1 ed., 1989.

[67] T. A. Albright, J. K. Burdett, and M.-H. Whangbo, *Orbital Interactions in Chemistry.* Wiley, 1985.

[68] N. T. Anh, *Frontier Orbitals: A Practical Manual.* Wiley, 1 ed., 2007.

[69] J. K. Burdett, *Chemical Bonding in Solids.* Oxford University Press, USA, 1995.

[70] D. Kienle, J. I. Cerda, and A. W. Ghosh, "Extended Hückel theory for band structure, chemistry, and transport. I. carbon nanotubes," *Journal of Applied Physics*, vol. 100, no. 4, pp. –, 2006.

[71] R. Hoffmann, "An extended Hückel theory. I. hydrocarbons," *The Journal of Chemical Physics*, vol. 39, no. 6, pp. 1397–1412, 1963.

[72] C. A. Coulson, "The electronic structure of some polyenes and aromatic molecules. VII. Bonds of fractional order by the molecular orbital method," *Proc. R. Soc. Lond.*, vol. 169, no. 938, pp. 413–428, 1939.

[73] C. A. Coulson and H. C. Longuet-Higgins, "The electronic structure of conjugated systems. II. Unsaturated hydrocarbons and their hetero-derivatives," *Proc. R. Soc. Lond.*, vol. 192, no. 1028, pp. 16–32, 1947.

[74] C. A. Coulson, "The electronic structure of some polyenes and aromatic molecules. IV. The nature of the links of certain free radicals," *Proc. R. Soc. Lond.*, vol. 164, no. 918, pp. 383–396, 1938.

[75] J. K. Burdett, "From bonds to bands and molecules to solids," *Prog. Solid State Chem.*, vol. 15, no. 3, pp. 173 – 255, 1984.

[76] B. C. Gerstein, "Chemistry, bands, bonds, and solids. a translator's notes," *J. Chem. Educ.*, vol. 50, no. 5, p. 316, 1973.

[77] R. Shankar, *Principles of Quantum Mechanics.* New York: Plenum Press, 1994.

[78] F. Jensen, *Introduction to Computational Chemistry.* Chichester, England; Hoboken, NJ: John Wiley & Sons, 2007.

[79] I. N. Levine, *Quantum Chemistry.* Upper Saddle River, N.J.: Pearson Prentice Hall, 2009.

[80] R. G. Parr and Y. , *Density-Functional Theory of Atoms and Molecules.* New York; Oxford [England]: Oxford University Press ; Clarendon Press, 1989.

[81] W. Koch and M. C. Holthausen, *A Chemist's Guide to Density Functional Theory, 2nd Edition.* Wiley-VCH, 2 ed., 2001.

[82] D. Sholl and J. A. Steckel, *Density Functional Theory: A Practical Introduction.* Wiley-Interscience, 1 edition ed., 2011.

[83] P. Hohenberg and W. Kohn, "Inhomogeneous electron gas," *Phys. Rev.*, vol. 136, pp. B864–B871, 1964.

[84] W. Kohn and L. J. Sham, "Self-consistent equations including exchange and correlation effects," *Phys. Rev.*, vol. 140, pp. A1133–A1138, 1965.

[85] K. Capelle, "A bird's-eye view of density-functional theory," *Braz. J. Phys.*, vol. 36, pp. 1318 – 1343, 2006.

[86] J. Hafner, "Ab-initio simulations of materials using VASP: Density-functional theory and beyond," *J. Comput. Chem.*, vol. 29, no. 13, pp. 2044–2078, 2008.

[87] M. Wang and C. M. Li, "Excitonic properties of graphene-based materials," *Nanoscale*, vol. 4, pp. 1044–1050, 2012.

[88] D. W. Boukhvalov, "DFT modeling of the covalent functionalization of graphene: from ideal to realistic models," *R. Soc. Chem. Adv.*, vol. 3, pp. 7150–7159, 2013.

[89] K. Burke, "Perspective on density functional theory," *J. Chem. Phys.*, vol. 136, no. 15, pp. –, 2012.

[90] J. Guan, P. Duffy, J. Carter, D. Chong, K. Casida, M. Casida, and M. Wrinn, "Comparison of local-density and Hartree-Fock calculations of molecular polarizabilities and hyperpolarizabilities," *J. Chem. Phys.*, vol. 98, no. 6, pp. 4753–4765, 1993.

[91] R. Godby, M. Schlüter, and L. Sham, "Self-energy operators and exchange-correlation potentials in semiconductors," *Phys. Rev. B*, vol. 37, no. 17, pp. 10159–10175, 1988.

[92] E. Chulkov, V. Silkin, and P. Echenique, "Image potential states on metal surfaces: Binding energies and wave functions," *Surf. Sci.*, vol. 437, no. 3, pp. 330–352, 1999.

[93] J. P. Perdew, "Density-functional approximation for the correlation energy of the inhomogeneous electron gas," *Phys. Rev. B*, vol. 33, pp. 8822–8824, 1986.

[94] J. P. Perdew, K. Burke, and M. Ernzerhof, "Generalized gradient approximation made simple," *Phys. Rev. Lett.*, vol. 77, pp. 3865–3868, 1996.

[95] J. P. Perdew, K. Burke, and M. Ernzerhof, "Generalized gradient approximation made simple [phys. rev. lett. 77, 3865 (1996)]," *Phys. Rev. Lett.*, vol. 78, pp. 1396–1396, 1997.

[96] G. Kresse and J. Hafner, “Ab initio molecular dynamics for liquid metals,” *Phys. Rev. B*, vol. 47, no. 1, pp. 558–561, 1993.

[97] G. Kresse and J. Furthmüller, “Efficient iterative schemes for ab initio total-energy calculations using a plane-wave basis set,” *Phys. Rev. B*, vol. 54, no. 16, pp. 11169–11186, 1996.

[98] G. Kresse and J. Furthmüller, “Efficiency of ab-initio total energy calculations for metals and semiconductors using a plane-wave basis set,” *Comput. Mater. Sci.*, vol. 6, no. 1, pp. 15–50, 1996.

[99] J. Paier, R. Hirschl, M. Marsman, and G. Kresse, “The Perdew–Burke–Ernzerhof exchange-correlation functional applied to the G2-1 test set using a plane-wave basis set,” *J. Chem. Phys.*, vol. 122, no. 23, pp. –, 2005.

[100] S. Grimme, “Semiempirical GGA-type density functional constructed with a long-range dispersion correction,” *J. Comput. Chem.*, vol. 27, no. 15, pp. 1787–1799, 2006.

[101] J. Neugebauer and M. Scheffler, “Adsorbate-substrate and adsorbate-adsorbate interactions of Na and K adlayers on Al(111),” *Phys. Rev. B*, vol. 46, pp. 16067–16080, 1992.

[102] R. D. King-Smith and D. Vanderbilt, “Theory of polarization of crystalline solids,” *Phys. Rev. B*, vol. 47, pp. 1651–1654, 1993.

[103] D. Vanderbilt and R. D. King-Smith, “Electric polarization as a bulk quantity and its relation to surface charge,” *Phys. Rev. B*, vol. 48, pp. 4442–4455, 1993.

[104] R. Resta, “Theory of the electric polarization in crystals,” *Ferroelectrics*, vol. 136, no. 1, pp. 51–55, 1992.

[105] R. Resta, “Macroscopic polarization in crystalline dielectrics: the geometric phase approach,” *Rev. Mod. Phys.*, vol. 66, pp. 899–915, 1994.

[106] R. W. Nunes and X. Gonze, “Berry-phase treatment of the homogeneous electric field perturbation in insulators,” *Phys. Rev. B*, vol. 63, p. 155107, 2001.

[107] C. Kittel, *Introduction to Solid State Physics.* NY: Wiley, 8 ed., 2005.

[108] E. Kaxiras, *Atomic and Electronic Structure of Solids.* Cambridge, UK; New York: Cambridge University Press, 2003.

[109] R. M. Martin, *Electronic Structure: Basic Theory and Practical Methods.* Cambridge, UK; New York: Cambridge University Press, 2004.

[110] J. Kohanoff, *Electronic Structure Calculations for Solids and Molecules: Theory and Computational Methods.* Cambridge: Cambridge University Press, 2006.

[111] H. J. Monkhorst and J. D. Pack, “Special points for Brillouin-zone integrations,” *Phys. Rev. B*, vol. 13, pp. 5188–5192, 1976.

[112] A. H. MacDonald, “Comment on special points for Brillouin-zone integrations,” *Phys. Rev. B*, vol. 18, pp. 5897–5899, 1978.

[113] J. H. Warner, G.-D. Lee, K. He, A. W. Robertson, E. Yoon, and A. I. Kirkland, “Bond length and charge density variations within extended arm chair defects in graphene,” *ACS Nano*, vol. 7, no. 11, pp. 9860–9866, 2013.

[114] P. E. Blöchl, “Projector augmented-wave method,” *Phys. Rev. B*, vol. 50, no. 24, pp. 17953–17979, 1994.

[115] G. Kresse and D. Joubert, “From ultrasoft pseudopotentials to the projector augmented-wave method,” *Phys. Rev. B*, vol. 59, no. 3, pp. 1758–1775, 1999.

[116] T. Enoki and T. Ando, *Physics and Chemistry of Graphene: Graphene to Nanographene*. Oxford [u.a.]: Pan Stanford Publ., 2009.

[117] O. Hod, V. Barone, and G. E. Scuseria, “Half-metallic grapheme nanodots: A comprehensive first-principles theoretical study,” *Phys.Rev.B*, vol. 77, no. 3, p. 035411, 2008.

[118] E. Rudberg, P. Sałek, and Y. Luo, “Nonlocal exchange interaction removes half-metallicity in graphene nanoribbons,” *Nano Lett.*, vol. 7, no. 8, pp. 2211–2213, 2007.

[119] Y. . Son, M. L. Cohen, and S. G. Louie, “Half-metallic graphene nanoribbons,” *Nature*, vol. 444, no. 7117, pp. 347–349, 2006.

[120] A. Konishi, Y. Hirao, K. Matsumoto, H. Kurata, R. Kishi, Y. Shigeta, M. Nakano, K. Tokunaga, K. Kamada, and T. Kubo, “Synthesis and characterization of quarteranthene: Elucidating the characteristics of the edge state of graphene nanoribbons at the molecular level,” *J. Am. Chem. Soc.*, vol. 135, no. 4, pp. 1430–1437, 2013.

[121] H. Park, J. Y. Lee, and S. Shin, “Tuning of the band structures of zigzag graphene nanoribbons by an electric field and adsorption of pyridine and BF_3: A DFT study,” *J. Phys. Chem. C*, vol. 116, no. 37, pp. 20054–20061, 2012.

[122] H. Lee, Y. . Son, N. Park, S. Han, and J. Yu, “Magnetic ordering at the edges of graphitic fragments: Magnetic tail interactions between the edge-localized states,” *Phys. Rev. B*, vol. 72, p. 174431, 2005.

[123] W. Y. Kim and K. S. Kim, “Prediction of very large values of magnetoresistance in a graphene nanoribbon device,” *Nat. Nanotechnol.*, vol. 3, no. 7, pp. 408–412, 2008.

[124] O. V. Yazyev and M. I. Katsnelson, “Magnetic correlations at graphene edges: Basis for novel spintronics devices,” *Phys. Rev. Lett.*, vol. 100, p. 047209, 2008.

[125] P. Lou and J. Y. Lee, “Band structures of narrow zigzag silicon carbon nanoribbons,” *J. Phys. Chem. C*, vol. 113, no. 29, pp. 12637–12640, 2009.

[126] P. Lou and J. Y. Lee, “Spin controlling in narrow zigzag silicon carbon nanoribbons by carrier doping,” *J. Phys. Chem. C*, vol. 114, no. 24, pp. 10947–10951, 2010.

[127] P. Lou and J. Y. Lee, “Electrical control of magnetization in narrow zigzag silicon carbon nanoribbons,” *J. Phys. Chem. C*, vol. 113, no. 50, pp. 21213–21217, 2009.

[128] S. Okada and A. Oshiyama, “Magnetic ordering in hexagonally bonded sheets with first-row elements,” *Phys. Rev. Lett.*, vol. 87, p. 146803, 2001.

[129] E. J. Kan, Z. Li, J. Yang, and J. Hou, “Will zigzag graphene nanoribbon turn to half metal under electric field?,” *Appl. Phys. Lett.*, vol. 91, p. 243116, 2007.

[130] E. J. Kan, Z. Li, J. Yang, and J. G. Hou, “Half-metallicity in edge-modified

zigzag graphene nanoribbons," *J. Am. Chem. Soc.*, vol. 130, no. 13, pp. 4224–4225, 2008.

[131] E.-J. Kan, X. Wu, Z. Li, X. C. Zeng, J. Yang, and J. G. Hou, "Half-metallicity in hybrid BCN nanoribbons," *J. Chem. Phys.*, vol. 129, no. 8, p. 084712, 2008.

[132] D. Gunlycke, J. Li, J. W. Mintmire, and C. T. White, "Altering low-bias transport in zigzag-edge graphene nanostrips with edge chemistry," *Appl. Phys. Lett.*, vol. 91, no. 11, pp. –, 2007.

[133] F. Cervantes-Sodi, G. Csányi, S. Piscanec, and A. C. Ferrari, "Electronic properties of chemically modified graphene ribbons," *Phys. Status Solidi B*, vol. 245, no. 10, pp. 2068–2071, 2008.

[134] Y. Ding, X. Yang, and J. Ni, "Electronic structures of boron nanoribbons," *Appl. Phys. Lett.*, vol. 93, no. 4, pp. –, 2008.

[135] T. B. Martins, A. J. R. da Silva, R. H. Miwa, and A. Fazzio, "σ- and π-defects at graphene nanoribbon edges: Building spin filters," *Nano Lett.*, vol. 8, no. 8, pp. 2293–2298, 2008.

[136] R. G. A. Veiga, R. H. Miwa, and G. P. Srivastava, "Quenching of local magnetic moment in oxygen adsorbed graphene nanoribbons," *J. Chem. Phys.*, vol. 128, no. 20, pp. –, 2008.

[137] Y. Li, Z. Zhou, P. Shen, and Z. Chen, "Spin gapless semiconductor-metal-half-metal properties in nitrogen-doped zigzag graphene nanoribbons," *ACS Nano*, vol. 3, no. 7, pp. 1952–1958, 2009.

[138] C. Uthaisar, V. Barone, and J. E. Peralta, "Lithium adsorption on zigzag graphene nanoribbons," *J. Appl. Phys.*, vol. 106, no. 11, pp. –, 2009.

[139] R. Miwa, R. Veiga, and G. Srivastava, "Structural, electronic, and magnetic properties of pristine and oxygen-adsorbed graphene nanoribbons," *Appl. Surf. Sci.*, vol. 256, no. 19, pp. 5776 – 5782, 2010.

[140] D. Krepel and O. Hod, "Lithium adsorption on armchair graphene nanoribbons," *Surf. Sci.*, vol. 605, no. 17-18, pp. 1633–1642, 2011.

[141] Y.-L. Lee, S. Kim, C. Park, J. Ihm, and Y.-W. Son, "Controlling half-metallicity of graphene nanoribbons by using a ferroelectric polymer," *ACS Nano*, vol. 4, no. 3, pp. 1345–1350, 2010.

[142] J. P. Perdew, K. Burke, and Y. Wang, "Generalized gradient approximation for the exchange-correlation hole of a many-electron system," *Phys. Rev. B*, vol. 54, no. 23, pp. 16533–16539, 1996.

[143] E. Voloshina, D. Mollenhauer, L. Chiappisi, and B. Paulus, "Theoretical study on the adsorption of pyridine derivatives on graphene," *Chem. Phys. Lett.*, vol. 510, no. 4–6, pp. 220 – 223, 2011.

[144] V. Q. Nguyen and F. Tureček, "Gas-phase protonation of pyridine. a variable-time neutralization–reionization and ab initio study of pyridinium radicals," *J. Mass Spectrom.*, vol. 32, no. 1, pp. 55–63, 1997.

[145] G. Maas, H. M. Weber, R. Exner, and J. Salbeck, "N-carbeniopyridinium salts: Charge-transfer complexes with the $\mathrm{C_5(COOMe)_5}$ anion; C−C bond formation with the TCNQ radical anion," *J. Phys. Org. Chem.*, vol. 3, no. 7, pp. 459–469, 1990.

[146] J. B. Neaton, M. S. Hybertsen, and S. G. Louie, “Renormalization of molecular electronic levels at metal-molecule interfaces,” *Phys. Rev. Lett.*, vol. 97, p. 216405, 2006.

[147] C. Freysoldt, P. Rinke, and M. Scheffler, “Controlling polarization at insulating surfaces: Quasiparticle calculations for molecules adsorbed on insulator films,” *Phys. Rev. Lett.*, vol. 103, p. 056803, 2009.

[148] L. Yang, C.-H. Park, Y.-W. Son, M. L. Cohen, and S. G. Louie, “Quasiparticle energies and band gaps in graphene nanoribbons,” *Phys. Rev. Lett.*, vol. 99, p. 186801, 2007.

[149] K. S. Thygesen and A. Rubio, “Renormalization of molecular quasiparticle levels at metal-molecule interfaces: Trends across binding regimes,” *Phys. Rev. Lett.*, vol. 102, p. 046802, 2009.

[150] G. Henkelman, A. Arnaldsson, and H. Jónsson, “A fast and robust algorithm for Bader decomposition of charge density,” *Comput. Mater. Sci.*, vol. 36, no. 3, pp. 354 – 360, 2006.

[151] E. Sanville, S. D. Kenny, R. Smith, and G. Henkelman, “Improved grid-based algorithm for Bader charge allocation,” *J. Comput. Chem.*, vol. 28, no. 5, pp. 899–908, 2007.

[152] W. Tang, E. Sanville, and G. Henkelman, “A grid-based Bader analysis algorithm without lattice bias,” *J. Phys.: Condes. Matter.*, vol. 21, no. 8, p. 084204, 2009.

[153] K. S. Novoselov, A. K. Geim, S. V. Morozov, D. Jiang, M. I. Katsnelson, I. V.

Grigorieva, S. V. Dubonos, and A. A. Firsov, “Two-dimensional gas of massless Dirac fermions in graphene,” *Nature*, vol. 438, no. 7065, pp. 197–200, 2005.

[154] S. Bhandary, O. Eriksson, B. Sanyal, and M. I. Katsnelson, “Complex edge effects in zigzag graphene nanoribbons due to hydrogen loading,” *Phys. Rev. B*, vol. 82, p. 165405, 2010.

[155] B. Xu, J. Yin, Y. D. Xia, X. G. Wan, K. Jiang, and Z. G. Liu, “Electronic and magnetic properties of zigzag graphene nanoribbon with one edge saturated,” *Appl. Phys. Lett.*, vol. 96, no. 16, p. 163102, 2010.

[156] H. Lee, M. L. Cohen, and S. G. Louie, “Selective functionalization of halogens on zigzag graphene nanoribbons: A route to the separation of zigzag graphene nanoribbons,” *Appl. Phys. Lett.*, vol. 97, no. 23, p. 233101, 2010.

[157] K. Wakabayashi, M. Fujita, H. Ajiki, and M. Sigrist, “Electronic and magnetic properties of nanographite ribbons,” *Phys. Rev. B*, vol. 59, no. 12, pp. 8271–8282, 1999.

[158] V. Barone, O. Hod, and G. E. Scuseria, “Electronic structure and stability of semiconducting graphene nanoribbons,” *Nano Lett.*, vol. 6, no. 12, pp. 2748–2754, 2006.

[159] K. N. Kudin, “Zigzag graphene nanoribbons with saturated edges,” *ACS Nano*, vol. 2, no. 3, pp. 516–522, 2008.

[160] O. Hod, V. Barone, J. E. Peralta, and G. E. Scuseria, “Enhanced half-metallicity in edge-oxidized zigzag graphene nanoribbons,” *Nano Lett.*, vol. 7, no. 8, pp. 2295–2299, 2007.

[161] Y. Wang, C. Cao, and H.-P. Cheng, "Metal-terminated graphene nanoribbons," *Phys. Rev. B*, vol. 82, p. 205429, 2010.

[162] C. Archambault and A. Rochefort, "States modulation in graphene nanoribbons through metal contacts," *ACS Nano*, vol. 7, no. 6, pp. 5414–5420, 2013.

[163] B. M. Wong, S. H. Ye, and G. O'Bryan, "Reversible, opto-mechanically induced spin-switching in a nanoribbon-spiropyran hybrid material," *Nanoscale*, vol. 4, pp. 1321–1327, 2012.

[164] P. Zhang, K. Jiang, C. Ye, and Y. Zhao, "Facile synthesis of V-shaped copolymer brushes grafted onto the surface of graphene oxide via coupling reactions," *Chem. Commun.*, vol. 47, pp. 9504–9506, 2011.

[165] Y. Deng, Y. Li, J. Dai, M. Lang, and X. Huang, "Functionalization of graphene oxide towards thermo-sensitive nanocomposites via moderate in situ SET-LRP," *J. Polym. Sci., Part A: Polym. Chem.*, vol. 49, no. 22, pp. 4747–4755, 2011.

[166] Z. Li, W. Zhang, Y. Luo, J. Yang, and J. G. Hou, "How graphene is cut upon oxidation?," *J. Am. Chem. Soc.*, vol. 131, no. 18, pp. 6320–6321, 2009.

[167] S. Lu, S. Li, J. Yu, Z. Yuan, and B. Qi, "Epoxy nanocomposites filled with thermotropic liquid crystalline epoxy grafted graphene oxide," *R. Soc. Chem. Adv.*, vol. 3, no. 23, pp. 8915–8923, 2013.

[168] K. Ai, Y. Liu, L. Lu, X. Cheng, and L. Huo, "A novel strategy for making soluble reduced graphene oxide sheets cheaply by adopting an endogenous reducing agent," *J. Mater. Chem.*, vol. 21, pp. 3365–3370, 2011.

[169] B. Narayanan, S. L. Weeks, B. N. Jariwala, B. Macco, J.-W. Weber, S. J. Rathi, M. C. M. van de Sanden, P. Sutter, S. Agarwal, and C. V. Ciobanu, “Carbon monoxide-induced reduction and healing of graphene oxide,” *J. Vac. Sci. Technol. A*, vol. 31, no. 4, pp. –, 2013.

[170] S. Paul, E. E. Santiso, and M. B. Nardelli, “Sequestration and selective oxidation of carbon monoxide on graphene edges,” *J. Phys.: Condes. Matter.*, vol. 21, no. 35, p. 355008, 2009.

[171] A. Pulido, P. Concepcion, M. Boronat, C. Botas, P. Alvarez, R. Menendez, and A. Corma, “Reconstruction of the carbon sp2 network in graphene oxide by low-temperature reaction with co,” *J. Mater. Chem.*, vol. 22, pp. 51–56, 2012.

[172] H. Liu and J. Y. Lee, “Electric field effects on the adsorption of CO on a graphene nanodot and the healing mechanism of a vacancy in a graphene nanodot,” *J. Phys. Chem. C*, vol. 116, no. 4, pp. 3034–3041, 2012.

[173] H. Liu and J. Y. Lee, “Electric field assisted oxygen removal from the basal plane of the graphitic material,” *J. Comput. Chem.*, vol. 34, no. 4, pp. 305–310, 2013.

[174] D. V. Kosynkin, A. L. Higginbotham, A. Sinitskii, J. R. Lomeda, A. Dimiev, B. K. Price, and J. M. Tour, “Longitudinal unzipping of carbon nanotubes to form graphene nanoribbons,” *Nature*, vol. 458, no. 7240, pp. 872–876, 2009.

[175] T. Sun and S. Fabris, “Mechanisms for oxidative unzipping and cutting of graphene,” *Nano Lett.*, vol. 12, no. 1, pp. 17–21, 2011.

[176] O. Leenaerts, B. Partoens, and F. M. Peeters, “Adsorption of H_2O, NH_3, CO,

NO_2, and NO on graphene: A first-principles study," *Phys. Rev. B*, vol. 77, p. 125416, 2008.

[177] X. Lin, J. Ni, and C. Fang, "Adsorption capacity of H_2O, NH_3, CO, and NO_2 on the pristine graphene," *J. Appl. Phys.*, vol. 113, no. 3, pp. –, 2013.

[178] Y. Peng and J. Li, "Ammonia adsorption on graphene and graphene oxide: a first-principles study," *Front. Environ. Sci. Eng.*, vol. 7, no. 3, pp. 403–411, 2013.

[179] A. Mathkar, D. Tozier, P. Cox, P. Ong, C. Galande, K. Balakrishnan, A. Leela Mohana Reddy, and P. M. Ajayan, "Controlled, stepwise reduction and band gap manipulation of graphene oxide," *J. Phys. Chem. Lett.*, vol. 3, no. 8, pp. 986–991, 2012.

국문초록

이 논문에서, 우리는 그래핀 나노리본에 대하여 이론연구와 계산연구를 했다. 그래핀 나노리본의 전자 구조는 그래핀의 전자구조와 다르다. 가장자리 구조가 만들어지면서 그래핀의 탄소 원자들 간의 공유결합 구조가 깨지기 때문에 이차원 구조에서 일차원 구조로 변한다. 띠간격이 없던 그래핀의 전자 구조는 그래핀 이차원 구조의 대칭성이 깨지면서, 그래핀 나노리본의 띠간격은 생기고 벌어진다. 그리고 한 쪽의 가장자리에 하나의 스핀 상태가 국한되어 양쪽의 상태는 나노리본의 너비에 의해 공간적으로 떨어져있을 뿐만 아니라 양쪽 모서리에 국한되어서 이곳 전자의 스핀 상태가 서로 다르다. 우리는 제일원리를 이용하여 화학적으로 수정된 그래핀 나노리본의 모형계를 만들어 전자구조와 화학반응을 연구했다. 그래핀 나노리본 위에 흡착된 분자의 영향에 의한 전자구조를 연구하면서 이와함께 전기장에 가해졌을 때 달라지는 특성들도 살펴보았다.

제 1 장에서는, 그래핀과 그패핀 나노리본이 갖는 전자띠 구조의 특징을 소개했다. 주기적 경계 조건 안에서 페르미 에너지 근처의 전자띠 구조가 어떻게 변하는지를 이해하기 위해서, 오비탈의 상 변화와 파수 벡터의 관계를 논하면서 원자가 실공간에서 위치한 배열과 그에 따라서 역공간에서 나타나는 전자띠 구조의 상관관계를 설명하였다. 우리는 또한 그래핀 합성과 관련된 실험들을 소개하고 그래핀과 그래핀 나노리본의 파생물의 성질을 살펴보았다. 이전의 연구들은 다양한 방법으로 접근하면서, 특정 성질을 갖는 그래핀 나노리본을 합성하는 일은 많은 노력이 필요하다는 것을 보여준다. 제 2 장에서, 우리가 주로 사용한 계산 방법인 밀도 범함수 이론에 대해 하트리·폭 방법과 비교하며 설명했다. 확장된 계에서, 평면파동 파동함수를 이용한 밀도 범함수 이론 계산 뿐만 아니라 k 점 표본 추출에 관하여 논했다.

제 3 장에서, PBE (Perdew-Burke-Ernzerhof) 범함수를 이용한 밀도 범함수 이론 방법으로 깨끗한 그래핀 나노리본의 특성를 얻는 과정을 설명하면서 다른 연구결과와 비교했다. 이렇게 얻은 깨끗한 그래핀 나노리본의 특성들은 화학적으로 조정된 그래핀 나노리본의 전자띠 구조와 비교하기 위한 기준이 되었다. 지그재그 가장자리 구조를 갖는 그래핀 나노리본은 재료 연구 분야에서 많은 관심을 받고있다. 왜냐하면, 지그재그 그래핀 나노리본의 특이한 전자적, 자기적 특성으로 실현 가능한 미래 장치의 재료로 각광을 받고 있기 때문이다. 이 지그재그 그래핀 나노리본은 작은 분자들의 정렬이나 전기장에 영향을 받아서 전자띠 구조가 바뀔 수 있다. 제 4 장에서, 피리딘의 흡착과 적용된 전기장이 전자띠 구조와 금속성에 주는 영향을 밀도 범함수 이론 벙법으로 다루며 연구한 내용을 소개했다. 피리딘과 그래핀 나노리본 사이의 공유결합 배위에 따라서 반도체 성질을 갖던 지그재그 그래핀 나노리본이 반쪽 금속 성질을 갖거나 반도체 성질을 그대로 유지되는 것을 관찰했다. 게다가, 두 α와 β 스핀 상태의 띠 간격이 비공유결합으로 각각 조정 되었다. 이 효과는 다른 나머지 가장자리에 BF_3를 피리딘과 함께 올려놓으면서 향상됐다. 전기장 역시 전기장 세기에 따라서 그래핀 나노리본이 반쪽 금속성이 되거나 반도체가 되도록 단위화 할 수 있었다. 이러한 특징들은 그래핀 면 위에서 흡착된 분자의 배열 모양에 따라서 나노 크기의 전자 장치를 조정할 수 있다는 것을 보여준다.

산화된 지그재그 그래핀 나노리본에서 벌집 모양의 그래핀 구조를 망가뜨리지 않고 에폭사이드를 제거하기 위해서는 많은 노력이 필요하다. 제 5 장에서, 우리는 좁은 지그재그 그래핀 나노리본의 중간에 있는 에폭사이드가 제거되는 반응 과정을 연구한 결과에 대해 논했다. 그래핀 나노리본의 너비에 따라서 에폭사이드의 이동과 제거 반응의 퍼텐셜 장벽의 높이가 달라져서 두 반응이 경쟁적 경로라는 것을 밝혔다. 그리고 두 반응 과정 모두, 그래핀 나노리본 평면에 수직 방향으로 전기장을 가하면 퍼텐셜 장벽의 높이가 낮아지는 것을 관찰했다. 우리는 이 연구를 하면서 그래핀의 한 부분에 국한된 화학 반응이나 전기장으로 그래핀 나노리본 파생물을

만들어서 깨끗한 그래핀 나노리본의 전자구조와 다른 조정된 전자구조를 관찰했다. 귀한 기능을 갖은 분자계를 설계하기위해, 이 결과들을 토대로 그 의미에 대하여 제 6 장에서 논하였다.

주요어: 그래핀, 나노리본, 지그재그 가장자리, 띠구조, 밀도 범함수 이론, 전기장
학　번: 2004-20455

감사의 말

이 학위 논문을 많은 분들의 도움이 있었기 때문에 마칠 수 있었습니다. 먼저 신석민 교수님께 화학보다 컴퓨터과학에 관심이 많았던 제가 동역학이론연구실 (Dycube Lab., ^{3}Dy)에 들어와 공부를 할 수 있도록 허락해주신 것에 감사드리며, 무엇보다 양자학의 매력을 가르쳐주신 것에도 이 학위논문을 마치며 감사의 마음을 표현하고 싶습니다. 지금 돌이켜보면 교수님의 관심사가 다양했던 것 만큼 저도 여러 분야를 접하며 이 연구 주제에 대해서도 깊은 이해를 할 수 있었습니다. 그리고 그래핀 연구를 하면서 계산 결과와 결론의 진로에 대하여 건설적이고 진심 어린 조언을 해 주신 이진용 교수님께 감사 인사 드립니다. 바쁘신 일정에도 시간을 내주시면서 이 두분과 함께 학위심사위원이 되주신 석차옥, 정연준, 김우연 교수님께도 감사 말씀 드립니다. 심사를 받으면서 이 논문의 내용이 탄탄하게 마무리 되도록 큰 도움을 주셨습니다.

연구실 구성원에게도 고마움을 표현하고 싶습니다. 단백질의 분자동역학 모의실험을 하신 장순민 박사님과, 모형분자계의 양자동역학 연구를 하신 장보영 박사님, 이 두 분들에게 어떤 질문을 드려도 제가 이해하기 쉽도록 답해주셨습니다. 그리고 처음으로 박사가 되는 것을 몸소 보여주신 이진혁 형, 공부하고 연구한 것에 대해 항상 자부심을 갖으라고 얘기해준 윤여훈 형, 처음 연구실에 들어와 컴퓨터 클러스터를 맡았을 때 직접 하나하나 가르쳐주고 마지막까지 이렇게 졸업을 할 수 있게 도와준 신창균 형, 처음 연구실에 들어왔을 때 앉을 책상을 양보해 주신 김남신 형, 꼼꼼하게 책을 읽고 공부하는 방법을 알려준 윤제성 형, 여러 책들을 소개해준 손원준 형, 양자는 어려운게 아니라고 용기를 준 조은석 형, 빨리빨리 서둘러 준비하는게 좋다며 현실적 충고를 충동적으로 해준던 남승윤 형, DFT를 처음 접하게 해준 이동형 형, “양자는 재미있는 거야.”라고 세뇌시켜준 최현호, 관심 분야가 달라도 제 얘기를 즐겁게 들어주신 박성병 형, 오래 연구실에 같이 있으면서 공부할

때 진지한 토론과 대화 상대가 되어준 김태래, 이 분들의 도움과 조언의 힘이 컸습니다. 그리고 심사 발표의 연습 대상이 되어준 후배들, “어떻게든 잘 되겠죠.”라며 긍정의 힘을 빌려준 우민우, “그게 그랬던건가요?”라며 되물어서 다시 답하게 만들어 소소히 개념들을 다시 정리하게 만들어준 손문기, “간단히 말하면 이런거죠?”라며 간결하게 해석하고 전달할 수 있게 도와준 이민준에게 고마움을 전합니다. 또, 신국조 교수님 방의 박수형 형, 정철 형, 이상익 형, 박기현 형들과 연구실을 같이 쓰면서 자주 만나고 얘기하며 여러 모습들에서 배울게 많았습니다.

마지막으로 가족들에게 감사의 말을 전하고 싶습니다. 가족의 응원이 있어서 학위 과정을 마칠 수 있었습니다. 아버지와 어머니의 끊임없는 응원에 감사드리고 Belle Park의 격려에 고마웠습니다. 그리고 저를 믿고 용기를 북돋으며 내용을 이해못해도 본문에서 오자를 찾아주는라 고생한 제 아내 김현진의 공헌이 있었습니다.